GL-TR-89-0334

Impact of a Unified DMSP Meteorological Sensor Retrieval Methodology on Global Numerical Weather Prediction

R. G. Isaacs
C. Grassotti
R. N. Hoffman
T. Nehrkorn
J.-F. Louis
M. Mickelson

Atmospheric and Environmental Research, Inc.
840 Memorial Drive
Cambridge, MA 02139-3794

February 27, 1990

Final Report
November 1988 - November 1989

GEOPHYSICS LABORATORY
AIR FORCE SYSTEMS COMMAND
UNITED STATES AIR FORCE
HANSCOM AFB, MASSACHUSETTS 01731-5000

This technical report has been reviewed and is approved for publication.

Donald C. Norquist

*DONALD C. NORQUIST
Contract Manager

Donald A. Chisholm

*DONALD A. CHISHOLM
Atmospheric/Prediction Branch

FOR THE COMMANDER

Robert A. McClatchey

*ROBERT A. McCLATCHEY, Director
Atmospheric Sciences Division

This report has been reviewed by the ESD Public Affairs Office (PA) and is releasable to the National Technical Information Service (NTIS).

Qualified requestors may obtain additional copies from the Defense Technical Information Center. All others should apply to the National Technical Information Service.

If your address has changed, or if you wish to be removed from the mailing list, or if the addressee is no longer employed by your organization, please notify GL/IMA, Hanscom AFB, MA 01731. This will assist us in maintaining a current mailing list.

Do not return copies of this report unless contractual obligations or notices on a specific document require that it be returned.

REPORT DOCUMENTATION PAGE

Form Approved
OMB No 0704-0188

1. AGENCY USE ONLY (Leave blank)	2. REPORT DATE	3. REPORT TYPE AND DATES COVERED
	February 27, 1990	Final Report: Nov. 1988 - Nov. 1989

4. TITLE AND SUBTITLE
Impact of a Unified DMSP Meteorological Sensor Retrieval Methodology on Global Numerical Weather Prediction

5. FUNDING NUMBERS
PE 61101F
PR ILIR TA 9E WU AA

Contract F19628-89-C-0011

6. AUTHOR(S)
R.G. Isaacs
C. Grassotti
R.N. Hoffman
T. Nehrkorn
J.-F. Louis
M. Mickelson

7. PERFORMING ORGANIZATION NAME(S) AND ADDRESS(ES)
Atmospheric and Environmental Research, Inc.
840 Memorial Drive
Cambridge, MA 02139-3794

8. PERFORMING ORGANIZATION REPORT NUMBER

9. SPONSORING/MONITORING AGENCY NAME(S) AND ADDRESS(ES)
Geophysics Laboratory
Hanscom AFB
Massachusetts 01731-5000

Contract Manager: Donald Norquist/LYP

10. SPONSORING/MONITORING AGENCY REPORT NUMBER
GL-TR-89-0334

11. SUPPLEMENTARY NOTES

12a. DISTRIBUTION/AVAILABILITY STATEMENT
Approved for public release;
distribution unlimited.

12b. DISTRIBUTION CODE

13. ABSTRACT *(Maximum 200 words)*

An observing system simulation experiment (OSSE) is conducted using simulated DMSP microwave sensor data, surrogate data for cloud imagery (all based on a nature run), and the application of the unified retrieval (UR) method for DMSP to obtain meteorological variables as proposed by Isaacs (23). Both the DMSP SSM/T-1 temperature sounder and SSM/T-2 moisture sounder data are simulated. The unified retrieval uses physical considerations based on a forecast or other first guess by comparing the sensor data with those simulated using the first guess profiles. Although the preliminary UR did not perform better than the statistical retrieval, enhanced UR are found to be more accurate in terms of integrated water vapor amounts. The retrieved variables, primarily temperature and moisture, are used to construct initial conditions for input to the AFGL global spectral numerical weather prediction model. The resulting analyses and forecasts are verified against the nature run and compared with analyses and forecasts based on the present statistical retrieval scheme. The impact of the preliminary UR used in this experiment was small. However the enhanced UR should provide improved humidity analyses.

14. SUBJECT TERMS		15. NUMBER OF PAGES
Satellite meteorology Water vapor Clouds	Unified retrieval Numerical weather prediction	76
		16. PRICE CODE

17. SECURITY CLASSIFICATION OF REPORT	18. SECURITY CLASSIFICATION OF THIS PAGE	19. SECURITY CLASSIFICATION OF ABSTRACT	20. LIMITATION OF ABSTRACT
Unclassified	Unclassified	Unclassified	SAR

Contents

Tables

Figures

1. Background and motivation

This study investigates the application of a unified retrieval (UR) approach tailored to the Defense Meteorological Satellite Program (DMSP) meteorological sensor suite to provide input data fields to a global spectral numerical weather prediction (NWP) model and to investigate the impact of these data on global NWP. In the unified retrieval approach, all of the available DMSP data is utilized in a multispectral sense. The existing operational statistical retrieval capability is exploited to provide parameter first guesses. First guess derived brightness temperatures are then compared with the original data and adjustments, based on sensor channel residuals, are made to the first guesses as required. A physically based simultaneous retrieval provides the appropriate parameter adjustments. Results of retrieval simulation calculations illustrate the improvements possible to the statistical first guesses by utilizing all sensor data multispectrally and to the first guess parameters by employing the physical adjustment step [22]. Recognizing the potential effect of clouds on the millimeter wave data, a method has been outlined to introduce required first guess cloud information by image processing visible/infrared imager data. This procedure provides the opportunity to characterize the uniformity (both atmospheric and surface) of the relatively large microwave FOV. This provides potential insights into both cloud and surface type classification with implications for determining their emissivities. The unified retrieval approach has been described by Isaacs [23].

The sensor payload of the Defense Meteorological Satellite Program (DMSP) spacecraft of the 1990's will consist of a visible/infrared imager (the operational linescan system or OLS), a microwave temperature sounder (SSM/T-1), a millimeter wave water vapor sounder (SSM/T-2), and a microwave imager (SSM/I). The current OLS imager provides high spatial resolution, global cloud imagery. Notably, all the other sensors are millimeter/microwave instruments. Of the microwave mission sensors, the SSM/T-1 and SSM/I are currently operational [14]. The SSM/T-1 is an microwave instrument from which temperature profiles may be retrieved. Clouds have only a small effect on the SSM/T temperature retrieval accuracy. The SSM/T-2 millimeter moisture sounder is a planned enhancement to the T-1. Like the proposed AMSU-B, the SSM/T-2 includes several channels near the 183.31 GHz water vapor absorption line. (For a detailed description of these instruments see [4].) The millimeter wave channels used are sensitive to the presence of cloud [24]. The SSM/T-2 is scheduled for launch in the early 1990s. The attributes of these sensors are summarized in Table 1. Meteorological data requirements tasked to this sensor complement include the acquisition of cloud information, temperature and water vapor profiles, precipitation, and surface properties. One important application of these data products is global numerical weather prediction [25].

Current operational analysis procedures for the OLS, SSM/T-1, and SSM/I treat each sensor data stream independent of the others. OLS imagery is processed into global cloud property fields using an automated nephanalysis algorithm [30]. The retrieval scheme for temperature sounding by the SSM/T-1 is based on regression of SSM/T-1 brightness temperature data against desired mandatory level temperatures [39] and an analogous statistical approach will be used in the determination of meteorological parameters such as cloud liquid water content and precipitation (among others) from the SSM/I data [31]. These approaches share a common

Instrument	Frequency or Wavelength	Polarization (H or V)	FOV (km)	Response	NEΔT (K)
SSM/T	50.500 GHz	H	200	surface	0.6
	53.200	H	200	T at 2 km	0.4
	54.350	H	200	T at 6 km	0.4
	54.900	H	200	T at 10 km	0.4
	58.825	V	200	T at 16 km	0.4
	59.400	V	200	T at 22 km	0.4
	58.400	V	200	T at 30 km	0.5
SSM/T-2	90.00	V	100	surface, water vapor	0.6
	150.00	V	60	surface, water vapor	0.6
	183.31±1	V	50	water vapor	0.8
	183.31±3	V	50	water vapor	0.6
	183.31±7	V	50	water vapor	0.6
SSM/I	19.350	H and V	50	surface	0.6
	22.235	V	50	water vapor	0.6
	37.000	H and V	25	clouds, rain	0.8
	85.000	H and V	12.5	clouds, snow	1.1
OLS	0.4-1.1 μm		0.6	surface/clouds	-
	10.5-12.5 μm		2.4	surface/clouds	-

Table 1. DMSP Meteorological Sensors

heritage in the "D" matrix technique described by Gaut et al. [15]. Data from the SSM/T-1 and SSM/T-2 will be integrated together in a statistical retrieval of water vapor profiles (cf. [23]).

For a variety of reasons, the operational approach described above could be improved. The main criticisms are:

1. The lack of a multispectral perspective;
2. The reliance on statistical retrieval approaches, which produce retrieval fields with reduced variance properties, fail to treat inherent problem nonlinearities, and provide little opportunity to monitor retrieval quality; and
3. The neglect of some physical aspects of the retrieval problem, such as the effect of cloud on millimeter wave brightness temperatures.

To address these issues, an alternative retrieval scheme has been developed [22]. The implementation and experiments described here are preliminary. However, our approach does attempt

to address the difficulties cited above and, in particular, it has the potential to integrate available data sources in a unified, multispectral retrieval constrained by radiative transfer principles.

We have evaluated the impact of the unified retrieval scheme by executing an observing system simulation experiment (OSSE). This OSSE, denoted URSAT, is formulated to facilitate direct comparison with a previously conducted OSSE which employs an analog to the simple statistical retrieval approach currently planned for operational implementation [26]. This latter OSSE, denoted SSMSAT was performed under contract F19628-86-C-0141 and described in detail by Grassotti et al. [17]. The forecast analysis system for the OSSE is the AFGL Global Spectral Model (GSM) [6] and the AFGL Statistical Analysis Program (ASAP) [36]. The reference atmosphere or nature run is that described by [11] obtained from the 1.875° ECMWF grid point global forecast model.

The experimental procedure consists of the following steps:

1. DMSP sensor data were simulated from the reference atmosphere using the RADTRAN radiative transfer model for the microwave sensors [13]; OLS imagery was simulated by analyzing the reference atmosphere moisture field for large scale cloud and employing this cloud coverage/height distribution data directly as a surrogate for cloud analyzed DMSP OLS imagery.
2. First guess statistics were derived for the microwave sensors using procedures analogous to those for the SSMSAT OSSE [26]. These statistics were used to derive statistical retrievals to initiate the unified retrieval procedure. Unified retrieval error statistics were obtained from an off line retrieval error analysis based on independent retrieval simulations.
3. The relevant retrieved parameters were used as input for a one week long data assimilation experiment.
4. Three ninety-six hour forecasts were run from the analyses produced above. Analyses and forecasts were verified against the reference atmosphere and compared to those obtained from SSMSAT.

This report consists of four sections. Following this introduction, Section 2 introduces the unified retrieval approach, provides some simulated results for the DMSP sensors, and addresses incorporation of the retrieved parameters within the GSM. Section 3 describes our OSSE results and Section 4 contains a summary and concluding remarks. An appendix describes a parameterization of cloud properties in terms of the available nature run variables. The complete parameterization was developed for the OSSE but only a simplified version of it was actually used as described in Section 2.

2. Unified retrievals

2.1 Methodology

The retrieval approach for the DMSP illustrated in Figure 2.1 employs physical considerations and allows for the incorporation of all data sources. Recognizing potential operational constraints, an attempt has been made to build on the attributes of the existing DMSP retrieval capability and experience. The microwave sensor data, $T_b{}^0$, is employed with the "D" matrix statistical retrieval to provide first guesses for the desired parameters, P^0: temperature, $T(p)$, and water vapor profiles, $q(p)$, surface emissivity, ϵ_s, and temperature, T_s. Simulated brightness temperatures, $T_b{}^n$, are then evaluated to examine the consistency of the first guesses with the observations. The forward problem calculation (denoted by F in Figure 2.1) is accomplished using the RADTRAN simulation code [13] as modified by [27]. When the residuals, Δ^n, (i.e. differences between simulated and observed brightness temperatures) are small, the process terminates. However, when residuals are larger than a preset tolerance (usually determined by the sensor noise equivalent brightness temperatures (NEΔT) and scene noise), the procedure goes on to adjust the first guess profiles. This adjustment is accomplished by using the residuals in a simultaneous physical retrieval based on both the work of Susskind et al. [43] and Smith et al. [42]. Monitoring residuals also provides the means to quality control each retrieval.

2.1.1 Physical retrievals

The radiative transfer equation for microwave frequencies is:

$$T_{b\nu} = \left[\epsilon_s T_s + (1 - \epsilon_s)\int_0^{p_s} T(p)\, d\tau_\nu'\right]\tau_\nu(p_s) + \int_{p_s}^{0} T(p)\, d\tau_\nu \tag{2.1}$$

where

$$\tau_\nu(p) = \exp\left[\int_0^{p} k(\nu, p')\, dp'/\mu\right] \tag{2.2}$$

and

$$\tau_\nu'(p) = \exp\left[\int_p^{p_s} k(\nu, p')\, dp'/\mu\right] \tag{2.3}$$

Here, μ is the cosine of the path zenith angle, τ_ν and τ_ν' are the upward and downward transmission functions, respectively, and p_s is the surface pressure. Specular surface reflection is assumed.

Differentiating equation (2.1) with respect to the desired variables U, T, T_s and ϵ_s where U is the integrated water vapor content, and dropping the frequency indices, one obtains:

$$\Delta^n = \frac{\partial T_b}{\partial \epsilon_s}\delta\epsilon_s + \frac{\partial T_b}{\partial T_s}\delta T_s + \frac{\partial T_b}{\partial T}\delta T + \frac{\partial T_b}{\partial U}\delta U \tag{2.4}$$

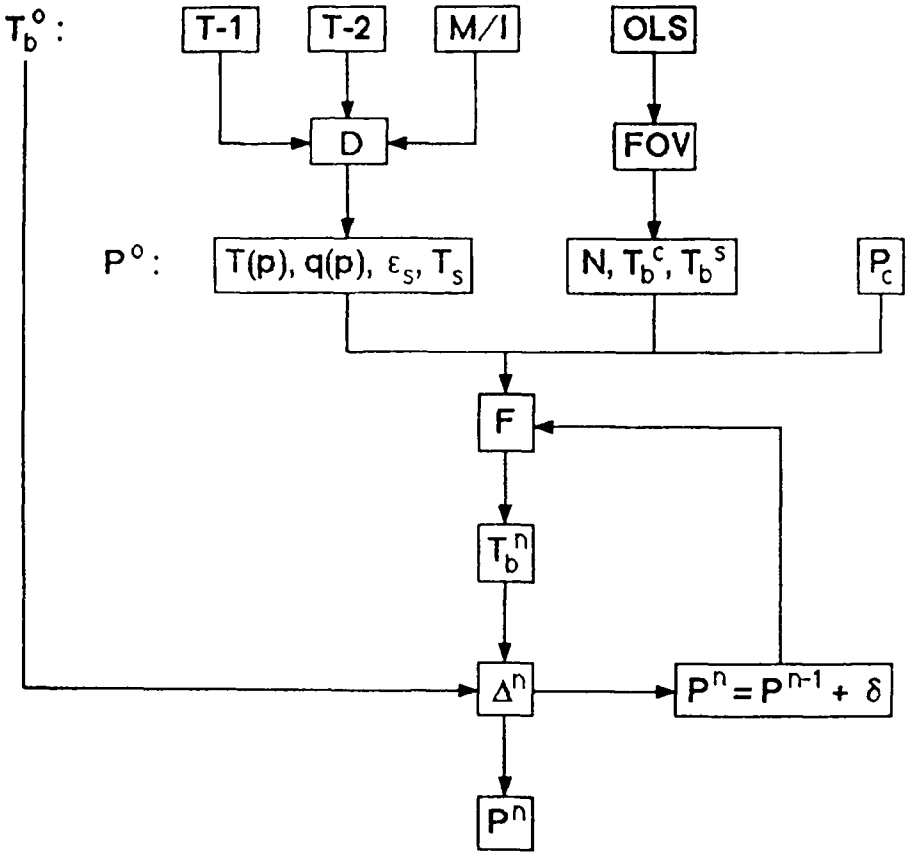

Figure 2.1. Schematic of unified DMSP retrieval scheme

where $\tau_s=\tau(p_s)$ and:

$$\frac{\partial T_b}{\partial \epsilon_s} = \left[T_s - \int_0^{p_s} T(p)\, d\tau'\right] \tau_s \tag{2.5}$$

$$\frac{\partial T_b}{\partial T_s} = \epsilon_s \tau_s \tag{2.6}$$

$$\delta T \frac{\partial T_b}{\partial T} = \tau_s (1 - \epsilon_s) \left[\int_0^{p_s} \delta T\, d\tau'\right] + \int_{p_s}^{0} \delta T\, d\tau \tag{2.7}$$

$$\begin{aligned} \delta U \frac{\partial T_b}{\partial U} &= (\epsilon_s - 1) \left[T_s - \int_0^{p_s} T(p)\, d\tau' + \tau_s T(0)\right] \frac{\partial \tau_s}{\partial U} \delta U \\ &+ \int_0^{p_s} \left[\frac{\partial \tau}{\partial U} + \tau_s (\epsilon_s - 1) \frac{\partial \tau'}{\partial U}\right] \delta U\, dT \end{aligned} \tag{2.8}$$

Parts of $\delta U \left(\frac{\partial T_b}{\partial U}\right)$ have been obtained using integration by parts. Note that $\left(\frac{\partial \tau_i}{\partial T}\right)$ and the variation with respect to surface pressure have been ignored.

The quantities δU and δT may be expanded in series of the eigenvectors of the covariance matrices (EOFs) of U and T, with N_u and N_t terms, respectively.

$$\delta U(p) = \sum_{j=1}^{N_u} A_j \phi_j(p) \tag{2.9}$$

$$\delta T(p) = \sum_{j=N_u+1}^{N_u+N_t} A_j \phi_j(p) \tag{2.10}$$

$$\delta T_s = A_{N_u+N_t+1} \tag{2.11}$$

$$\delta \epsilon_s = A_{N_u+N_t+2} \tag{2.12}$$

Upon substitution of (2.9 - 2.12) into (2.4) a linear equation in the coefficients A_j is obtained:

$$\Delta^n = \sum_{j=1}^{N_u+N_t+2} A_j \Phi_j \tag{2.13}$$

where the Φ_j's are functions of the terms in equations (2.5-2.8). The desired difference terms, δ, in the relaxation equation:

$$p^n = p^{n-1} + \delta \tag{2.14}$$

are available by solving (2.13) for the A_j's.

The ridge stabilized, least squares solution is given by:

$$A = \left(\Phi^T \Phi + \sigma H\right)^{-1} \Phi^T \Delta^n \tag{2.15}$$

where σ is the ridge parameter and the diagonal elements of the **H** matrix are the inverse of the fractional variance due to each EOF.

Alternatively, the geophysical profiles may be retrieved directly (i.e. without the use of EOF basis functions). In these cases N_u and N_t are the number of retrieval layers/levels for water vapor and temperature, respectively, Φ is simply the matrix containing derivatives of channel T_b with respect to retrievable parameters obtained from equations 2.5–2.8, and H is equal to the identity matrix.

2.1.2 Cloud Effects

Cloud or precipitation in the field-of-view (FOV) of the microwave sensors can be problematic. In cloudy areas, cloud coverage and cloud top height first guesses are necessary for the physical retrieval step (Equation 2.1 is modified). The UR forward problem requires the profile of cloud liquid water content (LWC). Layer cloud liquid water content determines cloud millimeter wave attenuation through a simple relationship. Cloud attenuation, $\alpha(\nu,T,z)$, is given by the Rayleigh approximation [44]:

$$\alpha(\nu, T, z) \quad 6\pi\nu \, \mathrm{Im}\left[\frac{m^2 - 1}{m^2 + 2}\right] \mathrm{LWC} \tag{2.16}$$

where ν is the frequency in wave numbers and m is the complex index of refraction of water evaluated using Ray's empirical expression [37]. Falcone et al. [12] have shown that the use of Rayleigh approximation instead of the full Mie theory for these cloud models is justified for frequencies less than about 300 GHz. If unaccounted for, brightness temperature contributions due to cloud resulting in residuals in the forward problem/data comparison procedures will be interpreted as necessary adjustments in the temperature/ moisture amounts sensed by the SSM/T-2 sounder.

Precipitation will generally preclude soundings of temperature and moisture and the determination of surface properties. Quality control flags for precipitation (as well as precipitation amounts) can be obtained from the SSM/I statistical retrieval [31, 28] . Isaacs and Deblonde [24] have discussed the potential impact of cloud on statistical millimeter wave water vapor retrievals and evaluated the sensitivity of these channels to cloud presence.

Collocated with the microwave sensors aboard the DMSP spacecraft, the Operational Linescan System (OLS) provides both visible and infrared imagery at high spatial resolution. With this much higher spatial resolution, the visible and infrared data from the OLS imagery can be used to characterize the uniformity and cloudiness of the much larger microwave footprints. In those areas where the contributions from the atmosphere to microwave brightness temperature are small (i.e., nonprecipitating situations), visible or infrared data is able to provide guidelines on the uniformity of the surface observed within a field of view. When clouds obscure portions of the microwave field of view, the imager data provides the complementary capability of cloud property determination.

Cloud fields from the DMSP OLS (using an appropriately spatially averaged subset of visible and infrared imagery) aid in cloud/no cloud discrimination. To determine first guess cloud properties within the FOV necessary to accomplish the physical retrieval step, image processing of the high spatial resolution OLS imager data within the relatively larger microwave footprint provides first guess cloud coverage, N, and equivalent brightness temperatures (EBTs) for cloud top and surface, T_b^c, T_b^s.

Classically, techniques to infer FOV non-uniformity have been referred to as texture analysis methods. A number of approaches can be used for texture analysis including:

1. Examination of the spatial power spectrum of an image through Fourier decomposition,
2. Edge enhancement, and
3. Spatial coherence.

We have chosen the spatial coherence approach [8] for the determination of both cloud and surface properties from OLS data. Cloud top brightness temperature along with the first guess temperature profile yields a first guess cloud top pressure, p_c. Over the oceans, cloud properties derived from the OLS imager data are supplemented by information on cloud integrated liquid water content (ILWC) available from the SSM/I. Cloud ILWC provides a parameterization of cloud optical thickness and emissivity. These cloud properties are required to treat the effect of cloud on the SSM/T-2 sensor data and therefore are input to the forward problem.

2.2 Simulation of DMSP data

2.2.1 Microwave data

In order to simulate SSM/T data realistically, we conducted a careful simulation study of the SSM/T instruments and data processing algorithm. The simulation study used subsets of the nature run fields, a realistic forward model to calculate brightness temperatures, a statistical retrieval algorithm similar to the operational algorithm, and finally, the physical retrieval step which updates the first guess profile using the methodology outlined above. The physical update step is similar to that used in previous cloud free retrieval simulations except for the retrievable quantities used by the algorithm. Unlike the previous efforts in which EOF coefficients of the physical variables (u, T) were retrieved, the integrated water vapor and temperature are retrieved directly on the desired vertical levels. Integrated water vapor is retrieved in 4 vertical layers (from the top of the atmosphere to 300, 700, 850 and 1000 mb), while temperature is retrieved on 11 pressure levels (50, 70, 100, 150, 200, 300, 400, 500, 700, 850, 1000 mb). Finally, to facilitate direct comparison with statistical first guess profiles and ECMWF nature run profiles, temperature retrievals were interpolated to the 12 mandatory pressure levels and the water vapor profiles were converted to relative humidity at the lowest 6 mandatory levels. Retrieval RMSE values were calculated for each of the geophysical categories noted below. The results of these off-line calculations allowed us to characterize the error structure of the unified retrievals. These error statistics were then used to generate unified retrievals for the OSSEs in a series of in-line retrieval simulations which are also described below.

The most accurate way to simulate an observing system such as the SSM is to use the nature run to generate the radiances (or brightness temperatures) that would be observed, add appropriate measurement errors and simulate the retrieval of temperature and moisture profiles. It would be very expensive to do this for every data point due mainly to the computational demands of the forward problem calculation. Instead, we characterized the errors of the SSM instruments and the associated operational retrieval system. To do this, we solved the forward problem, i.e. the brightness temperature computation, only for two relatively small subsets of the data. The first subset was used to derive regression equations between nature run temperature and moisture profiles and computed brightness temperatures. The coefficients of these equations form the so-called D matrix. Several D matrices were derived, depending on whether the ocean was ice covered or not, and, in the case of humidity retrievals, whether the sky was clear or cloudy. A similar approach is expected to be used operationally to obtain the T-2 retrievals. These D matrices were then used to simulate statistical retrievals for the second subset of data

and to provide the background field (i.e. first guess) for the unified retrieval. The second subset of radiances and their statistical retrievals were then used to generate unified retrievals, which were compared with the nature run values to compute error statistics. This procedure enabled us to derive a set of unified retrieval error statistics.

These error statistics were stratified according to geophysical criteria, which included the latitude and strength of the wind in addition to cloudiness and the presence of ice. The SSM/T-2 is designed to retrieve moisture profiles using five microwave channels near the 183.31 Ghz water vapor resonance line. For a thorough review of millimeter wave moisture retrievals see [23]. The main advantage of millimeter wavelengths over infrared retrievals is the low emissivity of the ocean surface, making possible the retrieval of low layer moisture. However, when wind speeds are high, surface emission dominates the atmospheric emission and the T-2 should provide less accurate retrieval of atmospheric boundary layer humidity. Another advantage of the T-2 is that clouds are not opaque to millimeter waves. However, the effect of clouds on the transmission in the millimeter region is not negligible. In particular, the role of ice clouds as attenuators may have been underestimated. For measurements taken over the oceans the main difficulty is estimating the effect of high winds on the surface emissivity. Over land, the variable, and in general higher surface emissivity makes millimeter wave retrieval of moisture less attractive. We simulated UR over oceans only because of the expected poorer retrieval performance over land.

In the OSSE, then, we used the error statistics to modify the nature run profiles and create pseudo-retrievals. This approach, except for the additional refinement of the statistical retrievals by the unified retrieval is very much the same as that performed for the SSMSAT experiment which is described in detail by Grassotti et al. [17].

2.2.2 Cloud data

For simulation purposes, presence of cloud in the microwave field of view (FOV) is an important consideration. Cloud will affect the accuracy of millimeter wave moisture sounding from the SSM/T-2 [24]; indeed the operational SSM/T-2 algorithm will stratify moisture retrievals by expected cloud liquid water content to partially account for this effect. In the unified retrieval (UR) implementation, both the OLS imager visible and infrared channels and the SSM/I microwave imager can be expected to provide information on cloud.

Neither the OLS nor the SSM/I will provide cloud LWC profiles, however. We have assumed that the coverage fraction N and cloud top pressure, p^c, of the upper most cloud layer are retrievable from the OLS. The SSM/I can be assumed to retrieve integrated (but not profile) cloud LWC (kg/m^2) over the ocean only. Over land areas, the accuracy of these observations are too unreliable to use.

Cloud data are needed to simulate the sensor data, in the study of the retrieval errors and as a categorical quantity for determining error statistics when generating data for the OSSE. The forward problem requires profiles of liquid water content. Actual nature profiles are therefore needed to simulate the radiances. The forward problem is also employed by the unified retrieval methodology. In this case we assume we know only observable cloud parameters and make reasonable assumptions, which would have to be made operationally, about the liquid water profile. The OSSE data depend only on whether or not cloud is present. Since that nature

run archived only the standard variables - wind components, temperature, relative humidity and surface pressure - we developed a procedure to deduce cloud parameters from the standard variables. Our approach is to first diagnose layer cloud amounts for different cloud types. These are then used to determine the various cloud parameters we require.

A straightforward application of the Tibaldi scheme to the nature run RH data lead to a gross overestimate of cloudiness. To remedy this problem, we have tuned the Geleyn scheme for estimating large-scale layer cloud cover (CC).

$$CC \quad \begin{cases} \left[\frac{RH - RH_c}{1 - RH_c}\right]^2 & RH > RH_c \\ 0 & RH < RH_c \end{cases} \tag{2.17}$$

The RH_c for mandatory layers from 1000 to 300 mb are tuned assuming random overlap to give agreement with observed climatological zonal mean total cloud cover, after convective clouds have been removed. Because small-scale convective clouds can significantly impact brightness temperatures observed by the T-2 sensor, we also developed a scheme to diagnose convective cloudiness from the nature data and investigated the use of the divergence fields, based on the ideas presented in Julian [29], and the conditional stability of the atmosphere. This scheme results in estimates of convective cloud cover and top, stratiform cloud cover at the mandatory levels, and total cloud cover. The convective cloud cover is estimated from the divergence profile while cloud top is determined as the level of maximum divergence between 500 mb and 150 mb. Stratiform cloud cover of the portion of the grid box not covered by convection is obtained from (2.17), using values of RH_c = 95.2%, 56.9%, 99%, 99%, 64.3%, 98.5% at σ = 1.00, .85, .70, .50, .40, .30., where σ is the ratio of model level to surface pressure. Total cloud cover is obtained by the appropriate combination of the convective clouds, which are assumed to be stacked vertically, and the stratiform clouds, for which random overlap is assumed. Agreement with observed, climatological values of zonal mean total cloud cover to within an rms error of 10.3% was achieved.

The complete cloud cover diagnosis scheme requires knowledge of the convergence, or equivalently, the vertical velocity profile at each SSM/T observing location. For the current study, we did not have enough resources to resample the nature run. Instead we used profiles sampled previously for the SSMSAT experiment, which did not include the vertical velocities. Therefore, during the in-line retrieval simulations, we used only the RH based Geleyn diagnosis of large-scale cloudiness described above. Note that in experiment SSMSAT, the inverse Tibaldi scheme, as described by Norquist [36], was used. However we do anticipate that the complete scheme will prove useful in future research. A more complete discussion of the RH to cloud analysis algorithms is presented in Appendix A.

An effective cloud top pressure is obtained by suitably weighting the appropriate cloud top level pressures for each cloud type. In the retrieval simulation, appropriate errors must be added to these quantities to account for the cloud parameter retrieval process (i.e. nephanalysis). Errors of 10% in coverage and 1 km in $Z(p^c)$ were deemed appropriate. The above procedure assumes that the upper most cloud layer has unit emissivity. In the case of upper level cirrus cloud, both cloud coverage and top pressure will be effective amounts, to account for the non-unit emissivity of these clouds. When nature run layer temperature/ humidity implies the presence

of cirrus, estimates of coverage and cloud top pressure must be modified accordingly. Since the nature run RH extends only to 300 mb, some cirrus may be missed, however, the impact on cloud LWC should be small.

Profiles of cloud liquid water content and SSM/I integrated cloud LWC were simulated from the nature run, by assuming an appropriate cloud type model for each model layer diagnosed to contain cloud with coverage fraction *N(i)*. Since layer cloud mass density, *m(i)* (g/m^3) is type dependent (see Table 2), type assignment will provide a layer dependent $(p_i \rightarrow p_{i+1})$ cloud LWC*(i)* in kg/m^2:

$$\mathrm{LWC} = N(i)\, m(i)\, \Delta z\,(p_i, p_{i+1}) \tag{2.18}$$

Table 2 includes mass densities for five typical low and middle clouds. Summing over all cloudy nature run model layers gives the required simulated SSM/I retrieved integrated LWC (ILWC):

$$\mathrm{ILWC} = \sum_i N(i)\, m(i)\, \Delta z\,(p_i, p_{i+1}) \tag{2.19}$$

A retrieved error was added to this quantity. Based on results of the SSM/I calibration/validation study we found the appropriate error for this quantity to be about 0.05 kg/m^2. Cloud type assignment was based on the diagnosed cloud height (from the OLS) from which it was assumed that a particular type was uniquely implied. The inferred cloud type, in turn, implied a cloud thickness and, hence, cloud bottom. Cloud layer LWC was then assumed to be distributed evenly among the cloud model vertical layers between the diagnosed cloud top and bottom.

Model	Type	Mode Radius (μm)	Mass Density (g/m^3)	Vertical Extent (km)
1	Stratus	2.70	0.15	0.5-2.0
2	Cumulus	6.00	1.00	1.0-3.5
3	Altostratus	4.50	0.40	2.5-3.0
4	Stratocumulus	6.25	0.55	0.5-1.0
5	Nimbostratus	3.00	0.61	0.5-2.5

Table 2. Typical Cloud Type Characteristics

2.3 Retrieval statistics

Unified retrieval simulations were conducted using subsets of nature run output as described above. Retrieval bias and error standard deviation were compiled and used as input to the in-line retrieval simulations in which retrievals were created at the location of each satellite field of view. Here we describe these retrieval results since they directly affect the impacts we obtain in the assimilation/forecast system.

After the retrieval data had been simulated and the assimilation cycles run a computer coding error was discovered in the unified retrieval software. Since the error related to the calculation of derivatives of brightness temperature with respect to the retrievable parameters, it significantly degraded the quality of the retrievals in some cases. Moreover, the off-line retrievals also contained problems stemming from interpolation of the profile from retrieval levels to model levels. This was particularly true for temperature near 100 mb. Once these problems were uncovered the retrieval software was corrected and appropriately modified. The number of retrieval levels was also increased to correspond more directly with the model pressure levels; the result was a strong positive impact on the retrieval quality at certain levels. Unfortunately, due to time and manpower constraints, it was not feasible to rerun the entire assimilation experiment. Hence, we mainly present the updated retrieval results in this section, while the data impacts discussed in the next section are based on the poorer quality preliminary retrievals which were first obtained.

Figures 2.2, 2.3 and 2.4 present the retrieval errors of the updated unified retrieval system for temperature, integrated water vapor, and relative humidity, respectively. In each plot, which reflects an ensemble of between 200 and 600 individual retrievals, the solid curve is the climate standard deviation, the dashed curve is the statistical first guess error, and the dotted curve is that of the physical UR update. Each panel shows results for a different geophysical category.

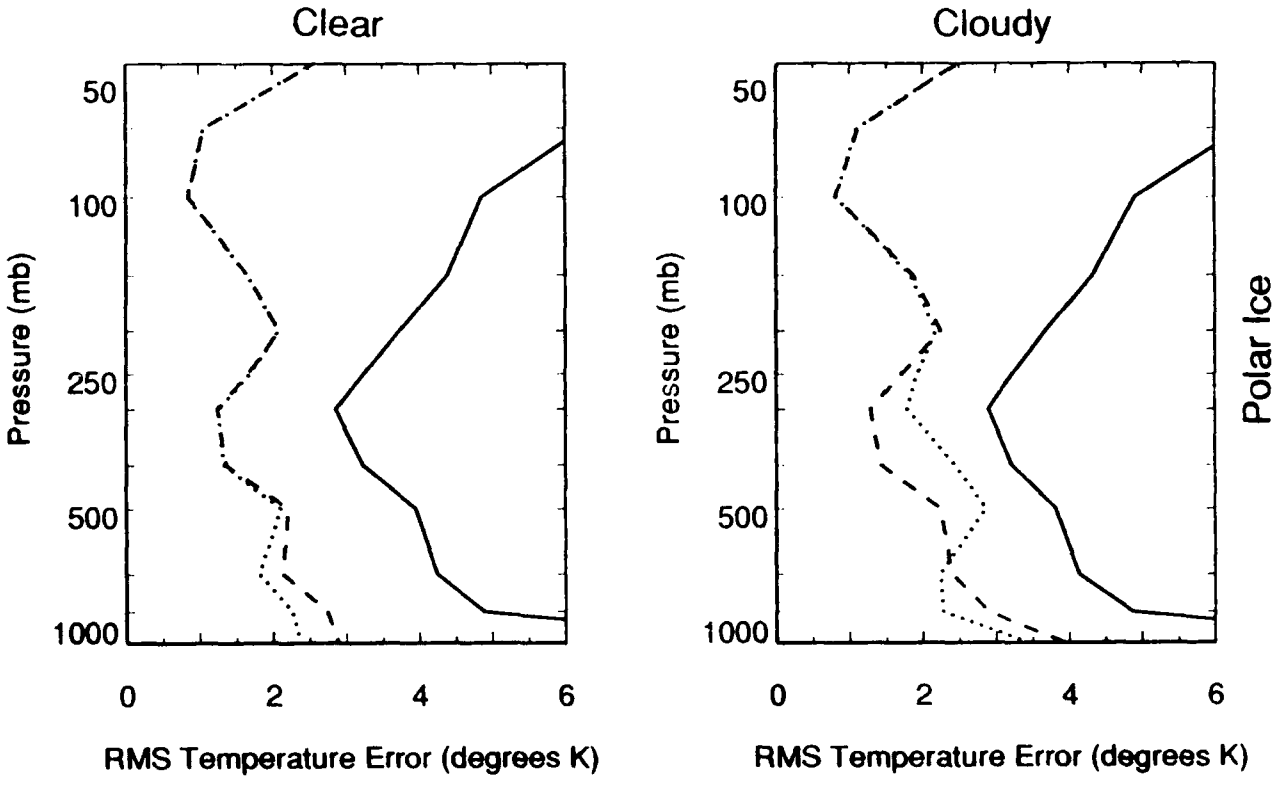

Figure 2.2. RMS temperature retrieval errors for various geophysical categories. Shown are climatology (solid), statistical first guess (dashed), and unified retrieval (dotted). (Continued . . .)

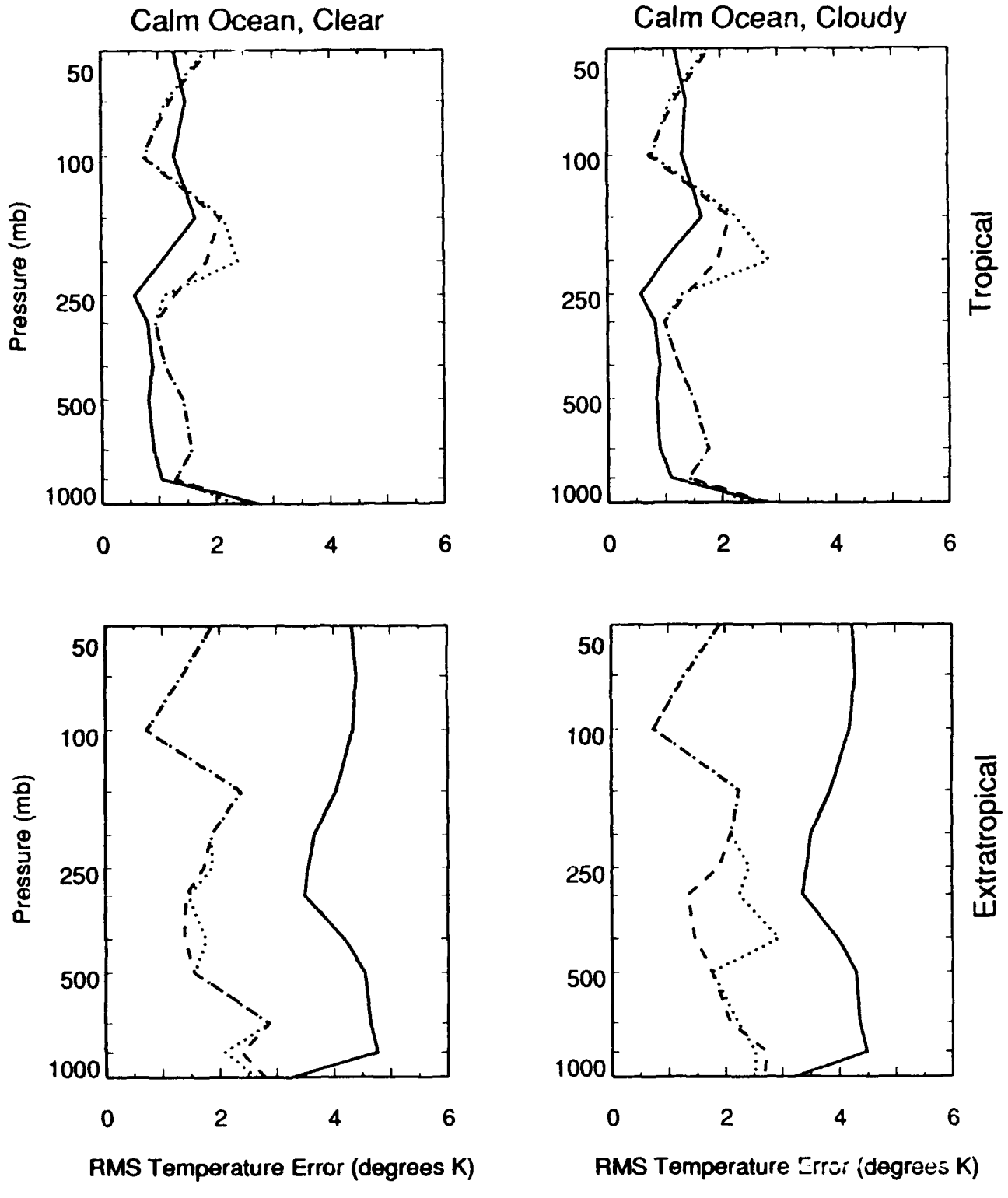

Figure 2.2. RMS temperature retrieval errors for various geophysical categories. Shown are climatology (solid), statistical first guess (dashed), and unified retrieval (dotted). (Continued . . .)

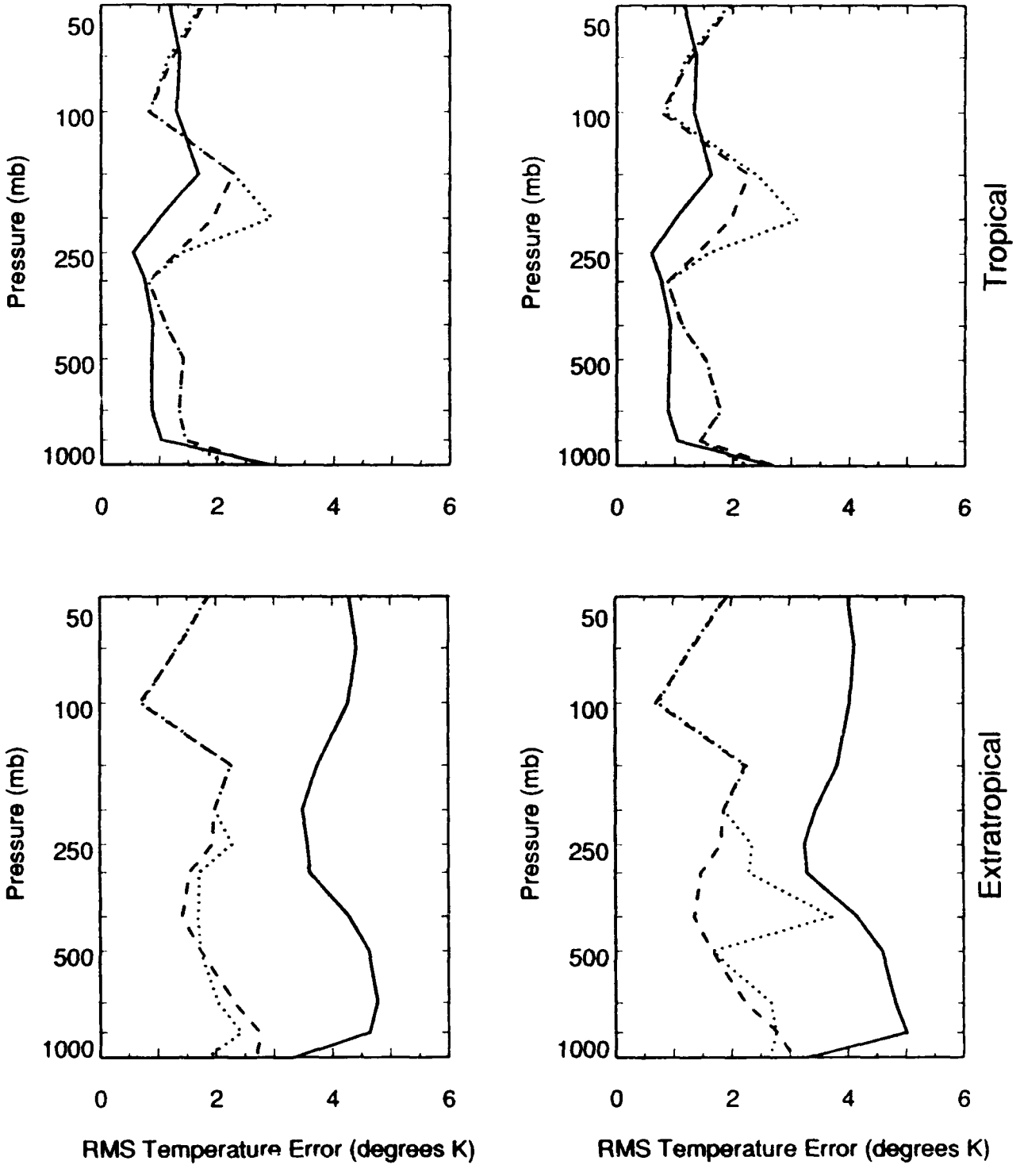

Figure 2.2. RMS temperature retrieval errors for various geophysical categories. Shown are climatology (solid), statistical first guess (dashed), and unified retrieval (dotted).

The unified retrievals consistently improve the retrieval of low level temperature. This is most evident for retrievals over polar ice and in extratropical clear conditions (Figure 2.2.). At higher levels temperature retrievals seem to degrade relative to the first guess by as much as 1 degree rms. This degradation seems to amplify in the presence of clouds with the maximum occurring at 400 to 500 mb in the extratropics and 200 to 300 mb in the tropics.

It is also interesting to note that in the tropics the statistical retrieval actually performs worse than climatology. The retrieval regression coefficients (i.e. the D Matrix) were derived from a mix of tropical and extratropical atmospheres. Because the D matrix coefficients are optimal in an rms sense, they tend to fit the extratropics better where there is more variance (roughly 3 K rms) to explain than in the tropics where the temperature variance is only $\sim$ 1 K. Separate D matrices for tropical and extratropical air masses should eliminate this problem.

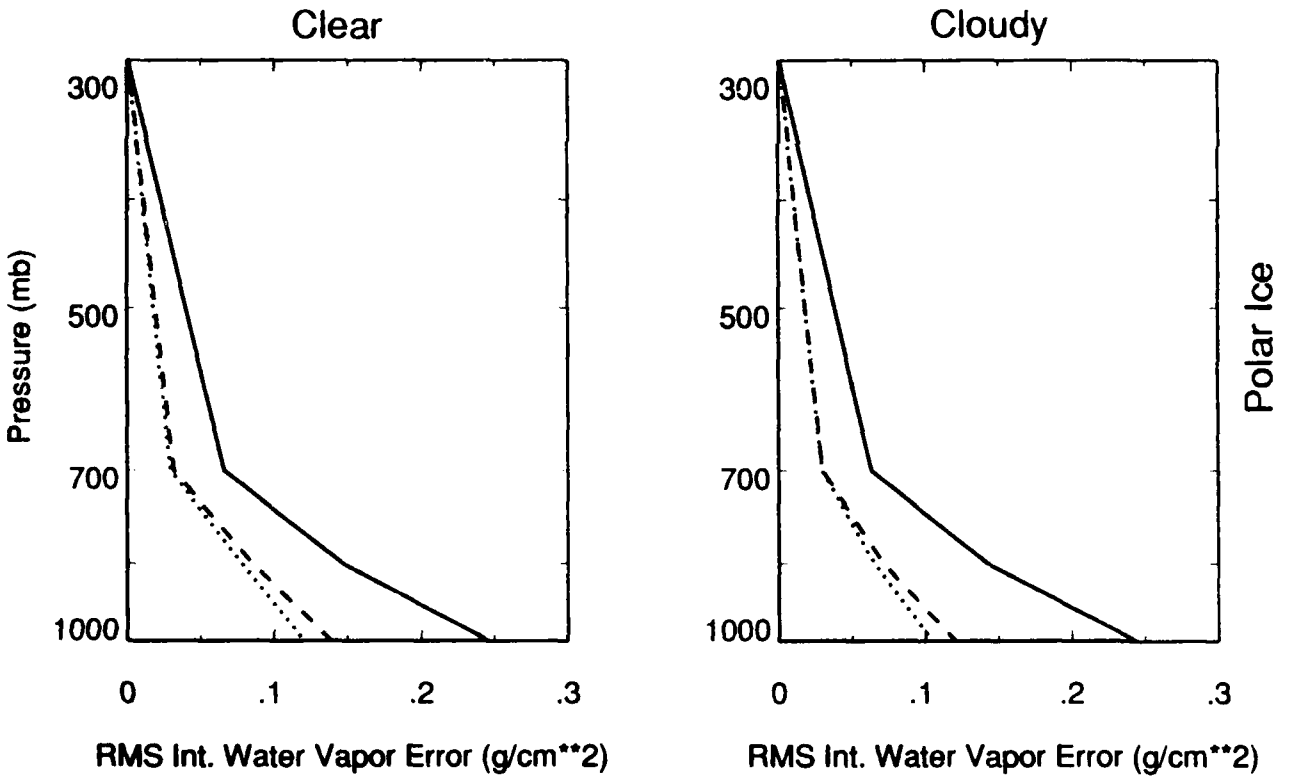

Figure 2.3. RMS integrated water vapor retrieval errors for various geophysical categories. Shown are climatology (solid), statistical first guess (dash), and unified retrieval (dot). (Continued . . .)

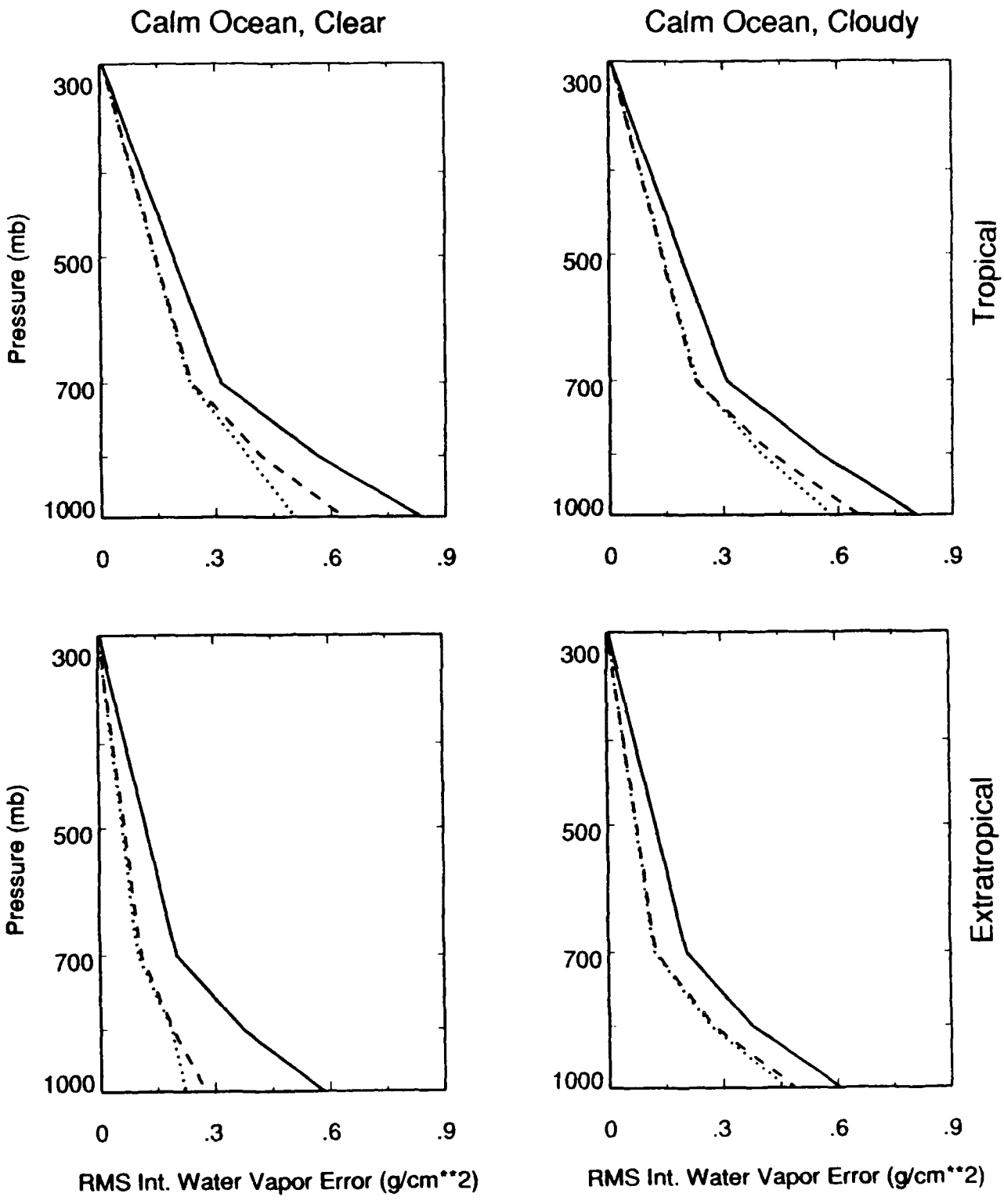

Figure 2.3. RMS integrated water vapor retrieval errors for various geophysical categories. Shown are climatology (solid), statistical first guess (dash), and unified retrieval (dot). (Continued . . .)

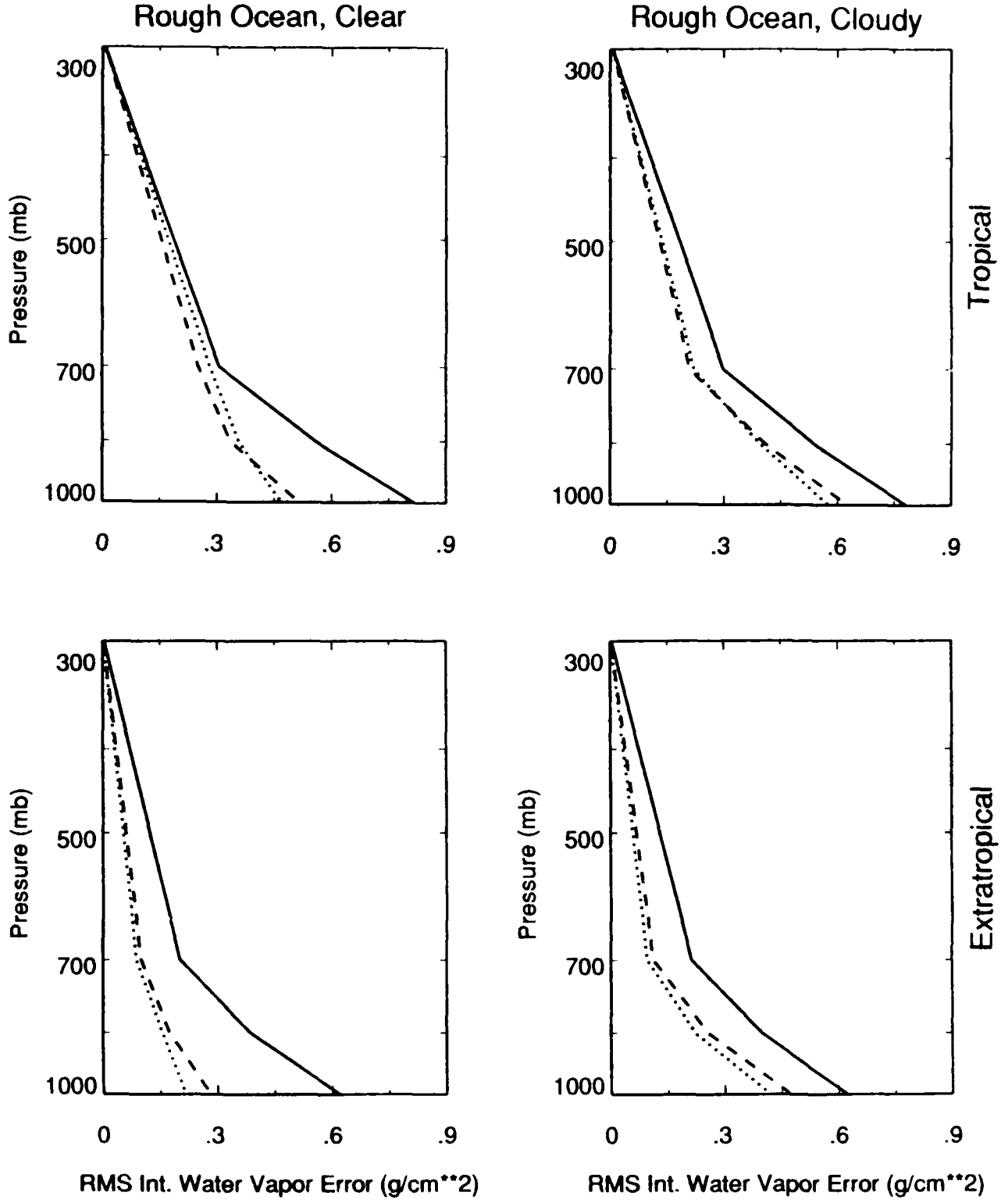

Figure 2.3. RMS integrated water vapor retrieval errors for various geophysical categories. Shown are climatology (solid), statistical first guess (dash), and unified retrieval (dot).

The mid-tropospheric rms error bulge is likely due to a problem of underdeterminacy (i.e., retrieving 11 level temperatures and 4 layers of moisture with only 12 SSM sounding channels). This can be addressed by determining the optimum combination of ridge parameters (σ in equation 2.15) which reduces the number of degrees of freedom in the problem so that the matrix inversion is more stable and a more consistent improvement in the temperature profile is seen. Additionally, it is well known that retrieving temperatures near the tropopause is difficult. The bulges in the rms T error profiles correspond to the lower part of the tropopause region in each category. The reason for the amplification of this error in the cloudy cases is not known.

For integrated water vapor the results show a marked improvement due to the physical retrieval in the layers 1-850 mb and 1-1000 mb. Even over a relatively high emissivity background such as ice, where detection of low level moisture is expected to be more difficult, the 1-1000 mb water vapor rms error is reduced by 10 to 25% (Figure 2.3a and 2.3b). Improvement in the water vapor profile retrieval is expected due to the physical retrieval's ability to treat the nonlinear relationship between water vapor and brightness temperature directly through the forward problem calculation. We find these results most encouraging.

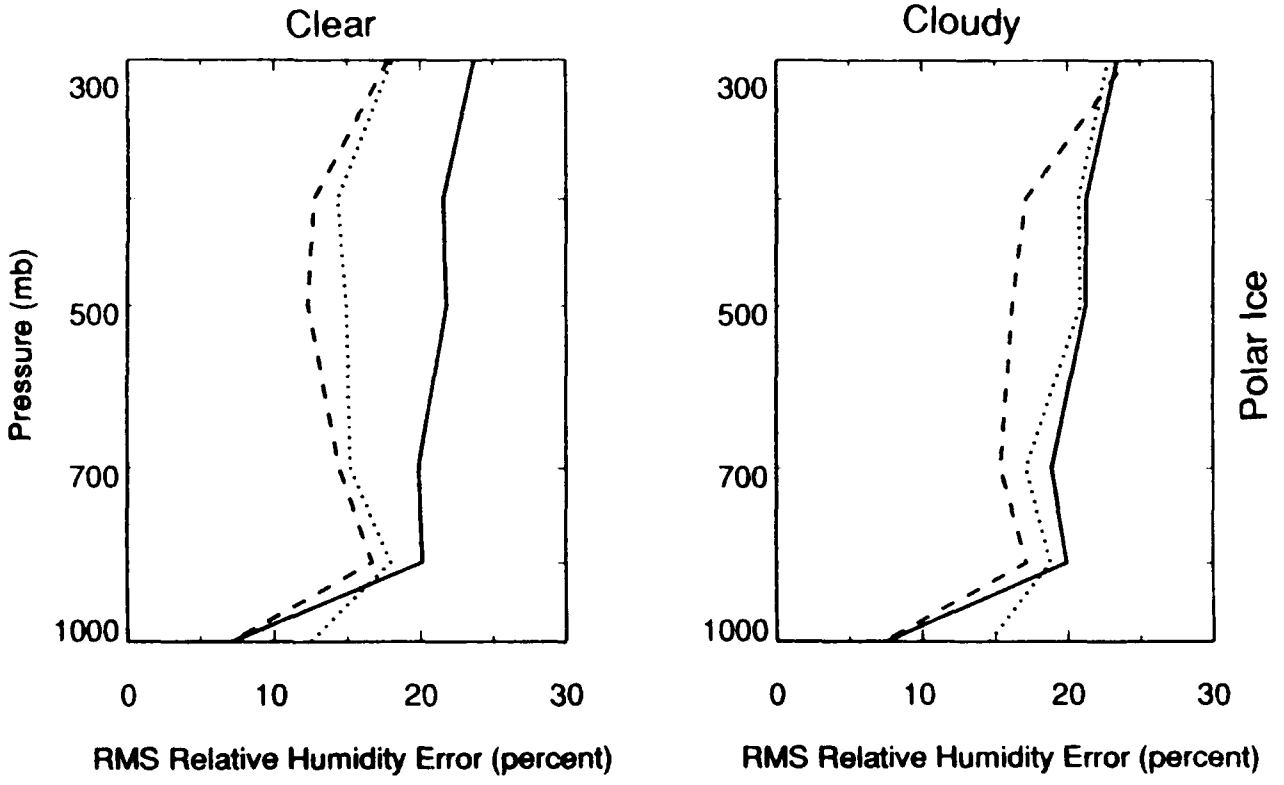

Figure 2.4. RMS relative humidity retrieval errors for various geophysical categories. Shown are climatology (solid), statistical first guess (dash), and unified retrieval (dot). (Continued . . .)

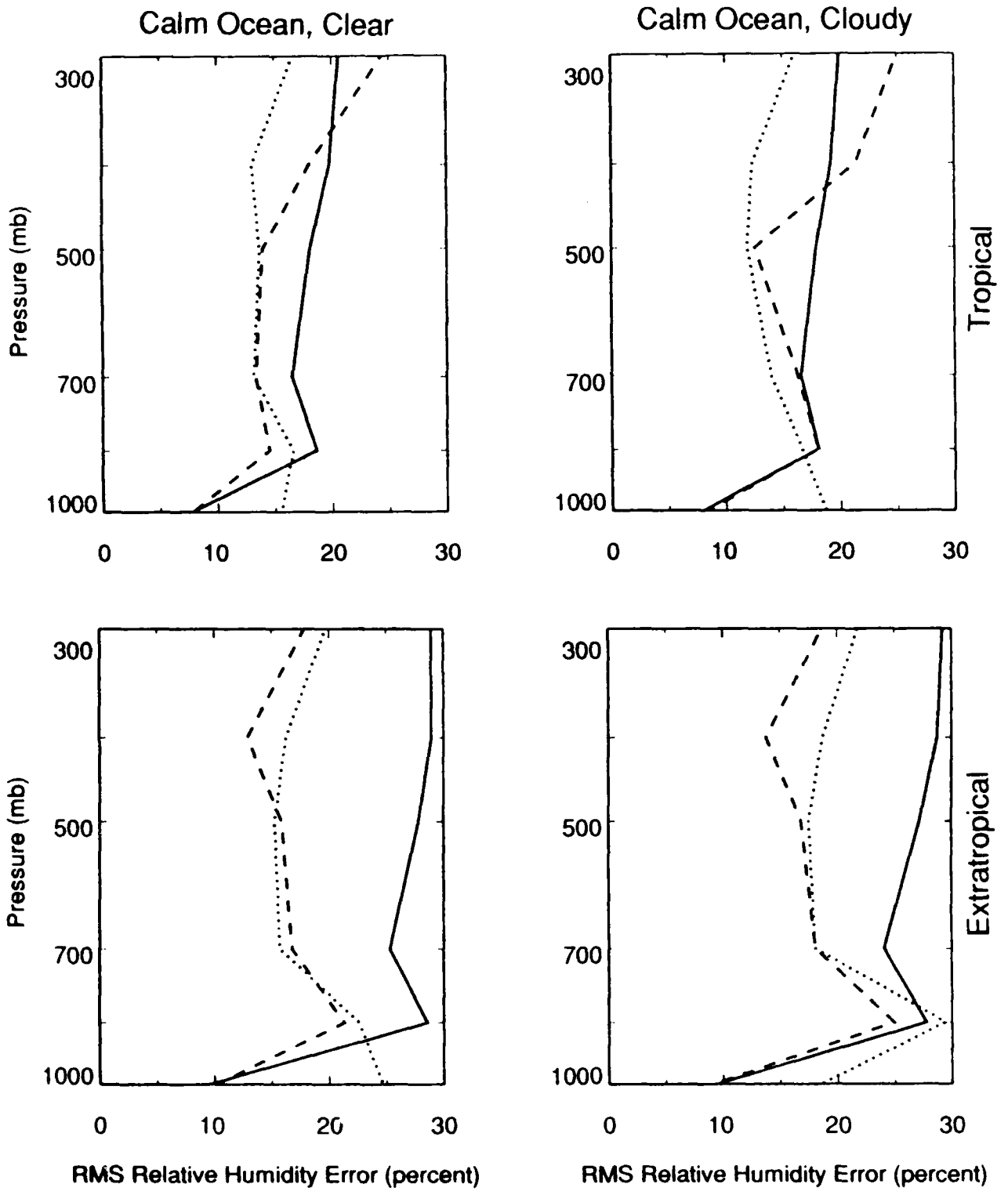

Figure 2.4. RMS relative humidity retrieval errors for various geophysical categories. Shown are climatology (solid), statistical first guess (dash), and unified retrieval (dot). (Continued . . .)

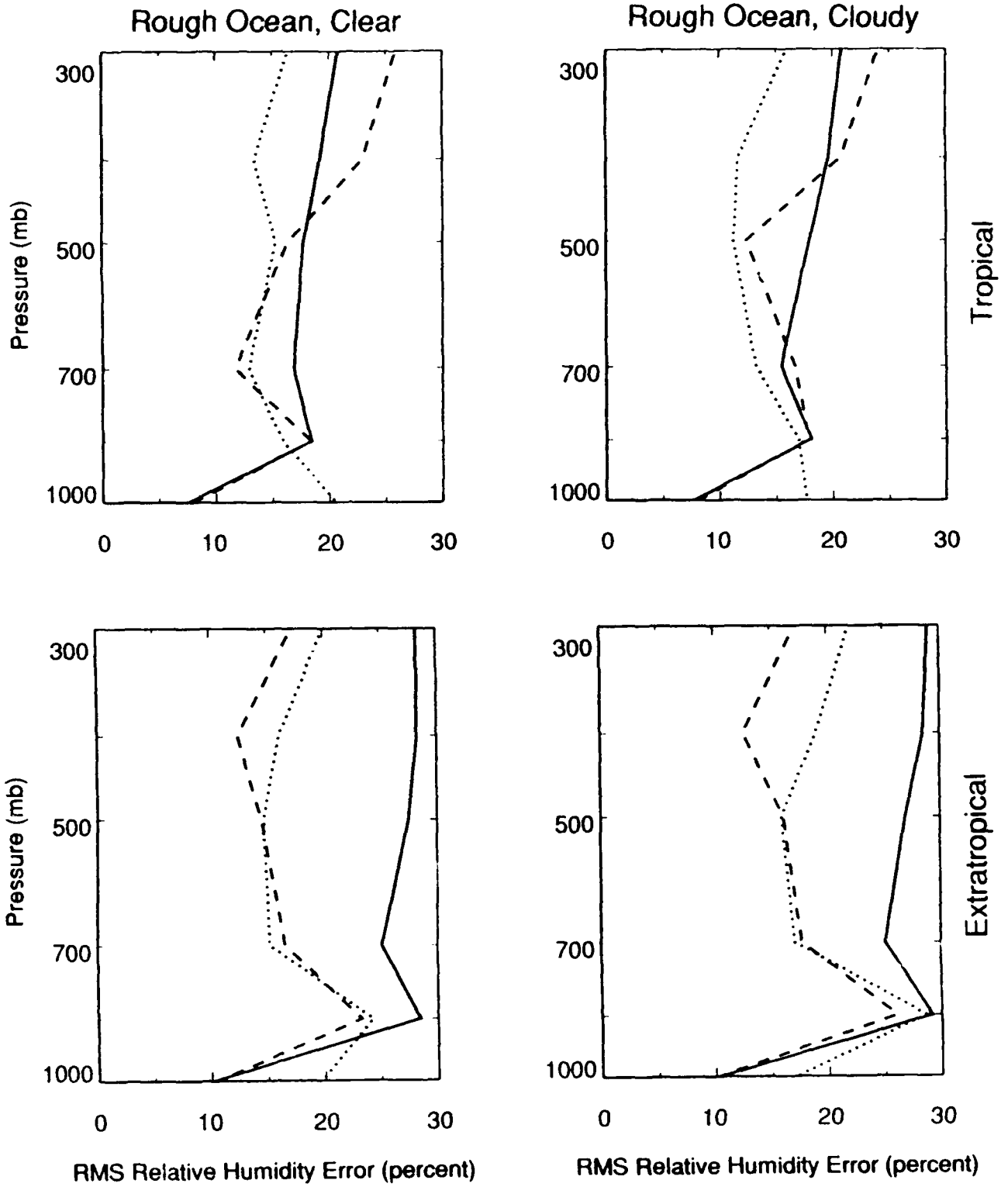

Figure 2.4. RMS relative humidity retrieval errors for various geophysical categories. Shown are climatology (solid), statistical first guess (dash), and unified retrieval (dot).

As indicated, moisture retrievals were converted to relative humidity (RH) to be consistent with the data assimilation system. In terms of RH, the results are quite variable (Figure 2.4). Only in the tropics does the physical retrieval improve upon the statistical retrieval. In the tropics the physical retrievals improve upon the first guess at 300 and 400 mb by 5 to 10% in terms of rms RH. Moreover, in cloudy situations the rmse is reduced at all levels except the surface. Retrieval of surface RH remains a problem in all categories with the error generally increasing by 10% rms. As depicted by the solid curves the climate standard deviation is very low, often less than 10%. This reflects the nearly saturated conditions which prevail, with mean 1000 mb RH greater than or equal to 90%. In the extratropics, on the other hand, the physical retrieval generally does not improve on the first guess.

These results raise the issue of whether or not RH is the most suitable variable for retrieval studies. Since RH is really a sensitive function of both the specific humidity and temperature, improving the temperature and/or specific humidity profile may not yield a corresponding improvement in the RH. Conversely, an improved RH retrieval may be the result of compensating errors in both T and q which really determine RH. This may, in part, explain why we obtain near universal improvements in integrated water vapor retrievals but only mixed results in terms of RH. Note that the temperature is better specified in the tropics (Fig. 2.2), where we do see improvements in RH. Additionally, interpolation errors introduced in converting the 4 layer integrated water profile to the 6 level RH profile could also have a negative effect.

In sum, the updated off-line unified retrieval results are far more encouraging than the preliminary retrievals which were used to run the OSSE. (Hereafter, these latter retrievals are termed the OSSE retrievals.) Extrapolating from these preliminary calculations we might anticipate positive impacts (relative to SSMSAT) upon RH analyses at mid and upper levels in the tropics and modest positive impacts upon the near surface T analysis over ice or other high emissivity surfaces. However, in other situations we might expect a negative impact.

In the statistical interpolation methodology used by our analysis procedures the statistical properties of the observational errors for each observation type must be specified. Because of the difficulty of characterizing these errors, we use simple models of the observational errors in the analysis procedures. In the case of the SSM/T data we do not directly use the statistical properties which were used to simulate the data. Instead we saved the actual errors used in simulating the OSSE retrievals and used them to develop global models of the observing errors for use in the analysis. For the current experiment we used the same error model for the analysis procedures as in the SSMSAT experiment except for the observational error standard deviations (OESDs) which were recalculated. The OESDs for both the statistical retrievals used in SSMSAT and the unified retrievals used in URSAT are shown in Figures 2.5 and 2.6. Each of these figures also include a curve corresponding to the offline retrievals discussed above. These latter curves were obtained by averaging the offline statistics over all categories. Considering first the height OESDs, we see that the errors of the OSSE retrievals are larger by about 10% than either the statistical retrievals or offline unified retrievals. By 50 mb the difference approaches 6 or 7 meters. The shape of these three error curves are very much the same. In terms of RH, the errors of the three SSM retrievals are comparable. The offline retrievals make a small improvement over the statistical retrievals, except at the surface. The OSSE retrievals are somewhat better than the statistical retrievals at and above 500 mb and somewhat worse near the surface. Compared to the OSSE

retrievals, the offline retrievals are better at 700 and 300 mb by almost 5%, but at other levels the impact of the updated retrieval sheme is neutral or slightly negative. The differences in the rms statistics are of order 2.5% RH. Based on these errors we should not expect the URSAT system to produce large positive analysis and forecast impacts.

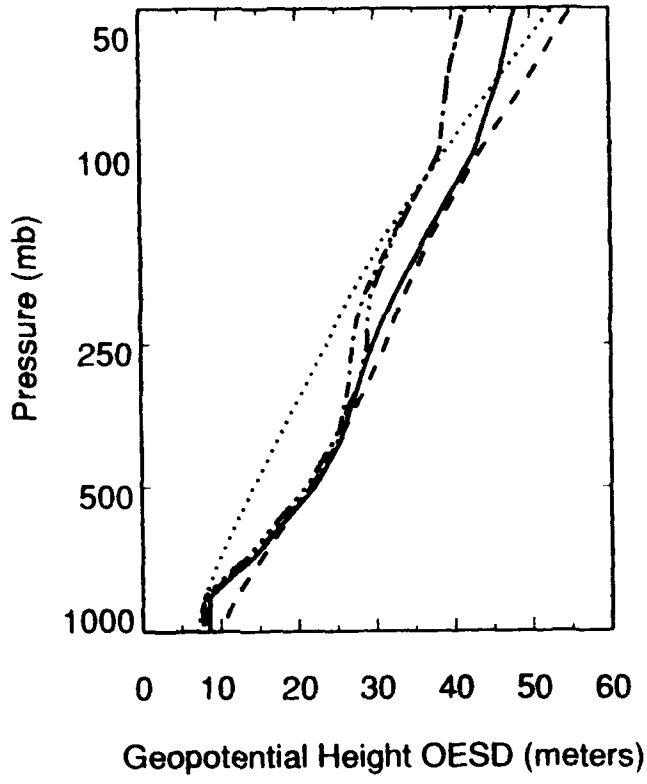

Figure 2.5. Geopotential height observational error standard deviations. Shown are OESDs for the URSAT OSSE unified retrievals (solid), SSMSAT statistical retrievals (dash-dot), TOVS statistical retrievals (dashed) and radiosondes (dotted). Also shown are estimates of the OESDs for the updated offline unified retrievals (dash-dot-dot-dot).

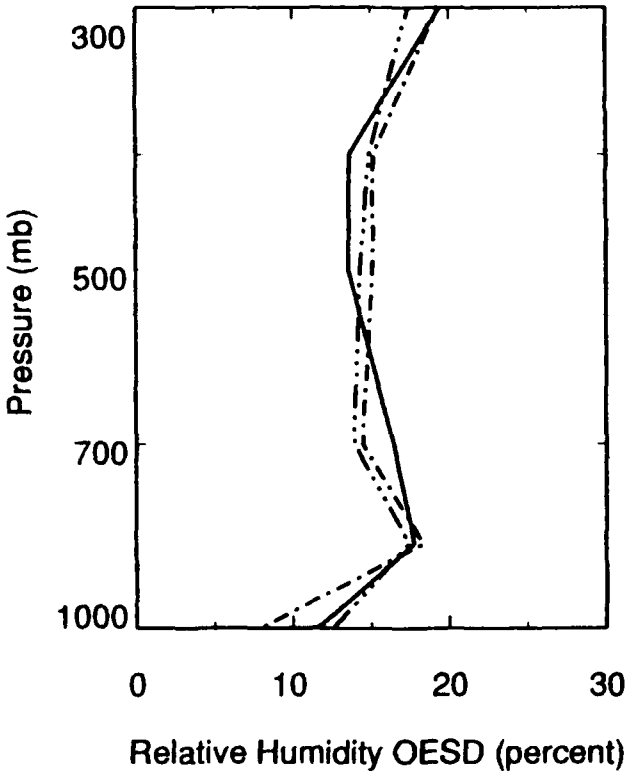

Figure 2.6. Relative humidity observational error standard deviations. Shown are OESDs for the URSAT OSSE unified retrievals (solid) and SSMSAT statistical retrievals (dash-dot). Also shown are estimates of the OESDs for the updated offline unified retrievals (dash-dot-dot-dot).

3. OSSE results

3.1 Experimental setup and summary of previous experiments

We have previously conducted a series of five OSSEs to assess the impact on the Air Force Geophysics Laboratory (GL) global data assimilation system (GDAS) of a satellite Doppler lidar wind sounder (WINDSAT) and of the Defense Meteorological Satellite Program (DMSP) Special Sensor Microwave (SSM) T-1 and T-2 instruments [18]. During the current study an additional OSSE, named URSAT has been performed to examine the impact of the unified retrieval methodology. In all, six OSSEs have been performed. These experiments are directly comparable, since the same data bases and procedures were used uniformly. For the current experiment, only the retrieval observations (i.e., unified rather than statistical retrievals) and their OESDs were changed. (See Figures 2.5 and 2.6.) The experiments are listed along with an indication of which data sources were used in each experiment in Table 3. In the experiments described in this section the preliminary or OSSE retrievals are used throughout. In addition to the Doppler wind lidar (DWL) and SSM data, the data sources include the conventional data (radiosondes, aircraft reports, etc.), cloud drift winds (CDW) and civilian satellite temperature retrievals (TOVS). The GL GDAS does not make use of surface observations. In a companion study [33] we reported results of a series of observing system experiments (OSEs) using the GL GDAS.

OSSE	Conventional	CDW	TOVS	SSM	DWL	UR
STATSAT	X	X	X			
NOSAT	X					
SSMSAT	X	X		X		
SSM+TOVS	X	X	X	X		
WINDSAT	X	X	X		X	
URSAT	X	X				X

Table 3. OSSE data sources summary.

As points of reference, NOSAT, STATSAT and WINDSAT OSSEs are used for comparison in this study. We remark that WINDSAT is a proposed instrument which is described in more detail by others [40, 9].

There are three components common to any OSSE:

1. A four dimensional reference atmosphere, often called the nature run. For the purpose of our experiments the nature run is considered to be the truth.
2. A sampling procedure to obtain observations and add appropriate errors.
3. A data assimilation system, composed of a forecast model and analysis procedure.

These components have been described in detail for our particular experiments in Sections 2, 3 and 4 of [18] with the exception of simulating the SSM UR errors. The SSM UR errors were described in the previous section of this report and the following paragraphs summarize the rest of the OSSE methodology. The sub-sections which follow describe our current experimental results and contrast and compare them to the results of [18].

Briefly, the ECMWF prepared the nature run, NMC simulated the GWE (Global Weather Experiment) Level II data base and the WINDSAT data and we simulated the SSM/T data. At a February 1983 Workshop at NMC, NMC, GLA and ECMWF agreed to jointly perform OSSEs to assess the impact of WINDSAT [11]. ECMWF generated the nature run by running their 15 level 1.875° resolution global grid point model for 20 days. NMC simulated all GWE Level IIb data for the same period by replacing each valid GWE observation by a simulated observation made up of the value of the nature run evaluated at the observing location plus a simulated observational error. In addition WINDSAT data were simulated at every TIROS sounding location down to cloud top. The various procedures used by Dey et al. [11] are recapitulated in Section 3 and Appendix A of [18]. Two series of experiments making use of these simulated data have been reported informally [2, 1].

Each simulated data assimilation experiment (OSSE) studied here consists of one assimilation run for seven days and three forecasts, each four days in length. Each OSSE runs from 00 UTC 18 November through 00 UTC 25 November and the 96 hour forecasts are made from 00 UTC 21, 23 and 25 November. Each assimilation run consists of a series of assimilation cycles, and each cycle in turn is made up of a 6-hour forecast that serves as the background or first guess field for the analysis, an optimum interpolation analysis which combines the first guess fields with the observations, and a nonlinear normal mode initialization of the analysis. The initialized analysis is the starting point for the next 6-hour forecast, which is then used as the first guess of the subsequent assimilation cycle. The GL global spectral model (GSM) [7, 6] is used for the 6-hour forecast in the GDAS as well as for the 96 h forecasts which start from days 3, 5 and 7 of the assimilation run. The AFGL Statistical Analysis Program (ASAP) [35, 36, 19] which is used to perform the analysis is a multivariate optimal interpolation procedure which operates in the model sigma domain.

For the most part the GL GDAS follows NMC practice. ASAP was developed from the NMC multivariate optimal interpolation (OI) procedure as described by [5] and [34]. The AFGL normal mode initialization (NMI) is based on the NMC NMI [3]. The AFGL GSM is based on the NMC GSM designed by Sela [41]. For the version used here, the physics routines are taken almost intact from NMC (circa 1983).

3.2 Synoptic examination of the analyses

We examined a selection of synoptic charts from experiment URSAT and compared them both to the Nature run and to corresponding results from SSMSAT. Generally, results from URSAT and SSMSAT are very similar. Differences which are present are due directly to the differences in the SSM data, are small scale and tend not to accumulate during the assimilation. To illustrate these findings we present a series of charts at the end of the 7 day assimilation period, 00 UTC 25 November, for 500 and 1000 mb height analyses.

Figure 3.1 shows the nature run. The wave number 4 present at 500 mb is dominant throughout the experimental period. URSAT captures the large scale features of the nature run (Figure 3.2). However there are many small scale differences, some of substantial magnitude as seen in Figure 3.3. Note the very large negative barotropic error in the mid north Pacific (about 55°).

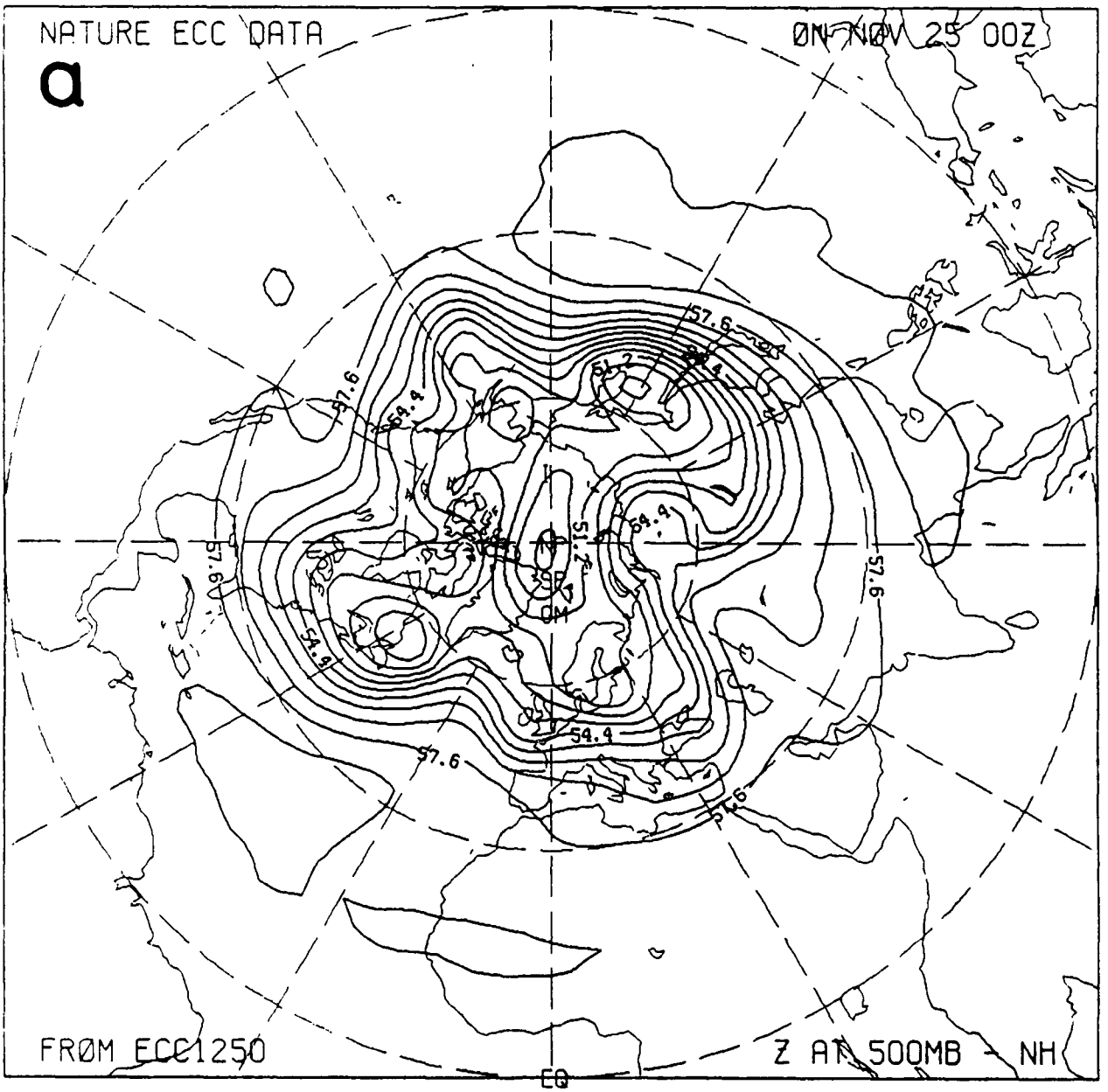

Figure 3.1. The nature run 500 hPa (a) and 1000 hPa (b) Northern Hemisphere height field at 00 UTC 25 November 1979. Here and below the 500 hPa height field is displayed with an 80 m contour level in hundreds of meters and the 1000 height field is displayed with an 40 m contour level in decameters. (Continued . . .)

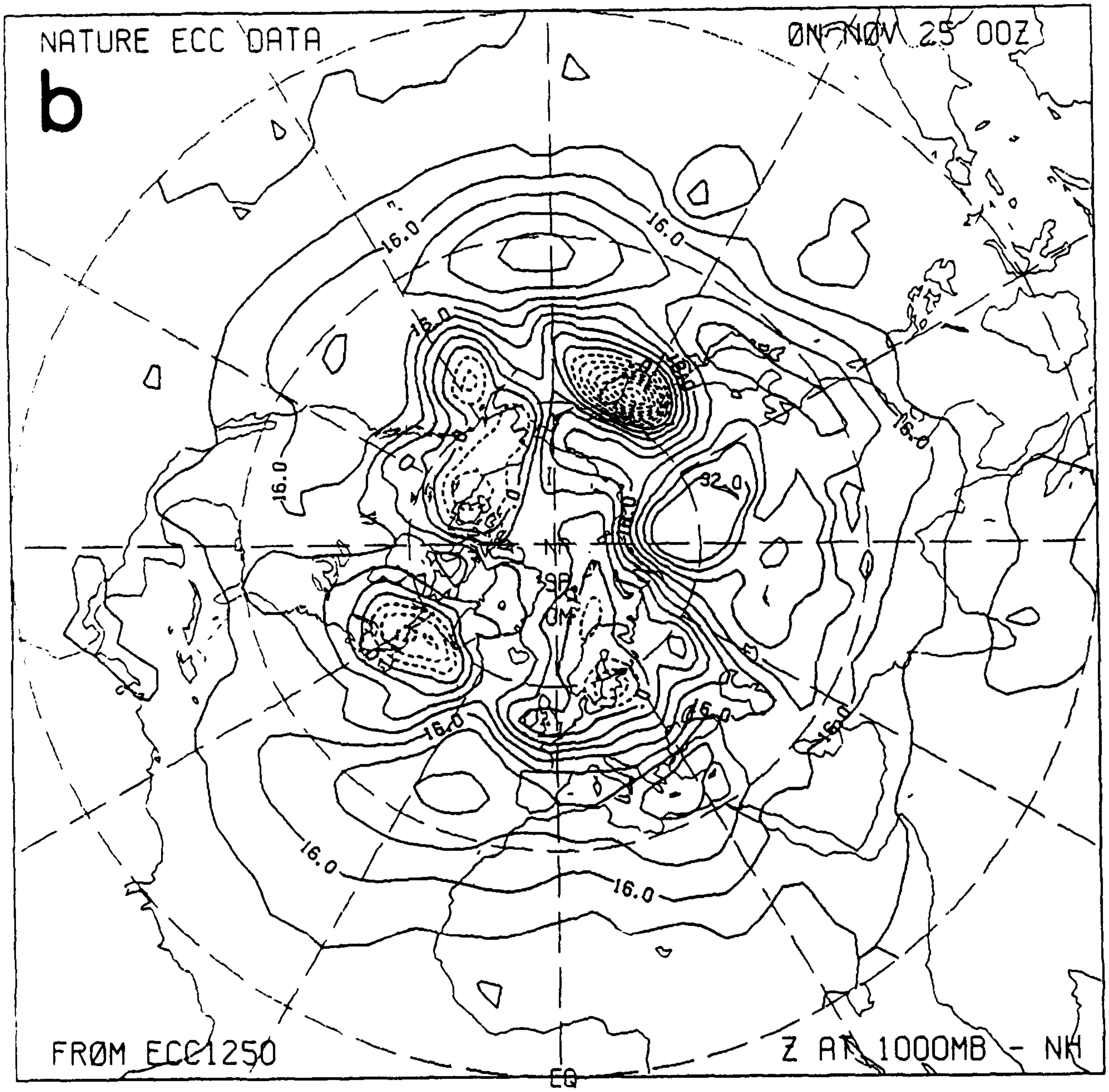

Figure 3.1. The nature run 500 hPa (a) and 1000 hPa (b) Northern Hemisphere height field at 00 UTC 25 November 1979. Here and below the 500 hPa height field is displayed with an 80 m contour level in hundreds of meters and the 1000 height field is displayed with an 40 m contour level in decameters.

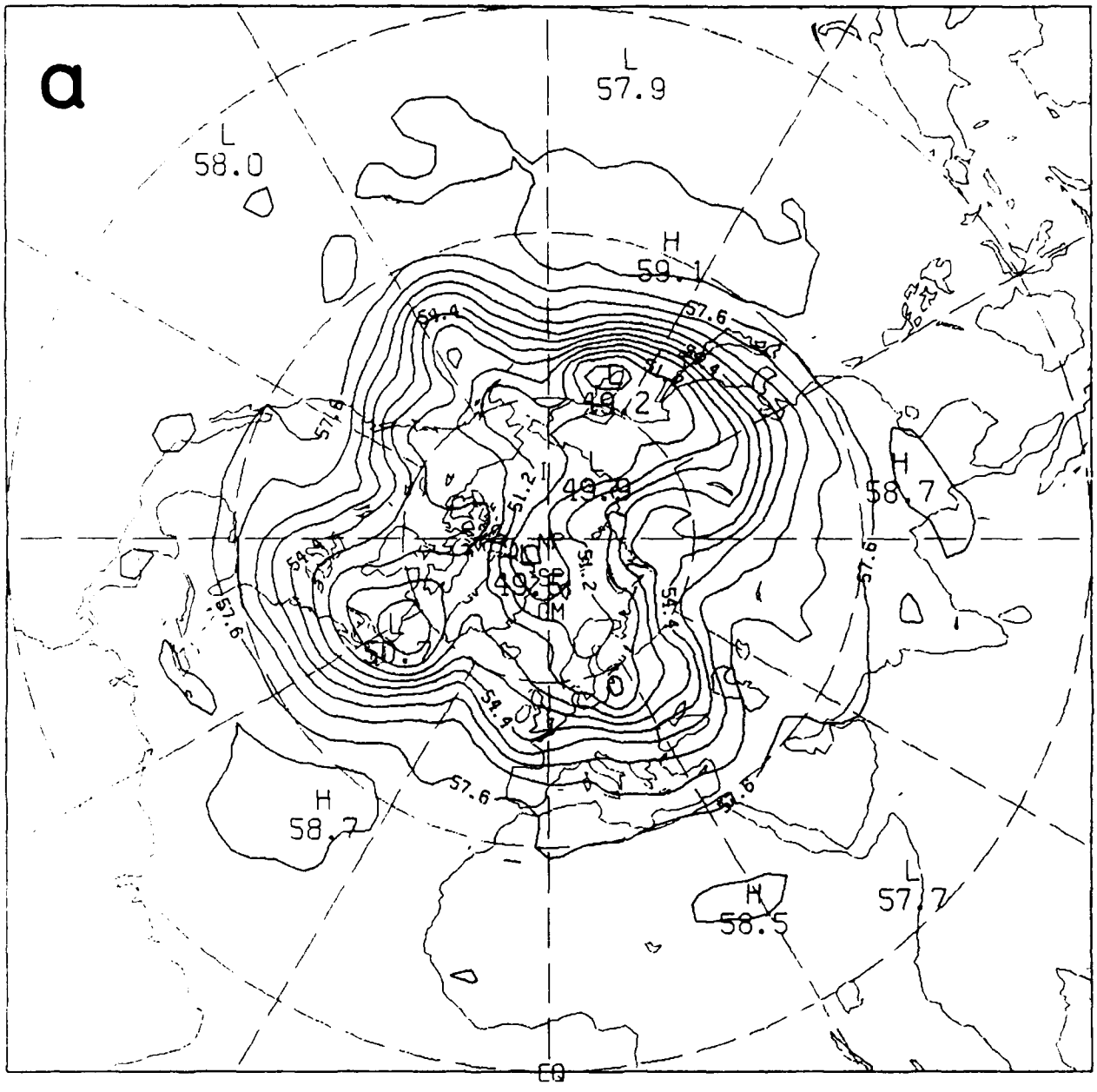

Figure 3.2. The same for URSAT. (Continued . . .)

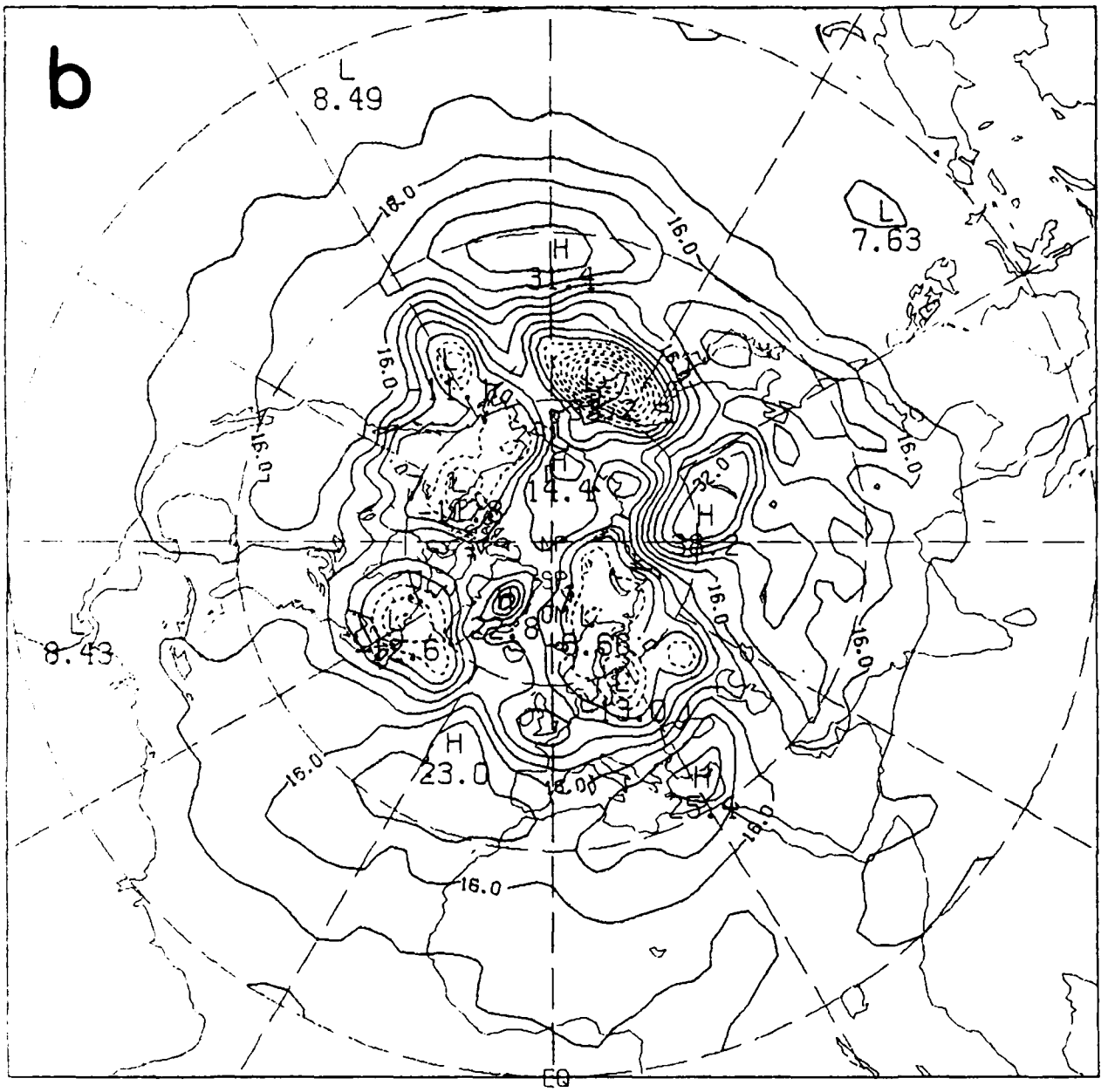

Figure 3.2. The same for URSAT.

The features of the URSAT analyses agree very well with the SSMSAT analyses. Even the analysis error charts look similar. Figure 3.4 is the SSMSAT analysis error comparable to the URSAT error displayed in Figure 3.3. Most of the features in Figure 3.3 have a corresponding feature in Figure 3.4. The errors are far from identical as can be seen in Figure 3.5, which shows URSAT - SSMSAT difference. (Note that the contour interval in this figure is 20 m as opposed to 40 m in the other difference maps.) Note that the differences in Figure 3.5 are concentrated

over the oceans and correlate well with the location of the SSM data available during the 6 h period used for the analyses (Figure 3.6).

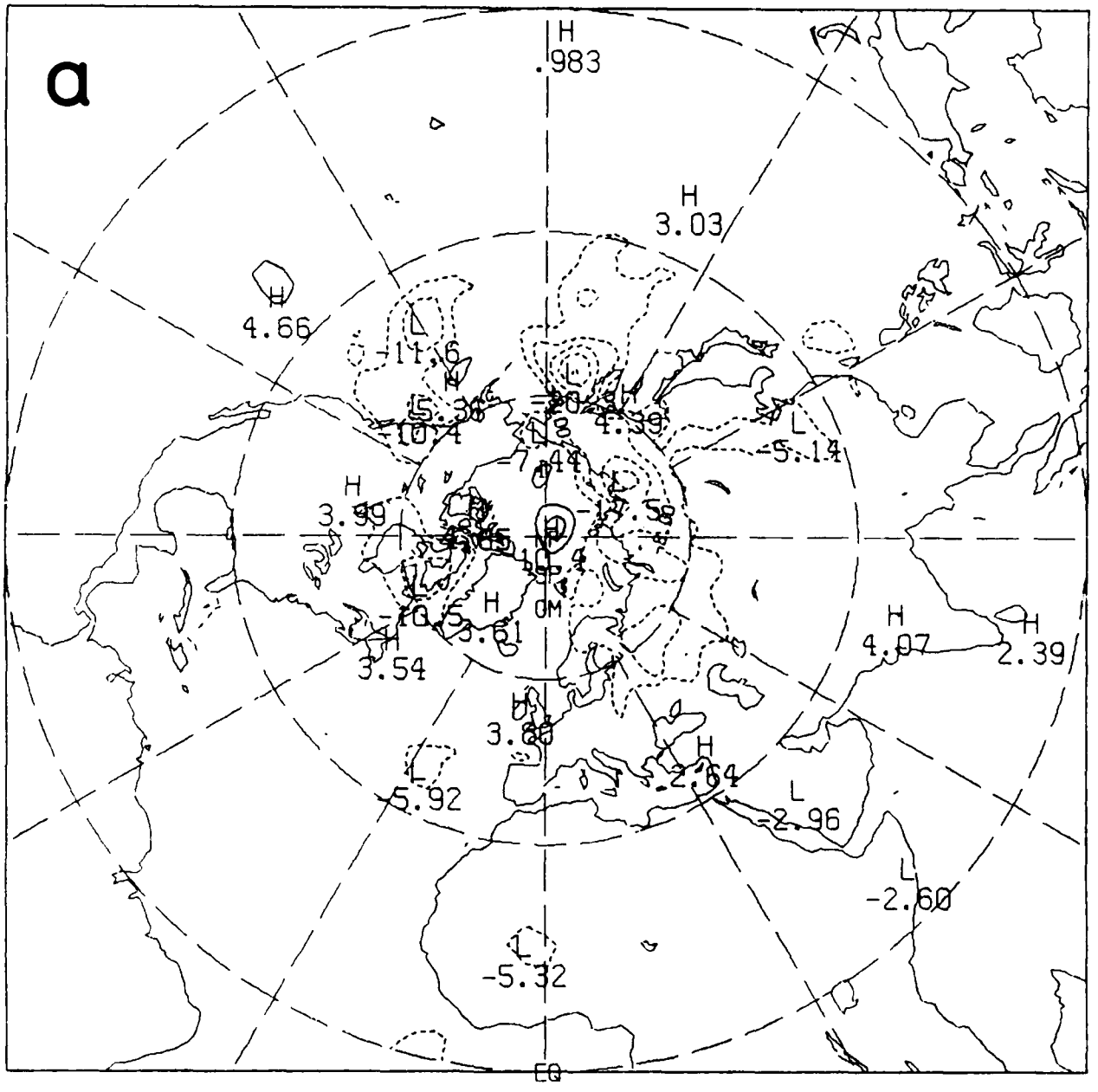

Figure 3.3. The URSAT assimilation error at 00 UTC 25 November 1979. Format as before. The errors are displayed with an 40 m contour level in decameters. (Continued . . .)

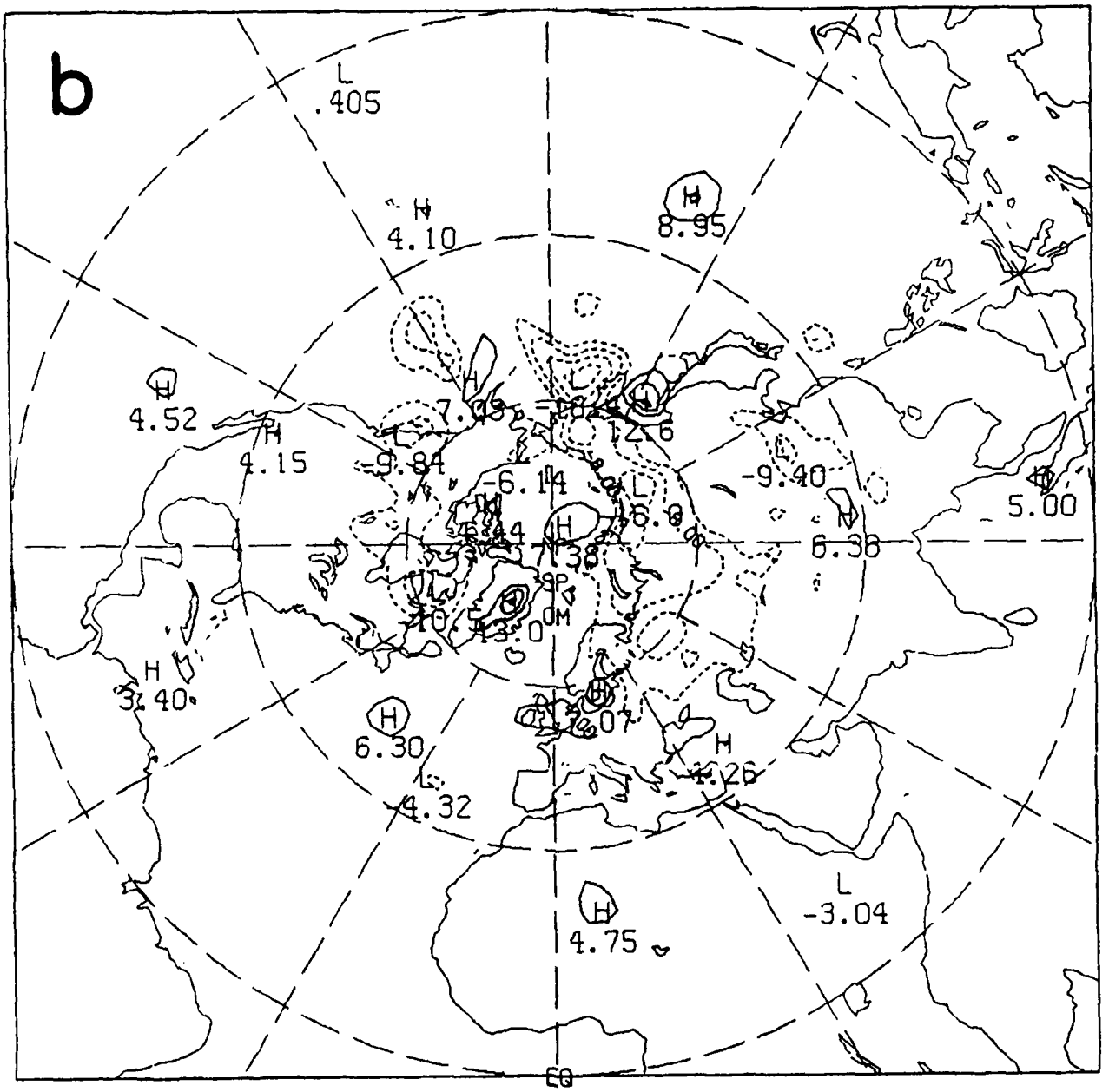

Figure 3.3. The URSAT assimilation error at 00 UTC 25 November 1979. Format as before. The errors are displayed with an 40 m contour level in decameters.

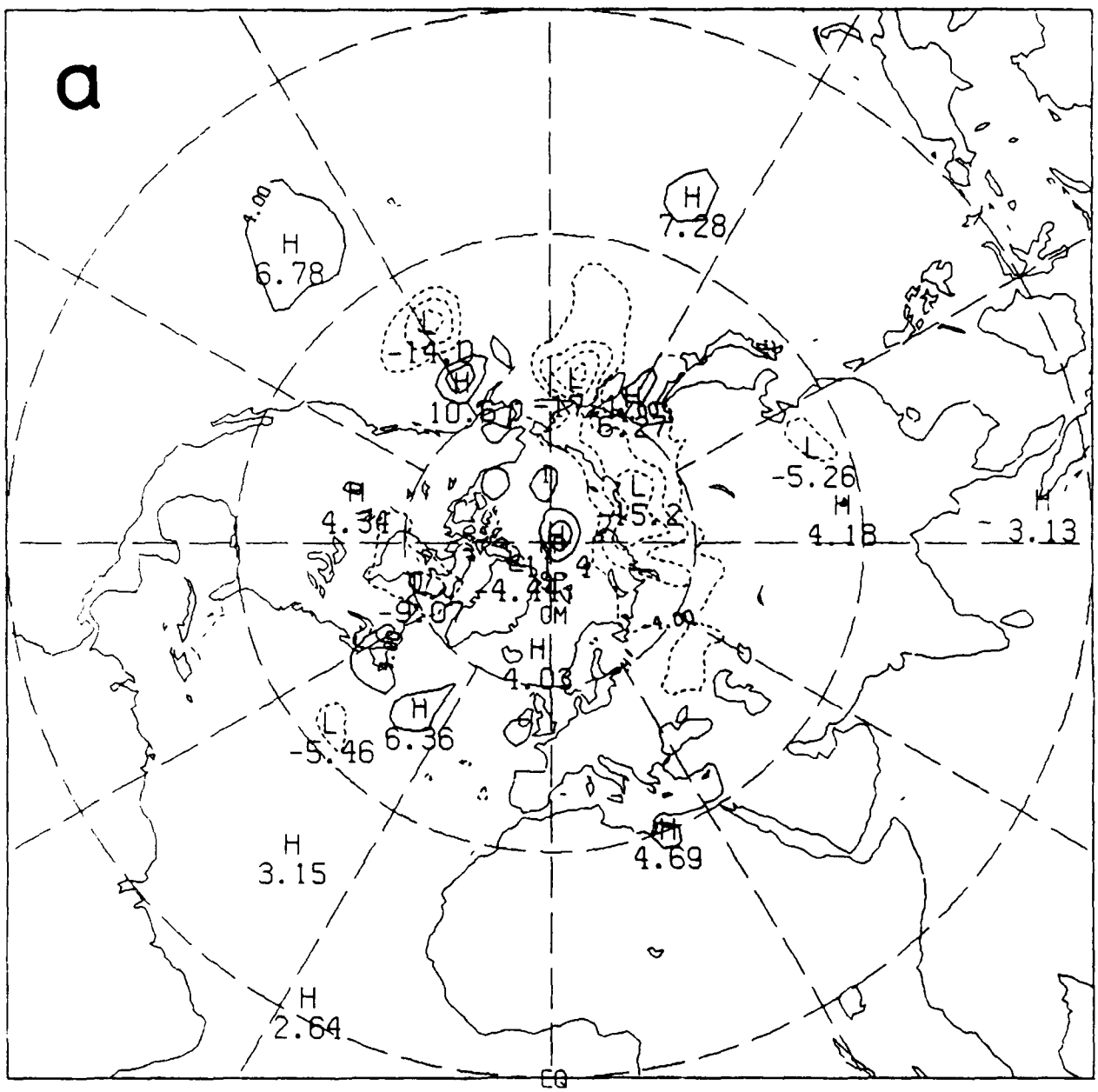

Figure 3.4. The same for SSMSAT. (Continued . . .)

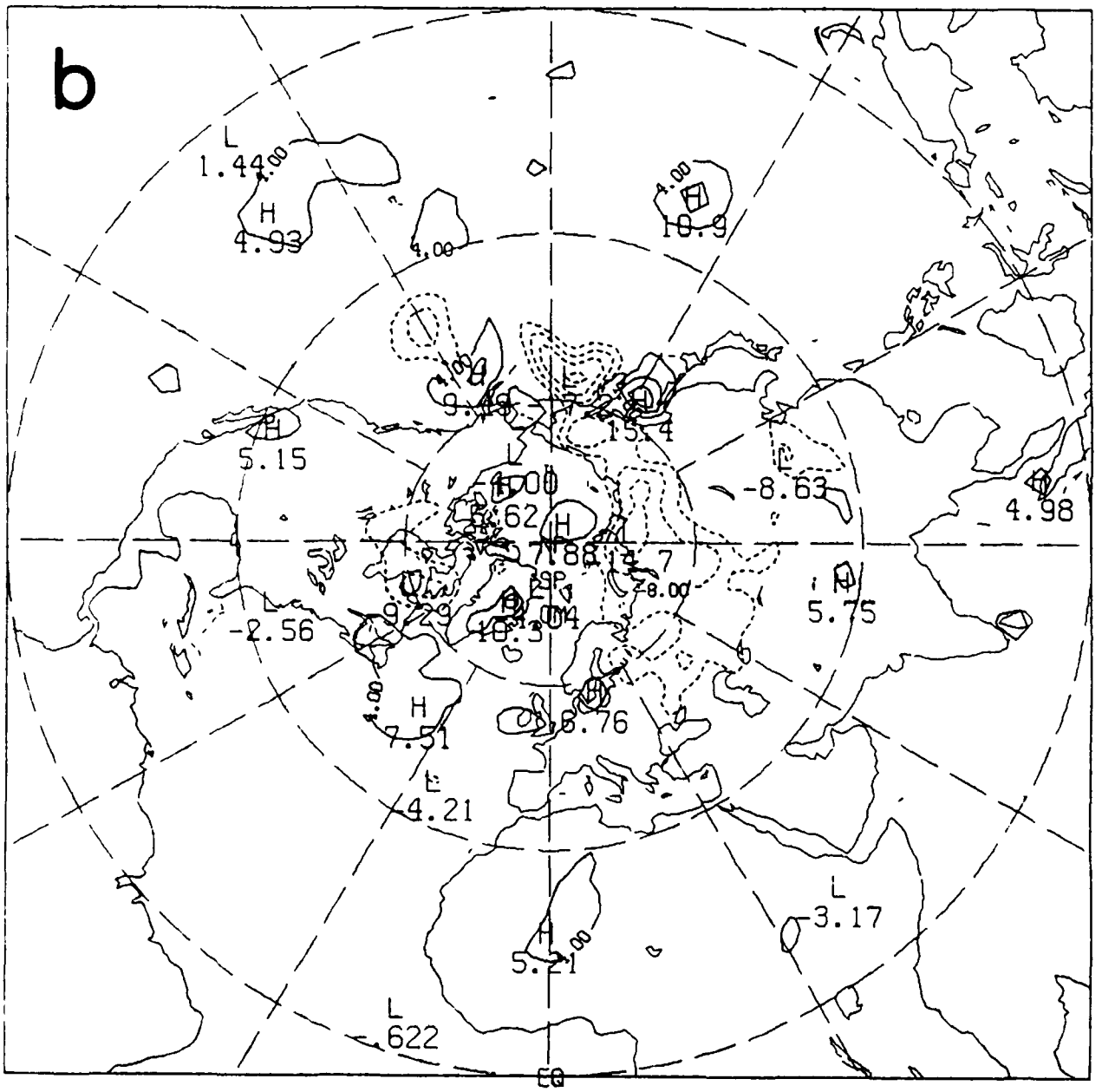

Figure 3.4. The same for SSMSAT.

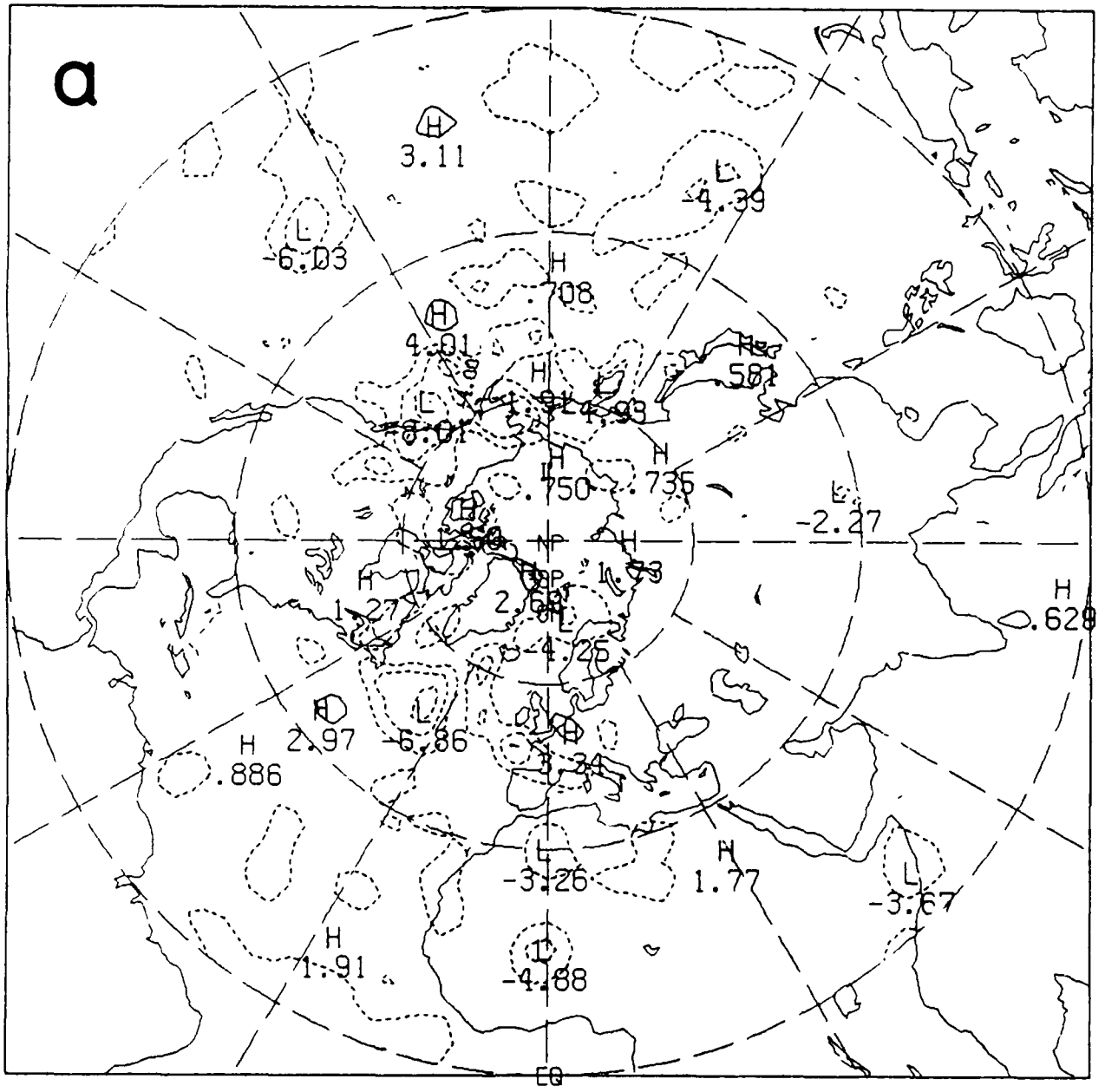

Figure 3.5. The URSAT - SSMSAT assimilation difference at 00 UTC 25 November 1979. Format as before. The differences are displayed with an 20 m contour level in decameters. (Continued . . .)

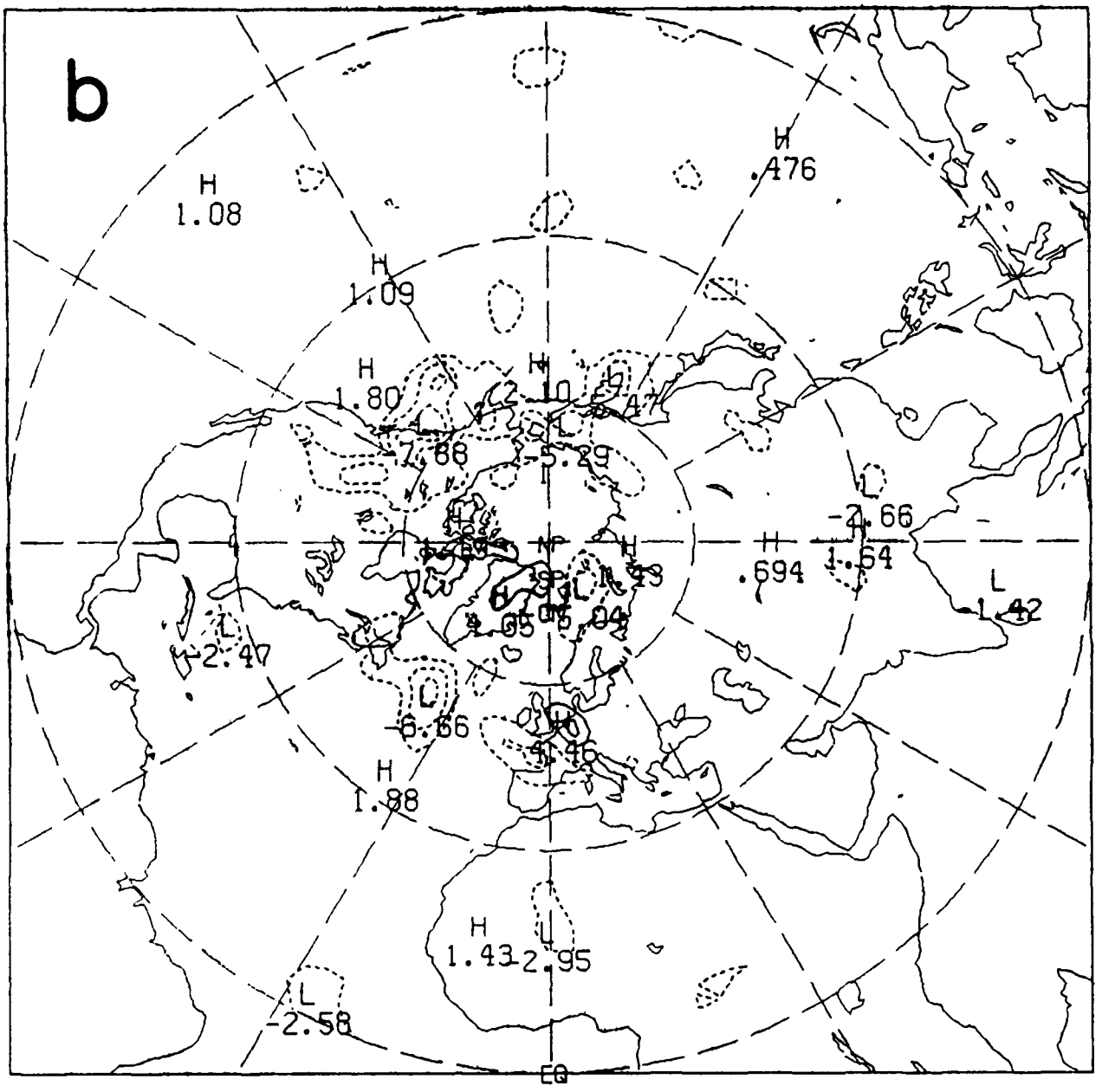

Figure 3.5. The URSAT - SSMSAT assimilation difference at 00 UTC 25 November 1979. Format as before. The differences are displayed with an 20 m contour level in decameters.

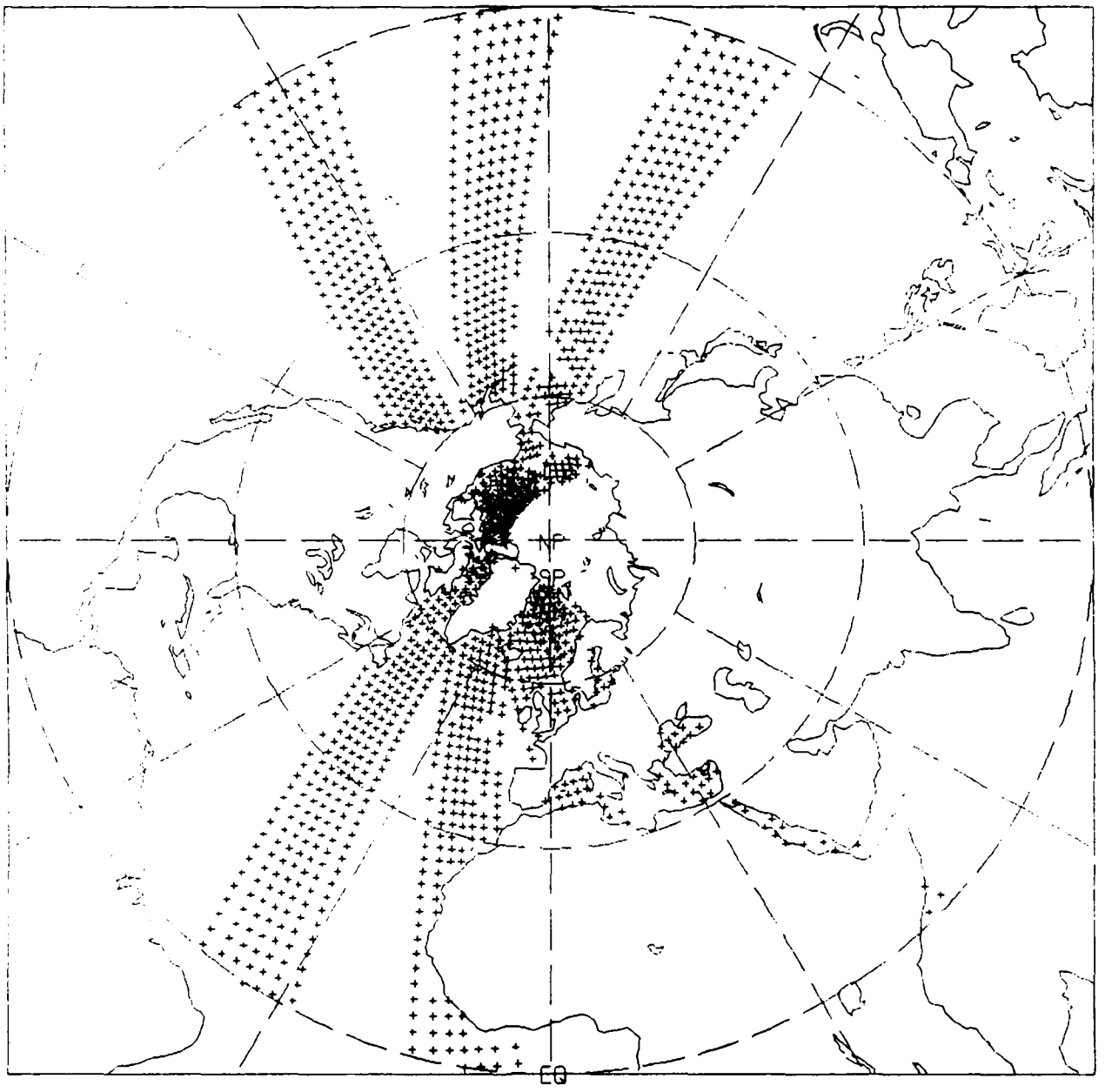

Figure 3.6. Simulated SSM/T data coverage for heights at $\sigma = 0.5$ in the Northern Hemisphere for the 6 h period centered on 00 UTC 25 November 1979 which have passed the analysis procedures gross and buddy checks.

3.3 Analysis impacts

To quantify the analysis errors we computed rms errors for different latitude zones for different variables, every 12 hours during the assimilation period. Four of the experiments described previously are used for comparison. The latitude zones defined here are the Northern

Hemisphere extratropics (20°N-80°N), tropics (20°S-20°N) and Southern Hemisphere extratropics (80°S-20°S). Note that because of the simulation nature of the current experiments, we know the truth and the difference statistics we calculate are truly errors.

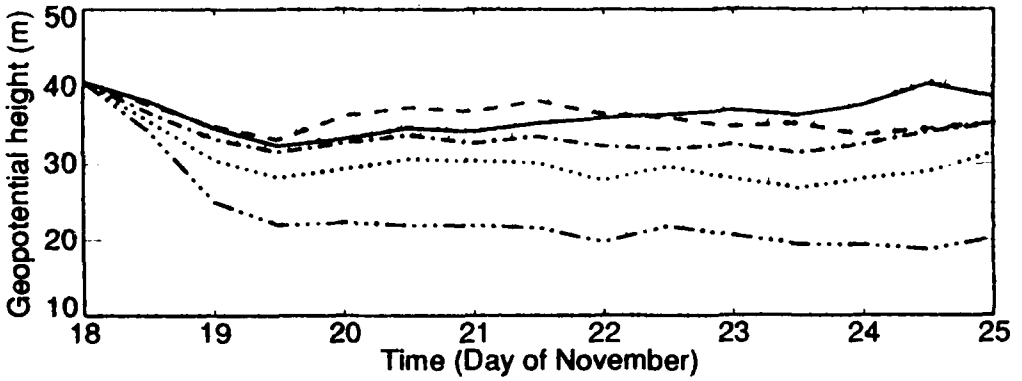

Figure 3.7. Evolution of Northern Hemisphere rms 500 hPa height error during the URSAT (solid), STATSAT (dash), NOSAT (dot), SSMSAT (dash-dot) and WINDSAT (dash-dot-dot-dot) OSSEs.

Figures 3.7 and 3.8 show the evolution of the analysis error of the 500 mb height error in the Northern Hemisphere extratropics and in the Southern Hemisphere extratopics. The three satellite sounding systems result in a slight degradation of the NOSAT system in the Northern Hemisphere. The satellite data are poor quality compared to the first guess available in the Northern Hemisphere and the statistics used in the analysis system are not optimal. The URSAT results are quite similar in quality to the SSMSAT results ior the first half of the data assimilation period, both being somewhat better than STATSAT. However, during the second half of the period the relative ranking of URSAT and STATSAT reverse. We can offer no definite explanation for the monotonic increase of the URSAT error from 12 UTC 19 November onward. It might be a statistical fluctuation or it might be caused by the greater OESDs associated with the preliminary unified retrievals for height. However, in support of the former possibility, we note that, in the Southern Hemisphere there is no difference between the quality of the 500 mb analyses of URSAT and SSMSAT during the entire week long period.

We now turn to root mean square errors, where the mean is over time and space, as a function of pressure. The rms height errors for the 3 geographical regions show relatively smooth changes with height through the depth of the troposphere (Figures 3.9, 3.10 and 3.11). The size of the height errors for the Northern Hemisphere is remarkably constant from the surface through the 70 mb level. The tropical errors are smaller than the extratropical errors since the variability of the height field in the tropics is so small. The SSM data are seen to improve the height analysis relative to the STATSAT experiment by a few meters at all levels. The height errors grow slowly with decreasing pressure, because the largest components are due to errors in the analysis of surface pressure and lowest layer temperature. Both these effects combine to produce large 1000 mb temperature errors, as is seen in Figures 3.12, 3.13 and 3.14, which are analogous to the previous three figures. The accuracy of the temperature analyses of SSMSAT and URSAT are very similar except in the tropics, where URSAT is superior near the surface and SSMSAT is superior in the tropopause region.

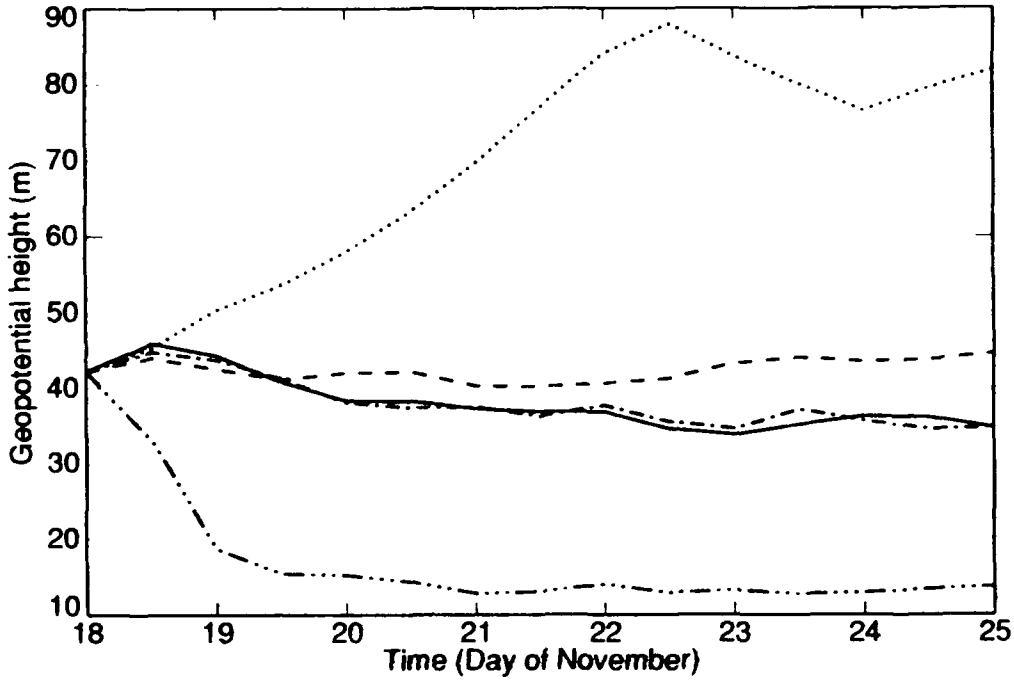

Figure 3.8. The same for the Southern Hemisphere.

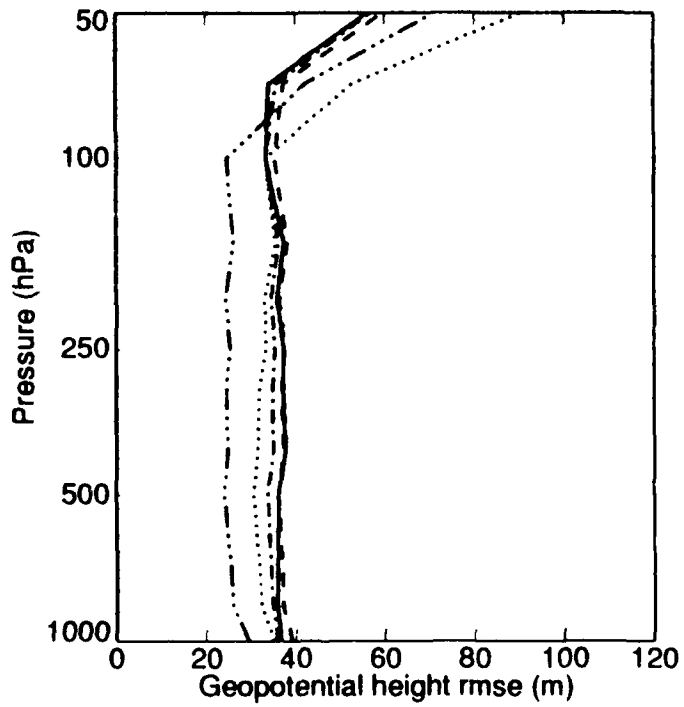

Figure 3.9. Rms height assimilation errors as a function of pressure for the Northern Hemisphere for the URSAT (solid), STATSAT (dash), NOSAT (dot), SSMSAT (dash-dot) and WINDSAT (dash-dot-dot-dot) OSSEs.

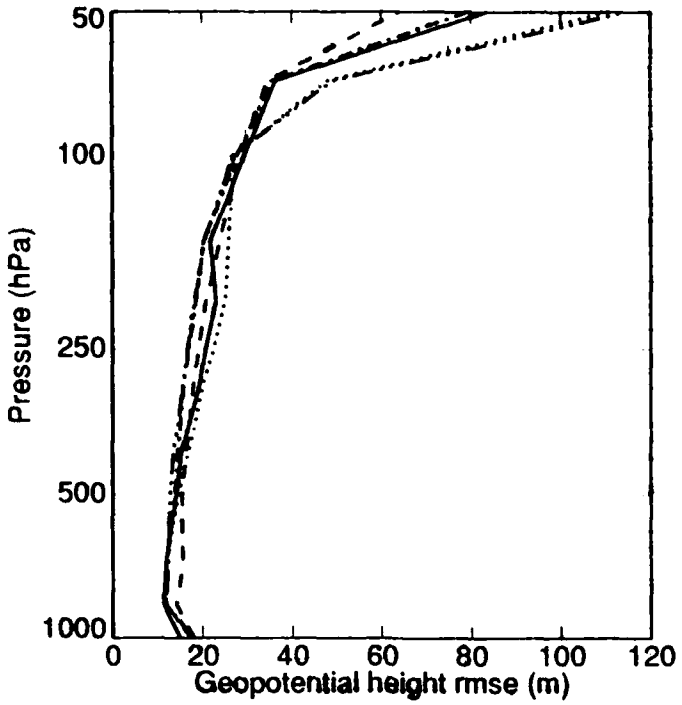

Figure 3.10. The same for the tropics.

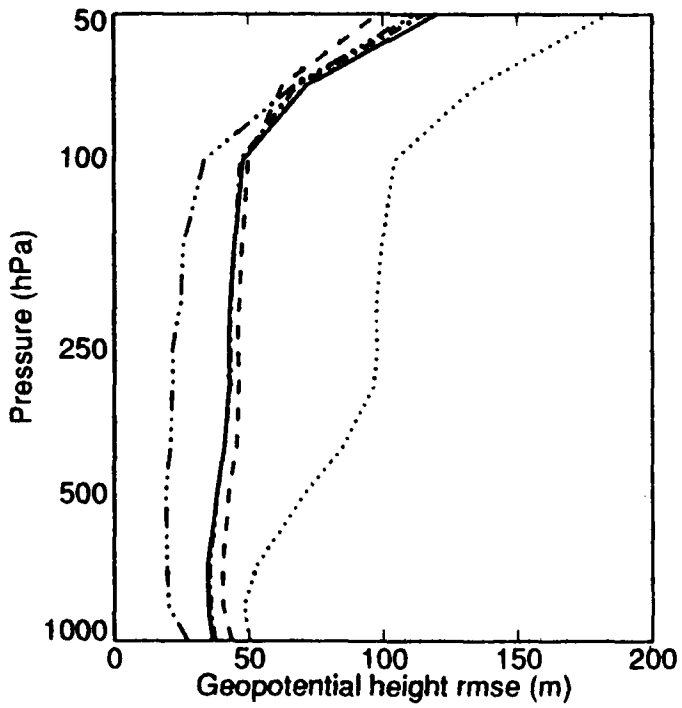

Figure 3.11. The same for the Southern Hemisphere.

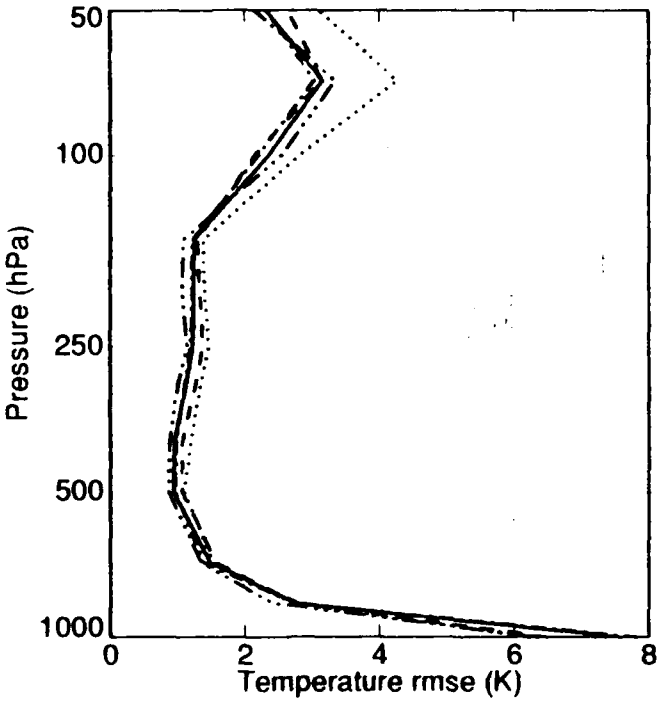

Figure 3.12. Rms temperature assimilation errors as a function of pressure for the Northern Hemisphere for the URSAT (solid), STATSAT (dash), NOSAT (dot), SSMSAT (dash-dot) and WINDSAT (dash-dot-dot-dot) OSSEs.

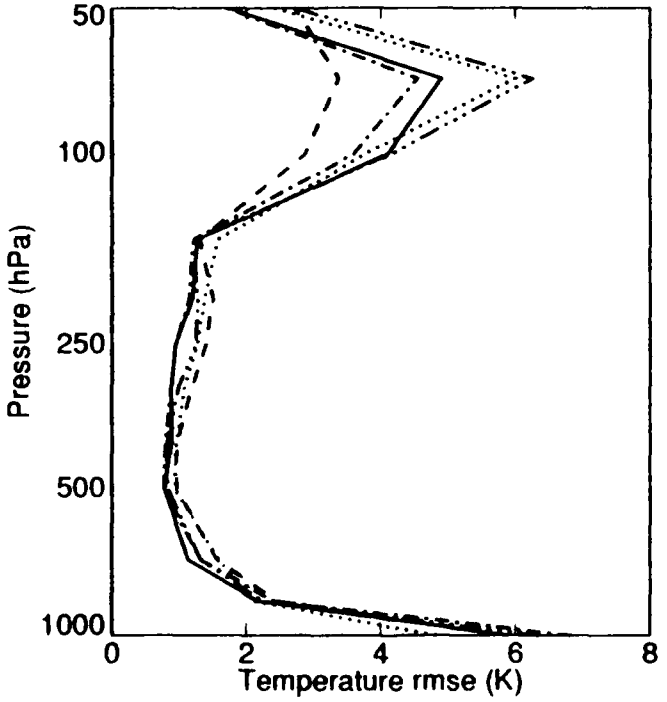

Figure 3.13. The same for the tropics.

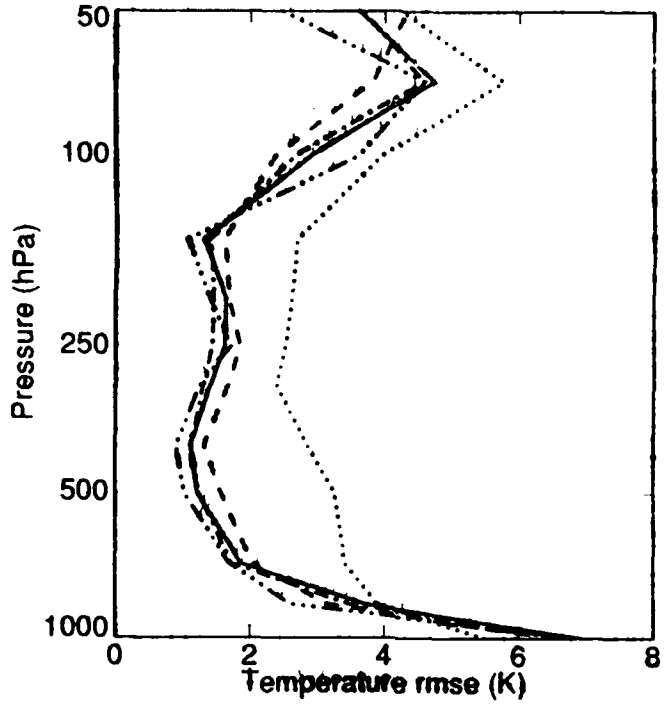

Figure 3.14. The same for the Southern Hemisphere.

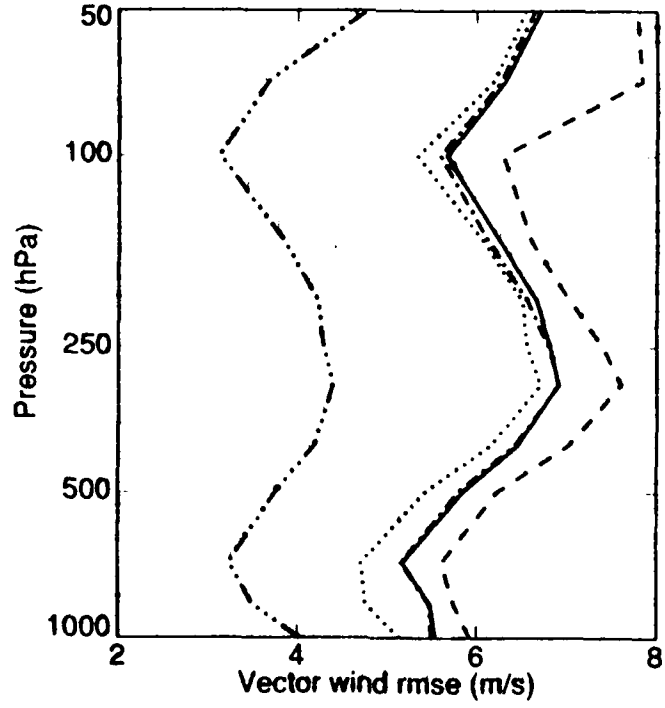

Figure 3.15. Rms vector wind assimilation errors as a function of pressure for the Northern Hemisphere for the URSAT (solid), STATSAT (dash), NOSAT (dot), SSMSAT (dash-dot) and WINDSAT (dash-dot-dot-dot) OSSEs.

The rms vector wind errors for URSAT and SSMSAT are nearly identical (Figures 3.15, 3.16 and 3.17). Even at 100 mb in the tropics where there is a significant negative impact of UR on the temperature error of the OSSE retrievals, there is no impact on the wind analysis. Both URSAT and SSMSAT are a significant improvement over STATSAT. This is reasonable, since the wind analysis increment respond to gradients in the observed heights, not the heights themselves and a large part of the OSSE retrieval errors at 100 mb in the tropics is a warm bias error.

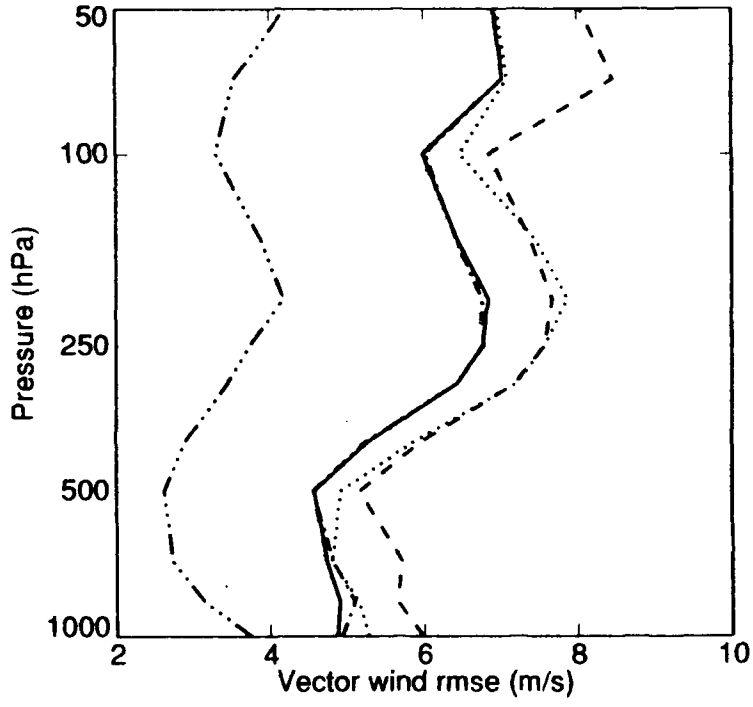

Figure 3.16. The same for the tropics.

We now turn to the relative humidity analyses (Figures 3.18, 3.19 and 3.20). In the Northern Hemisphere, URSAT is roughly equivalent to NOSAT and about 2% worse than SSMSAT. In the Southern Hemisphere and tropics, URSAT is roughly 5% worse than SSMSAT. The OSSE retrievals have not extracted any useful humidity information and the 5% relative humidity analysis improvement of SSMSAT over STATSAT is mitigated. Actually the RH retrievals of URSAT are no better or worse than those of SSMSAT (see Fig. 2.6), so the negative effect of the poorer height retrievals (see Fig. 2.5) must be propagating through the data assimilation system to influence the RH analyses. Again, it is emphasized that these impacts (and the forecast impacts to follow) are based on the poorer quality OSSE retrievals and not on the updated retrieval results described in section 2.

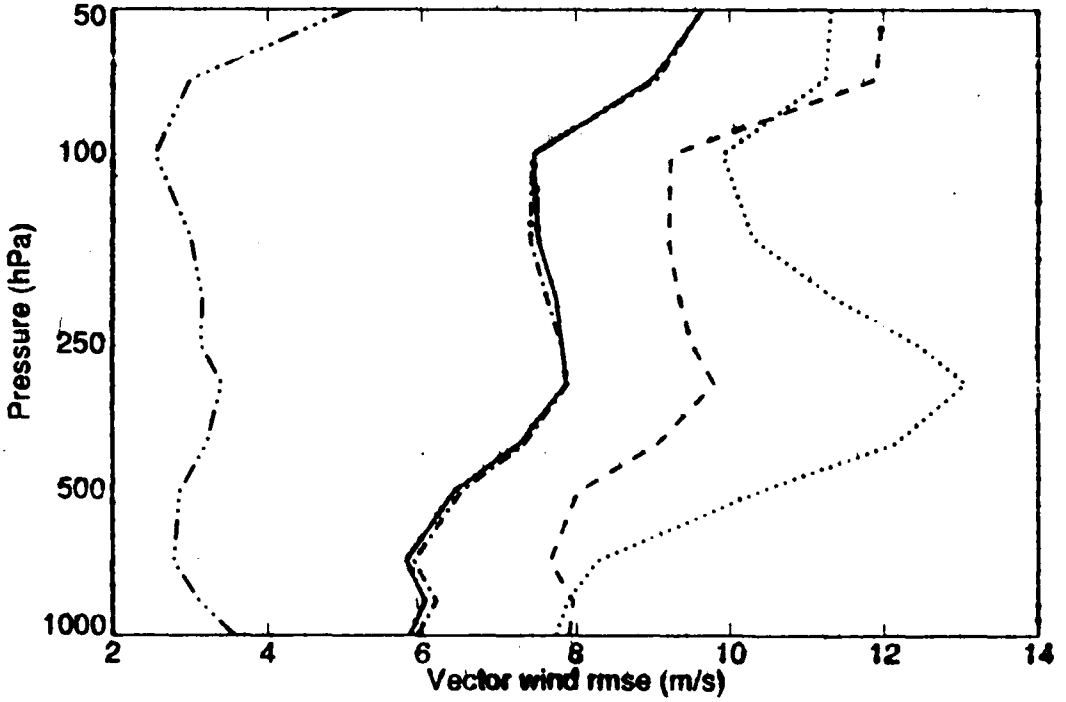

Figure 3.17. The same for the Southern Hemisphere.

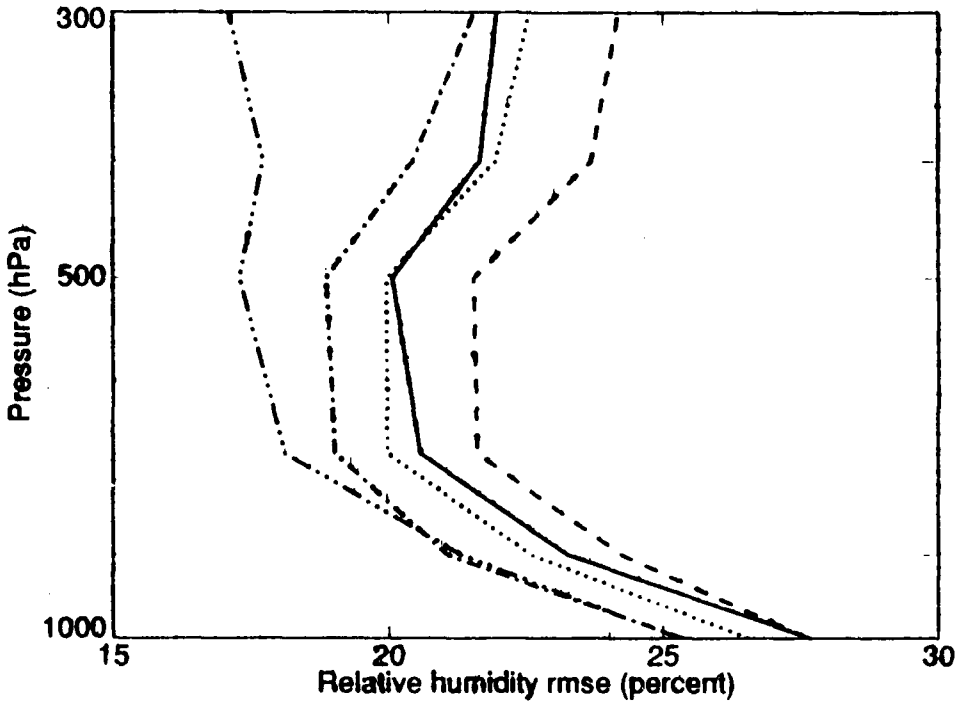

Figure 3.18. Rms relative humidity assimilation errors as a function of pressure for the Northern Hemisphere for the URSAT (solid), STATSAT (dash), NOSAT (dot), SSMSAT (dash-dot) and WINDSAT (dash-dot-dot-dot) OSSEs.

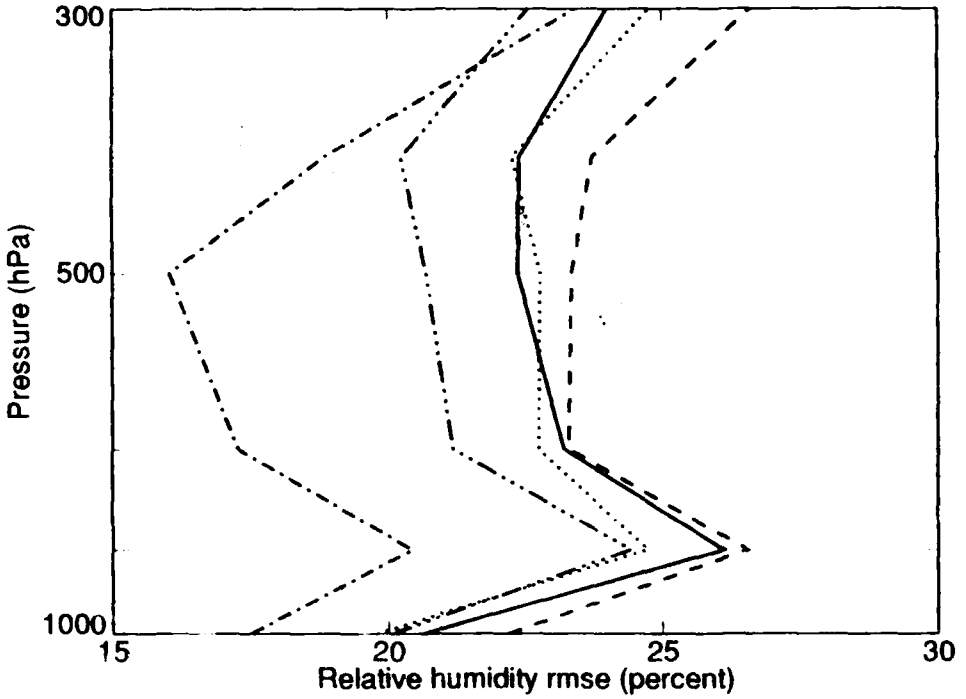

Figure 3.19. The same for the tropics.

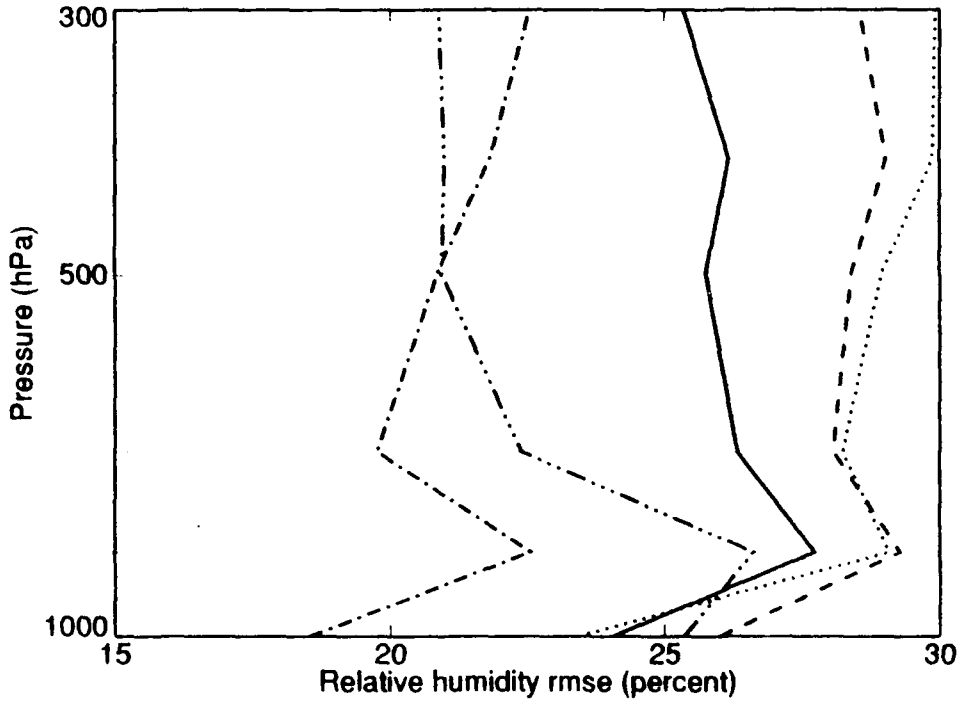

Figure 3.20. The same for the Southern Hemisphere.

3.4 Forecast impacts

The forecast impacts of URSAT relative to SSMSAT are relatively small. We calculate these impacts by calculating rms differences between the forecast fields and the simulated radiosonde observations. We used this methodology in the current study to enable a comparison with our previous results for OSSEs [17]. (In that study [17] we compared our forecasts to radiosondes to facilitate a comparison with our previous real data OSEs [33].) At particular synoptic times, for particular levels and variables, URSAT may be better or worse than SSMSAT. Overall the impact is neutral. In the Southern Hemisphere and in the tropics, jaggedness in these curves is due to the small radiosonde sample and do not reflect significant differences in forecast skill.

We present in Figures 3.21, 3.22 and 3.23 the rms forecast error for 500 mb height for each of the OSSEs listed in Table 3 for the three latitude zones. These results are rms over the three forecasts and the horizontal region. Figures 3.24, 3.25 and 3.26 present the same information for the 200 mb wind vector error and Figures 3.27, 3.28 and 3.29 for the 850 mb relative humidity error. The forecast error time evolutions shown are generally representative of other levels. This seems to hold particularly well for the Northern Hemisphere extratropics. In Figures 3.30 through 3.38, we present the vertical profiles at forecast hour 96 averaged corresponding to the previous figures.

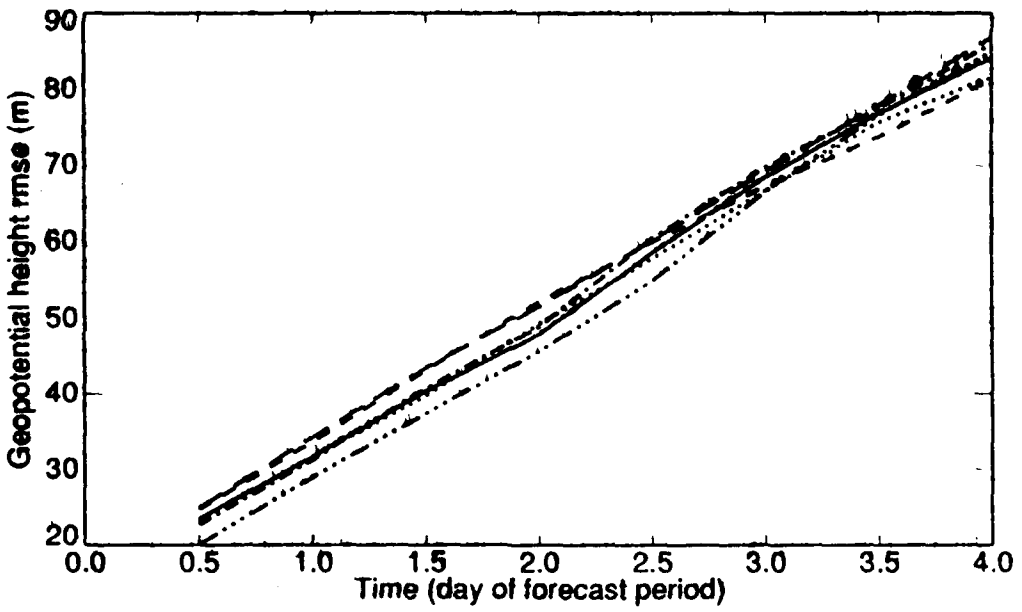

Figure 3.21. Rms forecast error growth for the Northern hemisphere extratropics 500 hPa height for the URSAT (solid), STATSAT (dash), NOSAT (dot), SSMSAT (dash-dot) and WINDSAT (dash-dot-dot-dot) OSSEs.

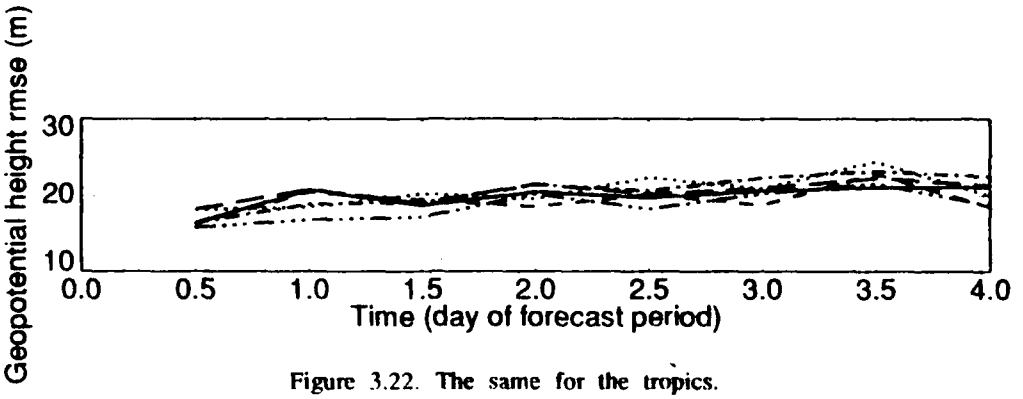

Figure 3.22. The same for the tropics.

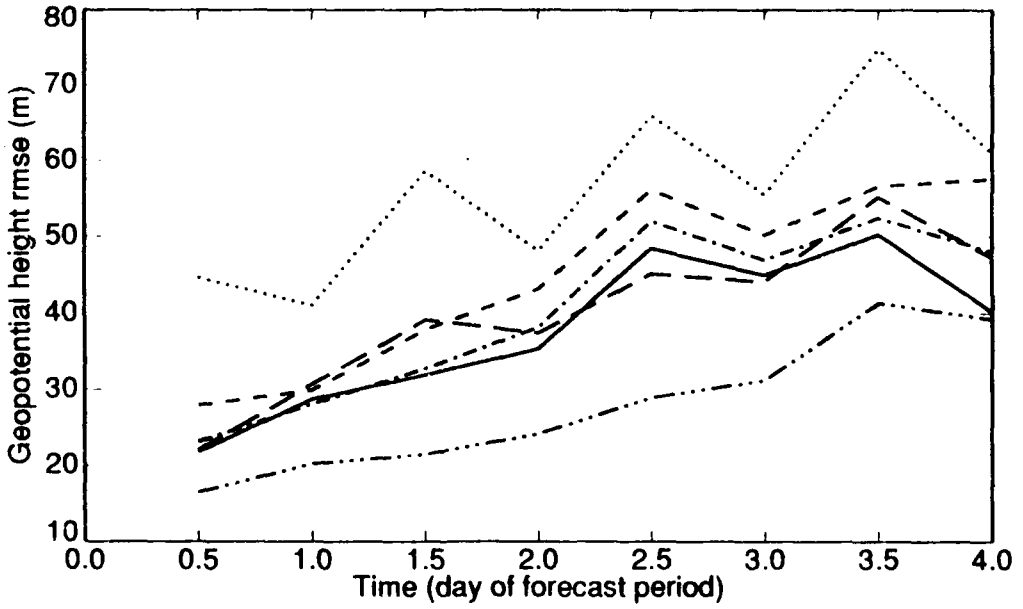

Figure 3.23. The same for the Southern Hemisphere extratropics.

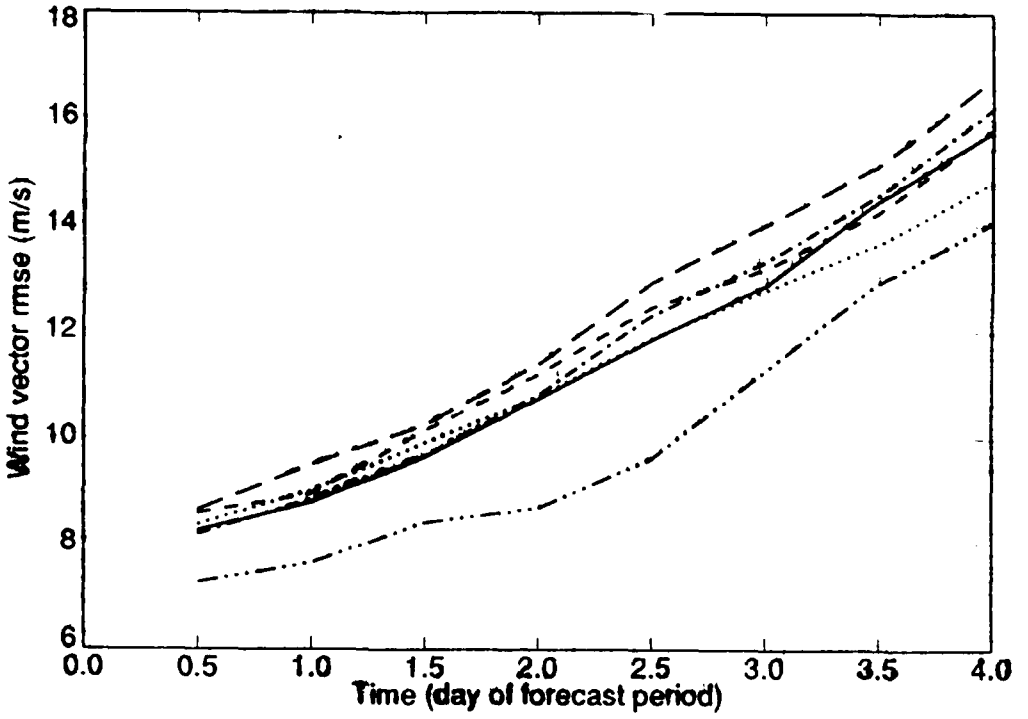

Figure 3.24. Rms forecast error growth for the Northern hemisphere extratropics 200 hPa vector wind for the URSAT (solid), STATSAT (dash), NOSAT (dot), SSMSAT (dash-dot) and WINDSAT (dash-dot-dot-dot) OSSEs.

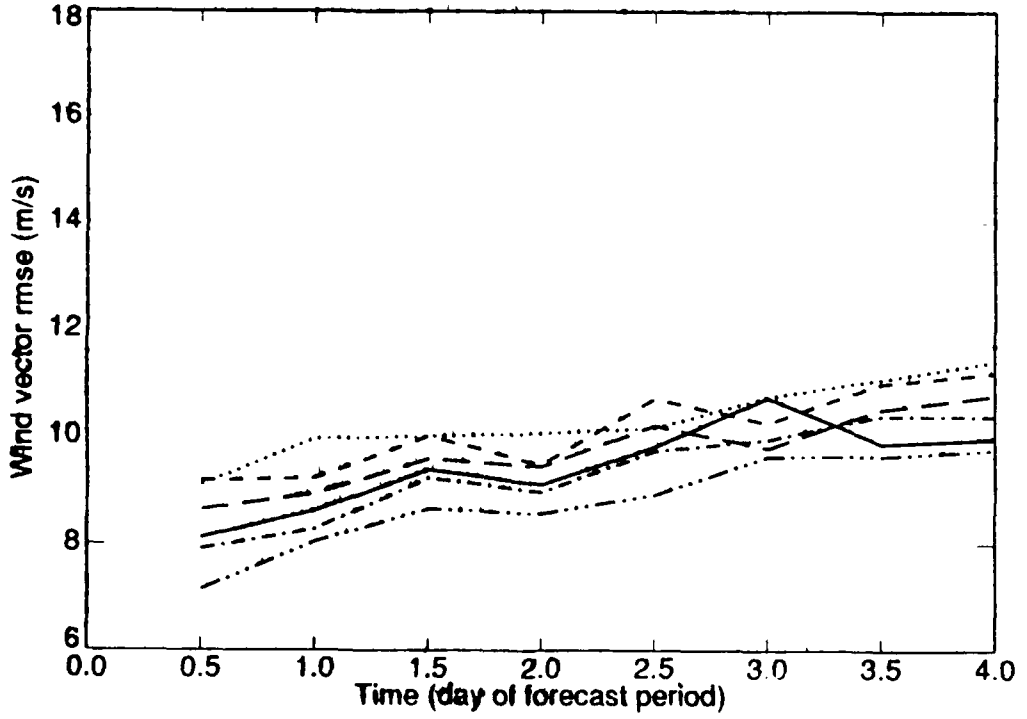

Figure 3.25. The same for the tropics.

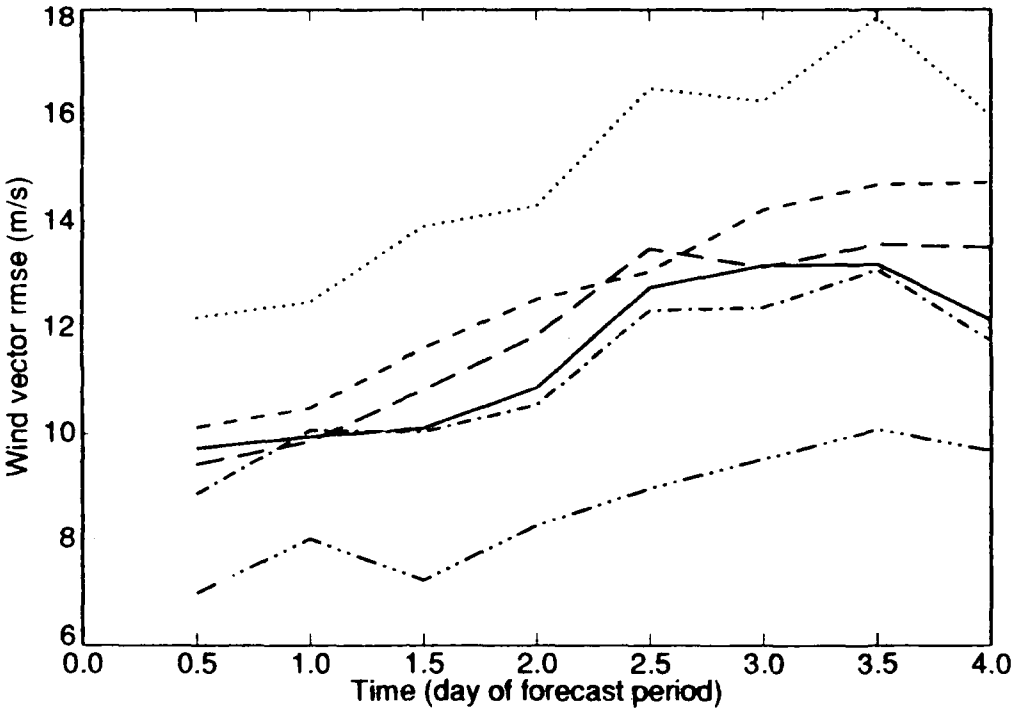

Figure 3.26. The same for the Southern Hemisphere extratropics.

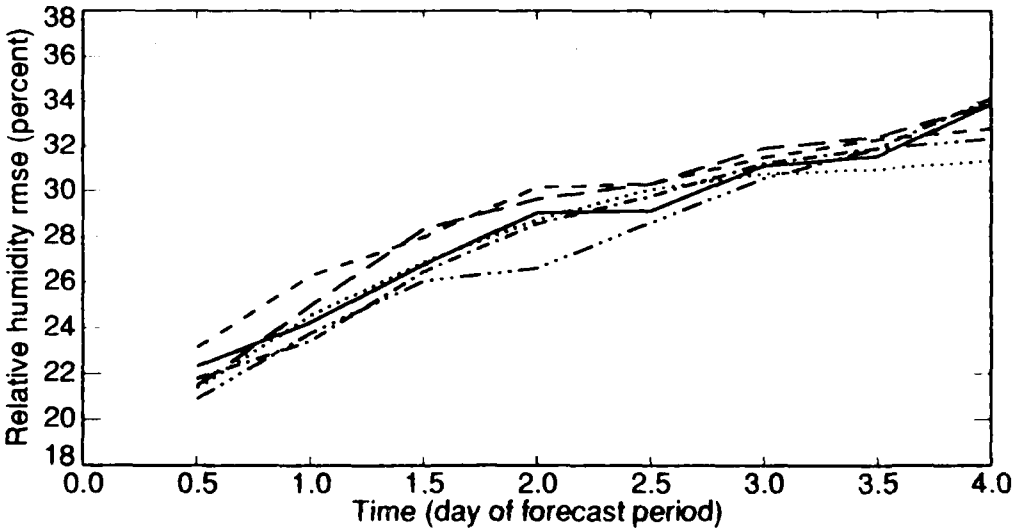

Figure 3.27. Rms forecast error growth for the Northern hemisphere extratropics 850 hPa relative humidity for the URSAT (solid), STATSAT (dash), NOSAT (dot), SSMSAT (dash-dot) and WINDSAT (dash-dot-dot-dot) OSSEs.

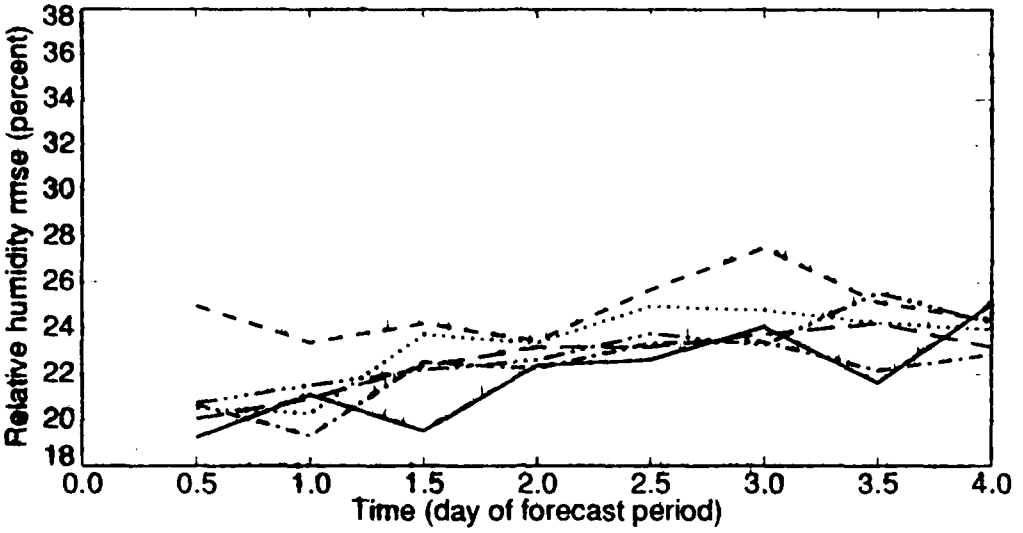

Figure 3.28. The same for the tropics.

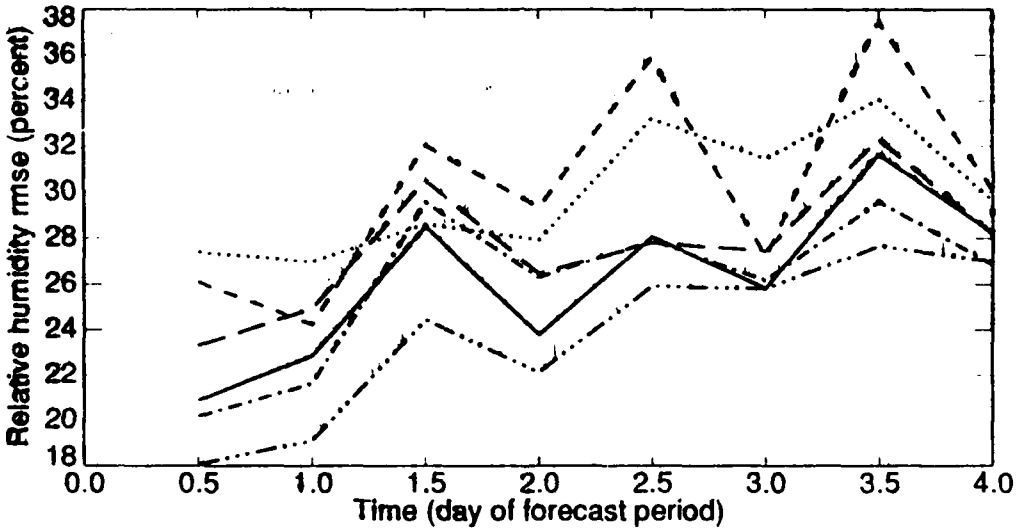

Figure 3.29. The same for the Southern Hemisphere extratropics.

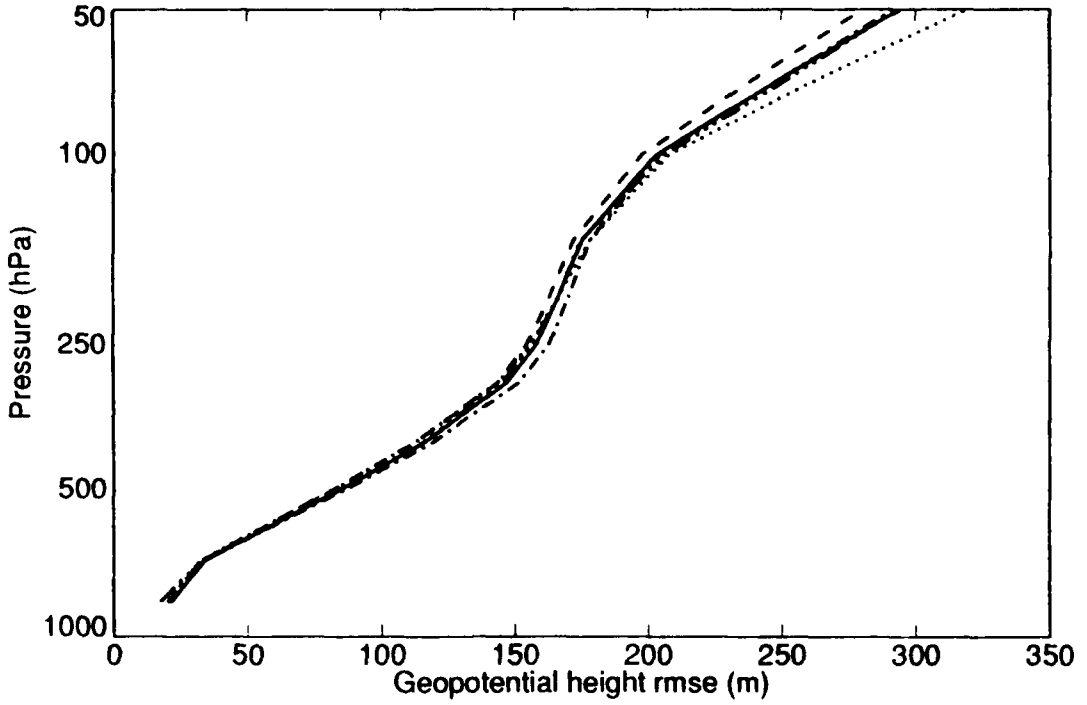

Figure 3.30. Rms height forecast errors as a function of pressure for the Northern Hemisphere for the URSAT (solid), STATSAT (dash), NOSAT (dot), SSMSAT (dash-dot) and WINDSAT (dash-dot-dot-dot) OSSEs.

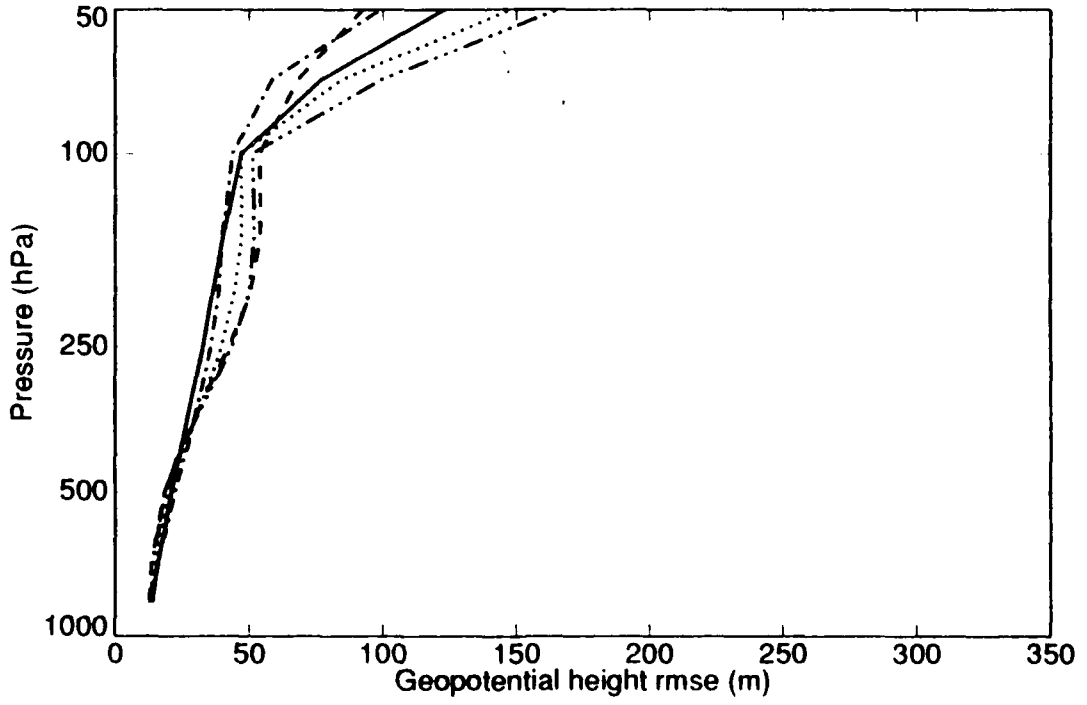

Figure 3.31. The same for the tropics.

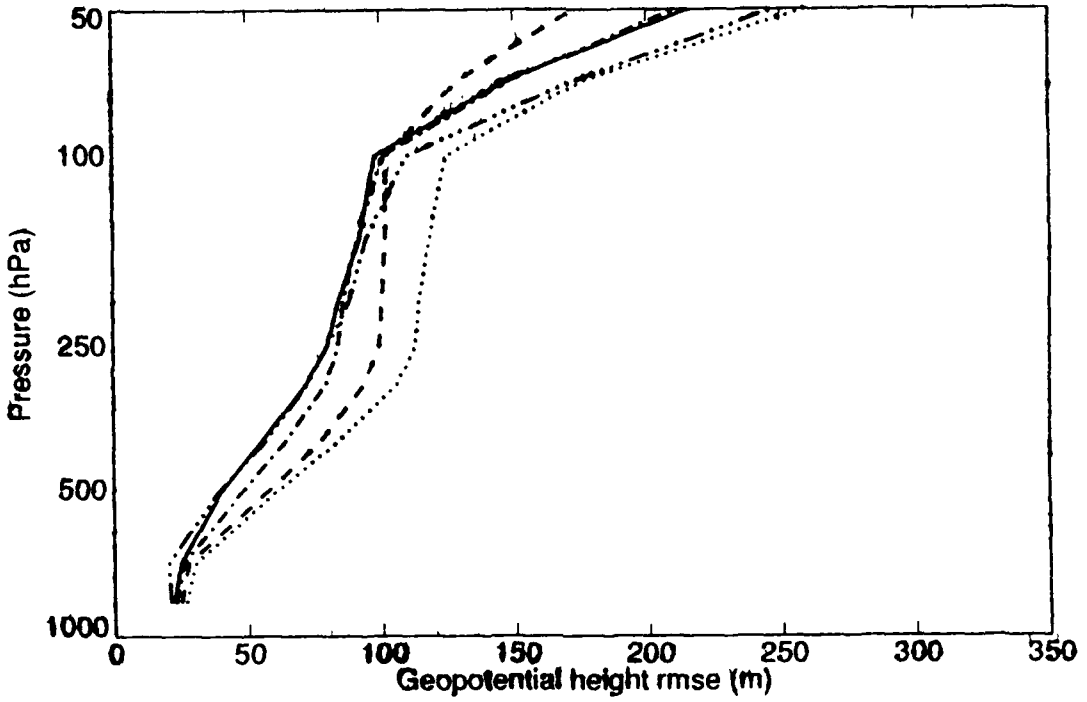

Figure 3.32. The same for the Southern Hemisphere.

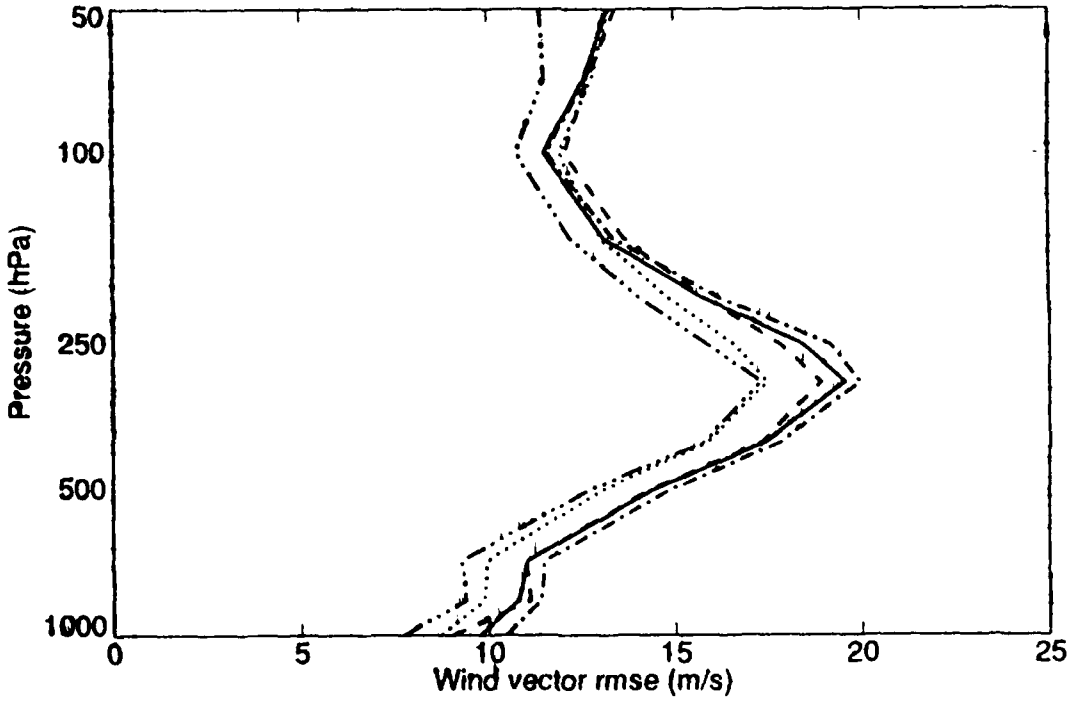

Figure 3.33. Rms wind vector forecast errors as a function of pressure for the Northern Hemisphere for the URSAT (solid), STATSAT (dash), NOSAT (dot), SSMSAT (dash-dot) and WINDSAT (dash-dot-dot-dot) OSSEs.

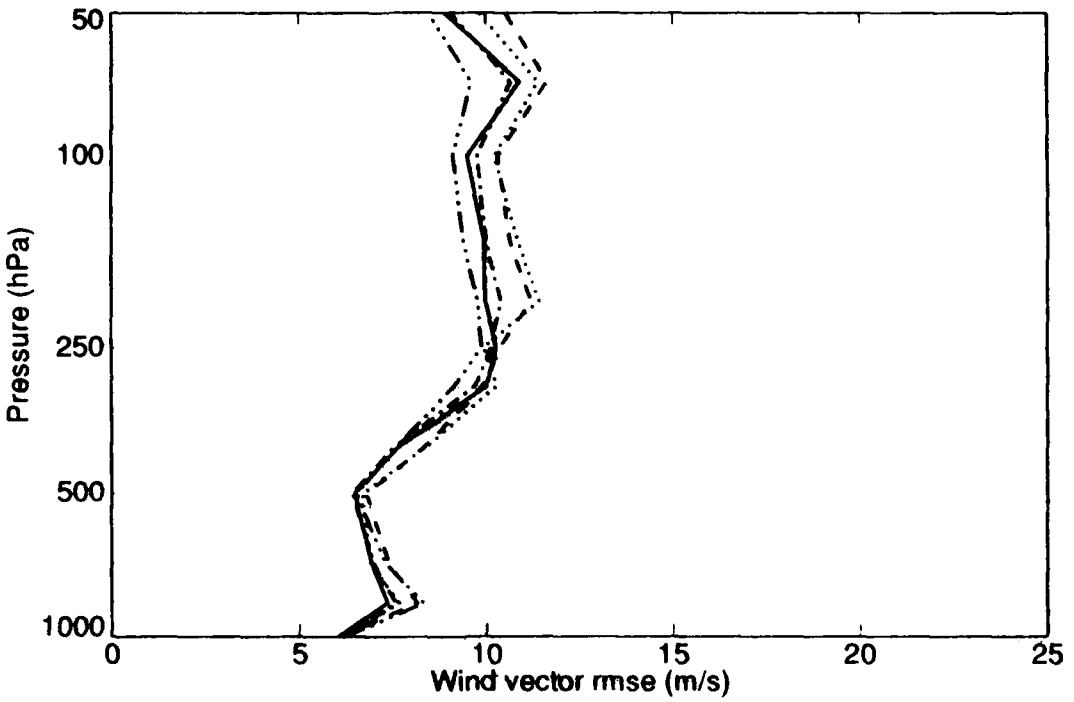

Figure 3.34. The same for the tropics.

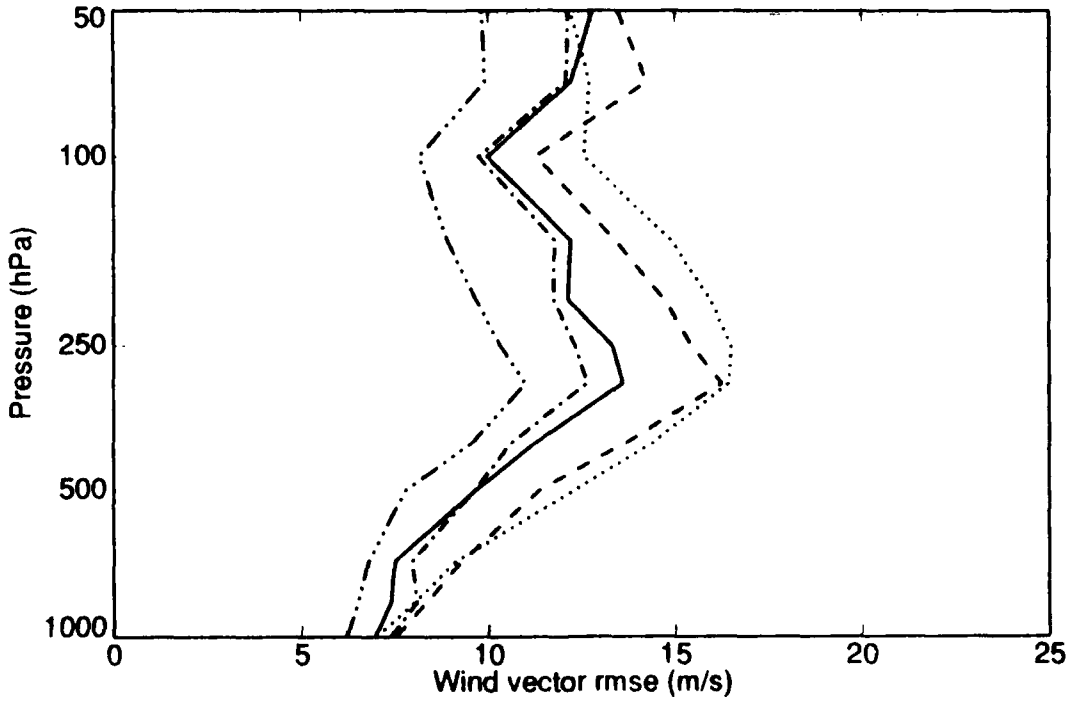

Figure 3.35. The same for the Southern Hemisphere.

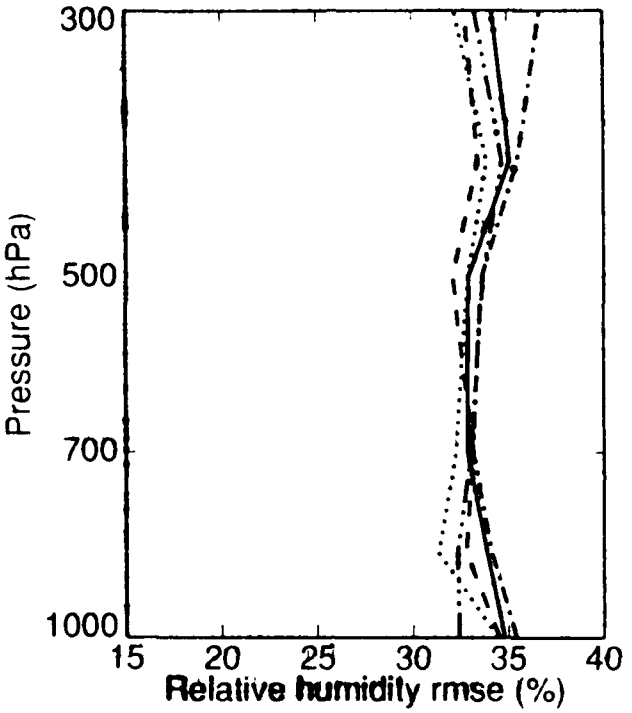

Figure 3.36. Rms relative humidity forecast errors as a function of pressure for the Northern Hemisphere for the URSAT (solid), STATSAT (dash), NOSAT (dot), SSMSAT (dash-dot) and WINDSAT (dash-dot-dot-dot) OSSEs.

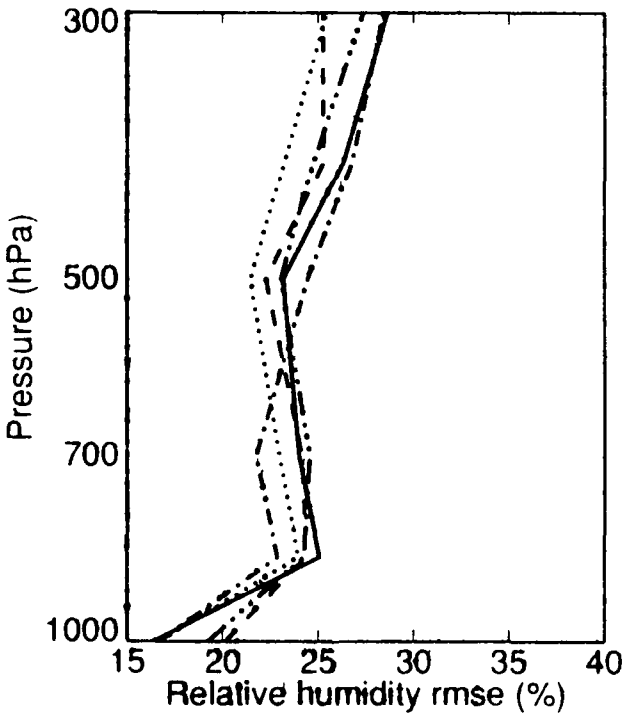

Figure 3.37. The same for the tropics.

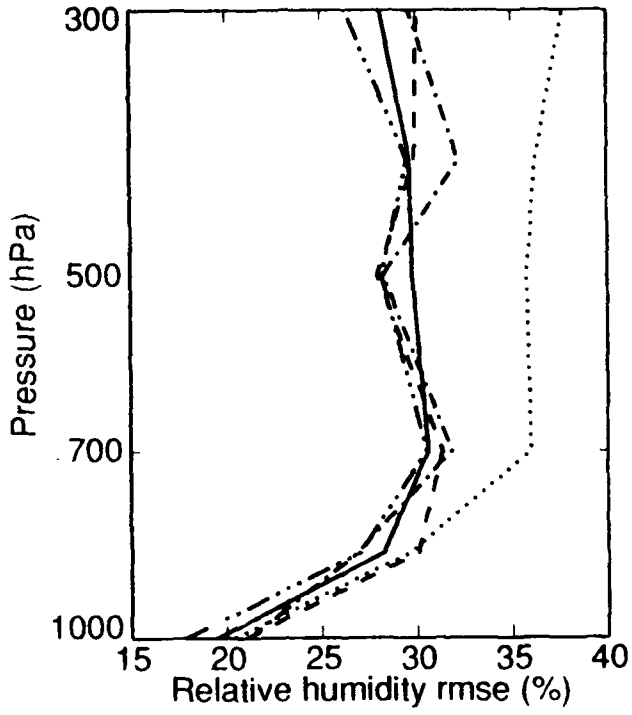

Figure 3.38. The same for the Southern Hemisphere.

4. Conclusions

Operational DMSP meteorological retrievals in support of numerical weather prediction (NWP) and other users does not exploit the multispectral information content of the various payload sensors in a complete manner. The unified retrieval (UR) methodology is a synergistic approach which combines the strengths of the DMSP sensors. For example, cloud information needed in support of SSM/T-2 water vapor profile retrievals is obtained from the OLS imager (coverage) and microwave imager (liquid water content) data, while the temperature profile information available from the SSM/T is used to refine determination of cloud top from the OLS infrared data. This report describes the methodology of the UR and it application to an observing system simulation experiment (OSSE).

Unified retrieval simulations were conducted based on ensembles of nature run profiles. Two sets of retrievals were performed: (a) a preliminary set which were assimilated and tested in the OSSE (the OSSE retrievals) and (b) an updated set which are described in section 2.3 above. The latter set was generated when a number of retrieval software errors which significantly degraded the quality of the retrievals were discovered subsequent to the OSSE. These were corrected and the software appropriately modified.

The updated unified retrievals show consistent but modest improvements over the first guess statistical retrievals for low level temperatures and integrated water vapor in the lowest retrieved layers. In the upper troposphere and in the tropopause region the unified retrieval errors for temperature are larger than those of the statistical retrieval. Since the NWP data assimilation system uses relative humidity, these results were converted to relative humidity. The relative humidity results are mixed; however, certain categories investigated show improvement. For example, in the tropics, the unified retrievals of RH show improvement relative to the statistical retrievals at 300 and 400 mb, and at all levels except the surface in cloudy situations.

Due to time constraints it was not possible to rerun the OSSE with the updated retrievals. The preliminary UR results were run through the assimilation and forecast system, however, and did not show an improvement in the model variables examined (height, relative humidity, and wind). For some levels, in fact, the first guess statistical retrievals are superior. Consequently, the preliminary UR data produce neutral or small negative impacts. The updated retrievals are somewhat more encouraging than the OSSE retrievals. Based on the results of the updated retrievals, we might anticipate positive impacts relative to the statistical retrieval approach (SSMSAT) for RH analyses at mid and upper levels in the tropics and possible modest improvements on lower level height analyses at high latitudes.

While the retrieval approach has been implemented here as a stand alone system, its most important application may be to provide data for use in a numerical weather prediction model. In this context it is noted that modifications to the procedure outlined are desirable. Operationally, for example, it may be advantageous to obtain some first guess elements such as the temperature and moisture profiles from model predicted fields. The quantities retrieved might be the model variables at the model vertical levels. This type of retrieval might be termed a variational analysis of the radiance observations. Furthermore, in the context of a prediction model application, forecast error covariances may be used as constraints on the

adjustment process (J. Eyre, personal communication). These changes are not inconsistent with the retrieval described and should in fact improve its effectiveness. Furthermore, the method provides estimates of the accuracy of each retrieval.

Quantitative interpretation of OSSE results require the most realistic experimental methodology possible. Although the current experiments are state-of-the-art, a number of improvements would be desireable, including correlated and therefore more realistic observing errors, more realistic forecast errors, enhancements to the analysis procedures and higher resolution in the analysis and nature run.

Appendix A Simulation of clouds from nature run data

A.1 Introduction

To perform the SSM/T OSSEs, simulated cloud data are needed for the forward problem, the retrieval algorithm and the in-line simulation of the SSM/T radiances. Preliminary computations, simply using the reverse Tibaldi scheme at mandatory levels, indicated a severe mismatch of the nature run data and the Tibaldi scheme: simulated total cloud cover was on the order of 80% when globally averaged. Thus, a relationship between archived nature run data (namely, u, v, T, and r, where r is relative humidity) and simulated clouds was developed and tuned to yield climatologically reasonable values. The data base used for this development is described in more detail in the following paragraphs. The diagnostic scheme consists of a convective and stratiform cloud module. The convection module uses the divergence field to diagnose convective cloud cover and cloud top; the stratiform module is a simple relative humidity to cloud cover conversion relationship. The two are combined to give convective and stratiform total cloud cover, and level cloud cover for each of the mandatory levels. The formulation and development of these procedures are discussed below.

We note that our purpose here is not to develop a new parameterization of cloudiness but to create a cloud cover consistent with the model nature run. In the ECMWF model convective cloud cover is not actually diagnosed. In the radiative parameterization, only stratiform cloud from the Geleyn scheme is used. However, there should be convective cloud when moist convection is taking place. Therefore our scheme includes both convective and stratiform cloud. Of course we use the Geleyn scheme for the stratiform cloud. The diagnosis of convective cloud is based on the vertical velocity diagnosed from the model, which is a key ingredient in the model parameterization of moist convection. (The other key ingredient is conditional instability - but this proved difficult to diagnose, even from the nature run, which is archived at mandatory levels only.) Since the model cloud climatology is not documented and for added realism, we tune our scheme to actual zonally averaged cloud climatology. As a result of this choice however, there is a mismatch between the diagnosed and observed clouds.

A.2 Data base

An independent reference of what are reasonable cloud cover values at different levels is needed for the tuning of a diagnostic cloud cover scheme. There are several possible cloud climatologies one might consider for this purpose ([20] contains a comprehensive list), but for our purposes it seems most appropriate to use a 3DNEPH-based climatology, since we are simulating OLS cloud imagery. The one chosen here are the monthly mean climatologies of 3DNEPH total cloud cover for 1979 of Hughes and Henderson-Sellers [21], which are given in map form (for layer cloud amount) and as zonal averages as a function of latitude (for total cloud cover); the latter is more amenable for quantitative optimization applications, and it provides enough detail to allow a reasonable tuning of the parameters of our diagnostic cloud scheme.

In the development and tuning described here, we compared the monthly mean values for November of 1979 with the average over 8 time periods of the nature run: 00 GMT and 12 GMT on November 10, 11, 18, and 19. The nature data available for tuning consisted of the archived values of u, v, T and r on mandatory pressure levels, interpolated from the original 1.875° grid to the 2.5°×2.5° grid. Terrain data, which were needed for the computation of surface pressure, were obtained by evaluating the spectral coefficients of the terrain used in the OSSE GSM forecasts on the 2.5°×2.5° grid.

A.3 Development and tuning of the cloud cover scheme

The development and tuning proceeded in three stages: first, the stratiform cloud cover scheme was applied to the nature data, and the results compared to the observed climatology. The results indicated the need for a partitioning of the observed data into convective and stratiform components, and the tuning was performed on the stratiform component alone. Next, the convective scheme was developed, using the convective component of the observed climatology for guidance. Finally, the two components were integrated, and total cloud cover values were then compared to the observed total cloud cover climatology for verification purposes. These three stages are now described in turn.

A.3.1 Stratiform cloud cover scheme tuning

The stratiform cloud cover scheme was based on the formulation of Geleyn [16]. This choice was suggested by the fact that the model used in producing the nature run, the ECMWF grid point model, used this scheme in its radiative package. The scheme relates cloud cover (c_k) to the relative humidity (r_k) expressed as a fraction between 0 and 1 at level k through the following relationship

$$c_k = \begin{cases} 0 & r_k < r_c \\ \left((r_k - r_c)/(1 - r_c)\right)^2 & r_k > r_c \end{cases} \qquad \text{(A.1)}$$

where r_c is a critical relative humidity. In Geleyn's original formulation, r_c was given by the formula

$$r_c = 1 - a\sigma(1-\sigma)(1 + b(\sigma - 1/2)) \qquad \text{(A.2)}$$

where $\sigma = p/p_s$, p is pressure, p_s is surface pressure and a and b are tunable parameters. In our tuning, we did not constrain r_c to the form given above, but instead regarded the values of r_c at six σ levels as the adjustable parameters. The σ levels (1.00, 0.85, 0.70, 0.50, 0.40, 0.30) are located at the moisture-carrying mandatory levels for a surface pressure of 1000 mb. We applied the formula to the mandatory level data by interpolating the relative humidity data to the σ levels. For this purpose, surface pressure was computed from the mandatory level height and temperature data using the NMC routine GETPS. The r_c profile given by (A.2) with $a = 2$ and $b = \sqrt{3}$ evaluated at the σ levels, is shown in Figure A.1. The resulting cloud cover values at the levels were then combined, using random overlap, to yield a total cloud cover:

$$c_t = 1 - \prod(1 - c_k) \qquad \text{(A.3)}$$

Zonal averages were then formed, and compared to the corresponding climatological values. First and second derivatives of the zonal mean total cloud cover with respect to the r_c values were computed, as well, to allow optimization of the parameter values. The optimization procedure closely follows what was used by Louis et al. [32]. Basically we use a Newton-Raphson iteration to minimize the nonlinear cost function $S = \sum_j (c^j - \hat{c}^j)^2$ where $\hat{c}^j$ is the climatological value of zonal mean total cloud cover for latitude band j, and c^j is the corresponding computed value. The sum is taken over the 36 latitude bands of 5° width for which climatology is defined.

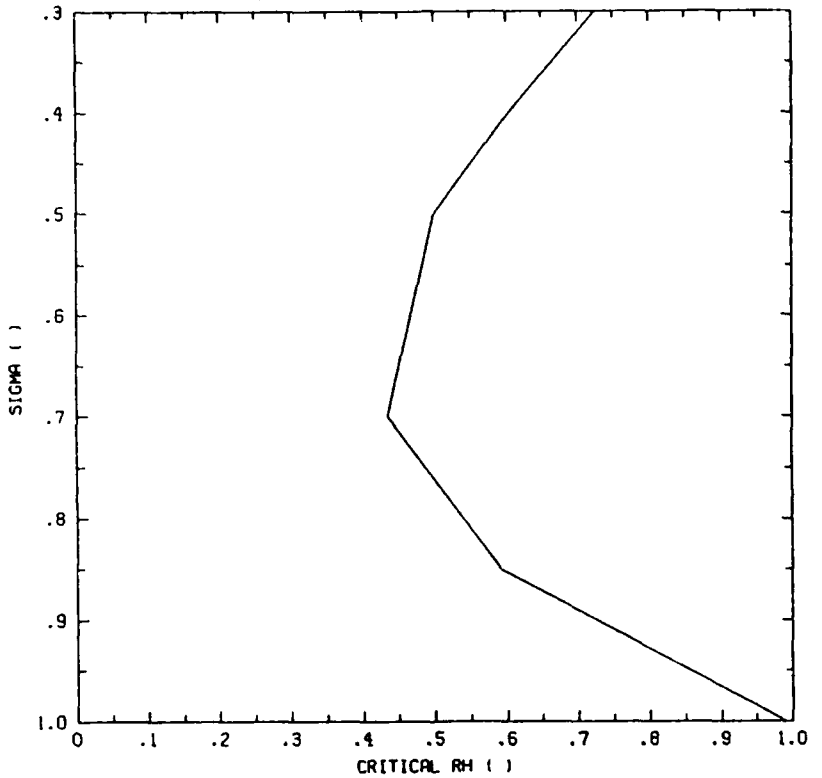

Figure A.1. Critical relative humidity profile r_c given by (A.2) with $a = 2$ and $b = \sqrt{3}$.

Application of (A.1) to the nature data, using r_c given by (A.2) as a first guess, resulted in the cloud cover shown in Figure A.2; the corresponding climatological values are shown in the figure as well. It is obvious that the tropical cloud cover is grossly underestimated, whereas values are more realistic at higher latitudes. The rms error of zonally averaged cloud cover is 21% in Figure A.2. Attempts at optimizing (A.1) by adjusting r_c were unsuccessful, indicating a more fundamental problem with this approach: the climatological values contain clouds of convective as well as of stratiform origin, whereas the relationship (A.1) is only applicable to stratiform clouds.

In an attempt to arrive at a preliminary tuning of just the stratiform cloud cover relationship, the total climatological cloud cover was partitioned into a stratiform and convective component, the latter being parameterized as

$$c_c = c_t \eta_c \qquad \text{(A.4)}$$

where c_c and c_t are the convective and total climatological cloud cover, respectively, and η_c is a function of latitude given by

$$\eta_c \quad a_c \exp\left(\quad \left((\phi \quad \phi_0)^2 / \sigma_c \right) \right) \tag{A.5}$$

where ϕ is the latitude, a_c and σ_c are adjustable parameters; ϕ_0 was chosen as 0°. For large enough first guess values of a_c and σ_c, optimization of (A.1) in conjunction with (A.4) proved successful. Of course, one aspect of this formulation is the opportunity of the optimization procedure to reduce the errors of stratiform cloud cover to zero by increasing c_c to the point where it equals c_t. To avoid convergence to this trivial solution, a_c and σ_c were held fixed in the final optimization of the r_c profile. For values of a_c = .75 and σ_c = 45° the cloud components are shown in Figure A.3 and the optimal r_c profile obtained by the optimization procedure is shown in Figure A.4. The corresponding stratiform cloud cover (Figure A.5) differs from the climatological stratiform cloud cover (Figure A.3) by an rms value of 8.8%. Given the disparity of the data sources, and the simplicity of the cloud cover relationship, agreement to this order must be considered adequate.

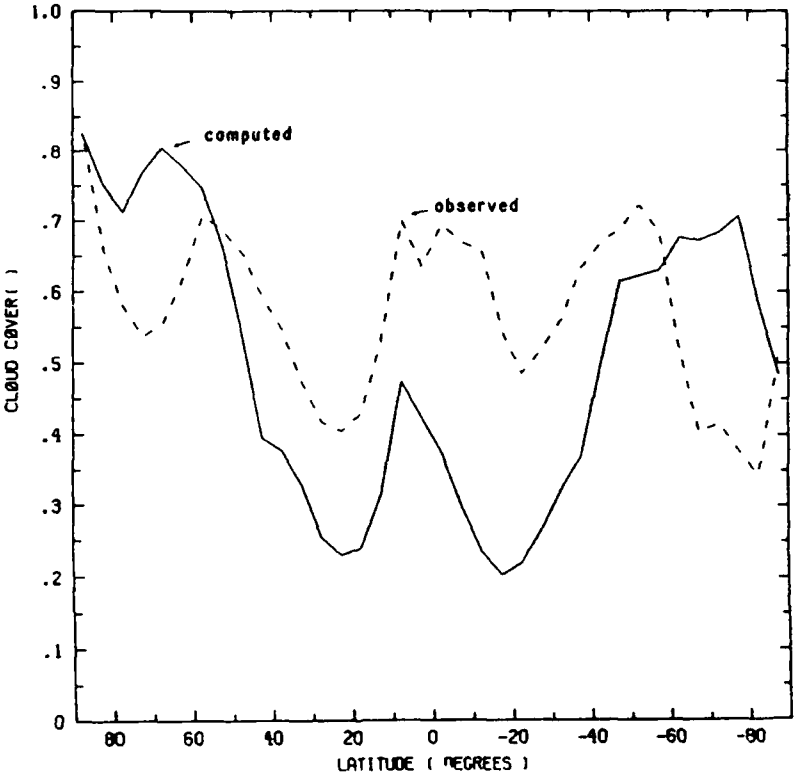

Figure A.2. Zonal mean total cloud cover computed from (A.1), (A.2), and (A.3). Also shown is the observed climatology.

A.3.2 Convection scheme development and tuning

The diagnosis of convective activity from the archived nature run data is less straightforward than the corresponding calculations for stratiform cloud cover. One might consider

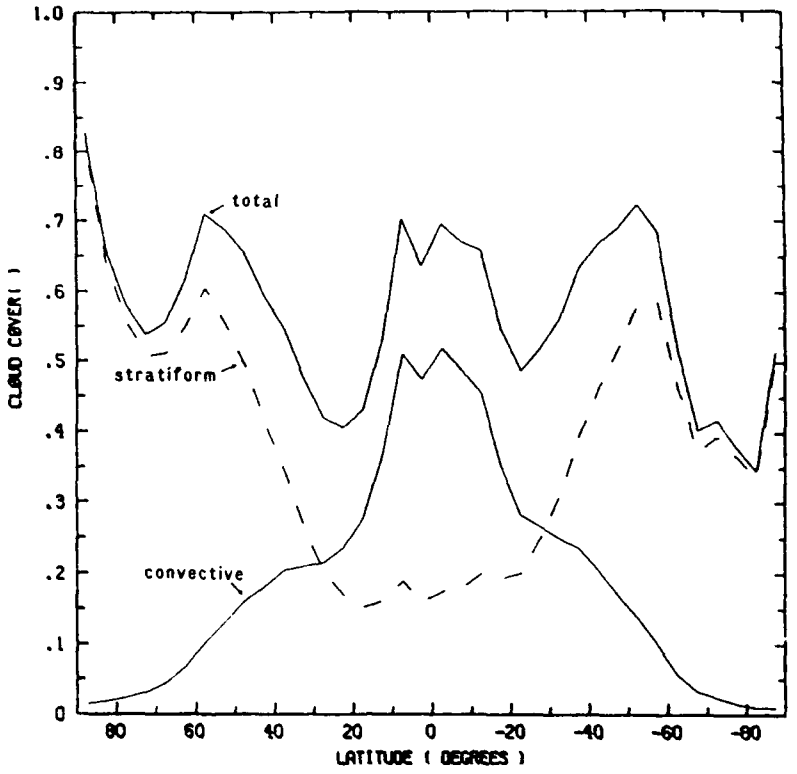

Figure A.3. Climatological values of zonal mean cloud cover: total, convective, and stratiform, computed from (A.4) with a_c = .75 and σ_c = 45°.

computing the conditional stability of the atmosphere; however, given the fact that most of the tropical atmosphere is near conditions of neutral stability, and that only mandatory level data are available, this approach is not likely to be successful. Instead, the divergent wind field was used in the diagnosis of convection. Julian [29] used a relation between convection and the divergent wind in the reverse application of inferring the divergent component of the wind field from the observed convective activity. He related the satellite observed Equivalent Black Body Temperature (EBBT) to define categories of convection, each of which was associated with a characteristic divergence profile. The divergence profiles (his Table B1) all exhibited convergence (divergence) below (above) 400 mb - 500 mb for EBBT of 245 K and below. With decreasing EBBT, the level of maximum divergence rises from 250 mb to 150 mb (the top level for which the divergence profiles are defined), whereas there is no monotonic increase in the intensity of either the upper level divergence or the low-level convergence. The EBBT categories are thus not directly suitable for parameterizing convective cloud cover. Danard [10] used a linear relationship between convective cloud cover and precipitation intensity, based on the work of Richards and Arkin [38] with GATE data. We adopted a similar approach by relating a measure of midlevel vertical velocity, which is also related to precipitation rate, to convective cloud cover. The vertical profile of divergence was used to yield a measure of the midlevel vertical p-velocity ω as follows:

$$S_d \quad \sum (w_k D_k) / \sum w_k \tag{A.6}$$

The sum S_d is simply a weighted sum of the mandatory level divergence values D_k, with the weights w_k chosen such that they correspond to an upward (downward) integration of the

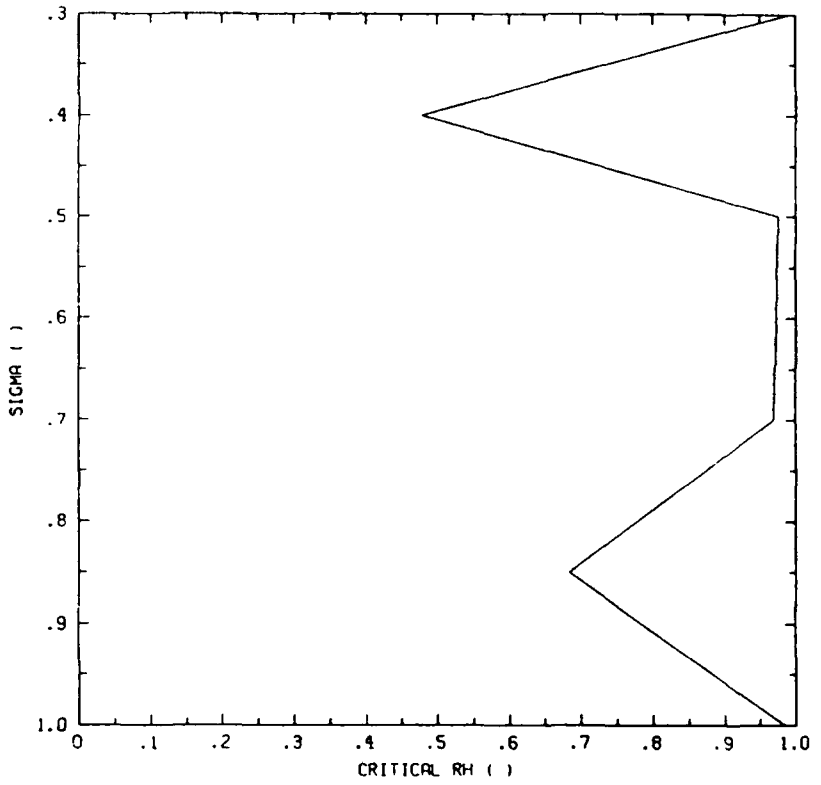

Figure A.4. Optimized profile of critical relative humidity, r_c, for a_c = .75 and σ_c = 45°.

continuity equation from the first level above the surface (the 150 mb level), assuming zero ω at the top and bottom. The sign convention is that $S_d > 0$ for upward vertical velocity at 500 mb. Convective cloud cover was then calculated by multiplying this sum by a factor of proportionality, η'_c:

$$c_c \quad \begin{cases} 0 & S_d < 0 \\ \eta'_c S_d & S_d > 0 \end{cases} \tag{A.7}$$

In cases where (A.7) yields $c_c > 1$, c_c is set to 1.

Figure A.6 shows the convective cloud cover computed with a constant factor of η'_c; it is apparent from the large values at middle and high latitudes that the measure of 500 mb ω includes synoptic scale uplift as well as tropical convection. Thus, the factor η'_c is modeled to take the latitude-dependence of convection into account explicitly:

$$\eta_c \quad a'_c \exp\left(\quad \left((\phi \quad \phi_0)^2 / \sigma'^2_c \right) \right) \tag{A.8}$$

where the a'_c and σ'_c are adjustable parameters. In a crude way, this takes into account the more favorable conditions for convection in the tropics. Optimization of (A.7) and (A.8) were performed, using the convective climatology modeled by (A.4) as truth. The resulting convective cloud cover distribution is shown in Figure A.7, which corresponds to values of a'_c = 2.27E6 sec and σ'_c = 28.9. This differs from the "truth" shown in Figure A.3 by an rms value of 6.3%.

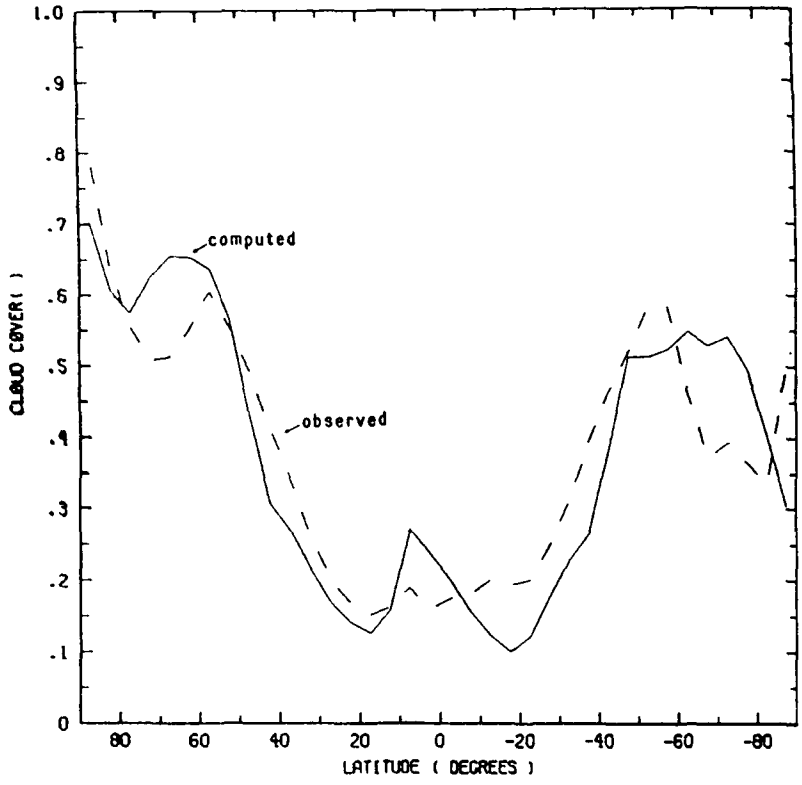

Figure A.5. Computed stratiform cloud cover for the profile of critical relative humidity shown in Figure A.4. The climatological values from Figure A.3 are shown for comparison.

Although the fit is good as measured by the rms statistic, the shapes of these two curves are significantly different. Relative to the "truth", there are relatively large amounts of convective cloud in the subtropical subsidence zone and relatively small amounts in the tropical convergence zone. It may be that the distribution of convection in the model differs significantly from that in the actual atmosphere.

A.3.3 Combination of stratiform and convective schemes

The final step in the development of our cloud diagnostic scheme is the combination of the convective and stratiform components. A schematic depiction of the combined scheme is shown in Figure A.8: convective clouds occupy a fraction c_c of the grid box between cloud base (assumed to be the lowest mandatory level above the surface) and the convective cloud top, p_c, where c_c is determined from (A.7) and (A.8). The convective cloud top p_c is determined as the level of maximum divergence between 500 mb and 150 mb. The stratiform cloud cover formulation (A.1) is applied to all mandatory levels between the surface and 300 mb; the r_i are interpolated to the σ values at the mandatory levels from the standard σ levels. In the absence of convective clouds (for practical applications, this is defined by $c_c < 1\%$), the total cloud cover is then obtained from the level values from (A.3). In the case of convection, the stratiform clouds can only occupy $(1 - c_c)$ of the grid box below p_c. Total stratiform cloud cover of that portion of the grid box below p_c, c_s, is thus computed by applying (A.1) and (A.3) to the levels below

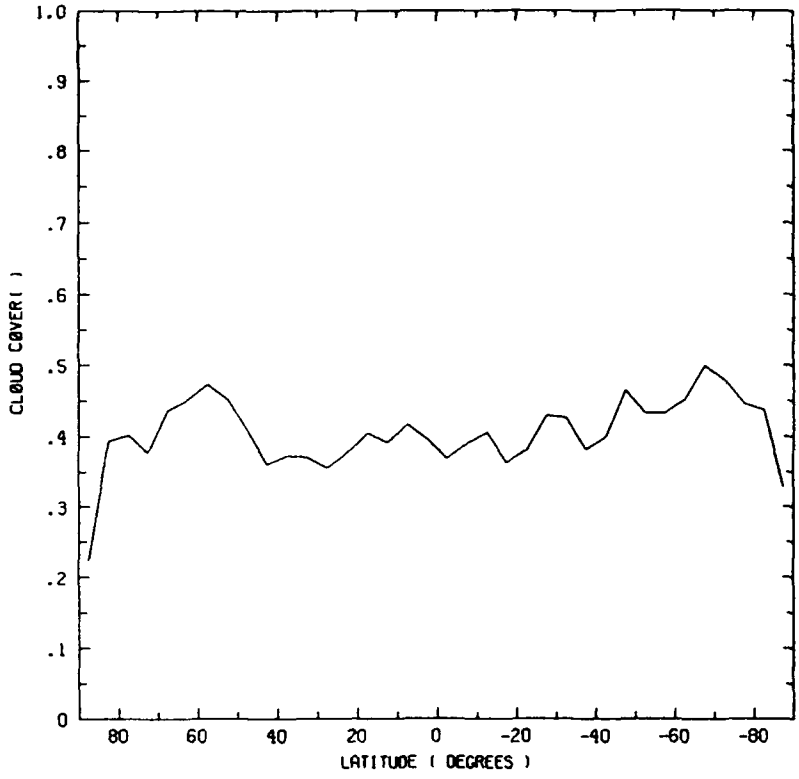

Figure A.6. Computed convective cloud cover for a constant η'_c = 3.E6 sec.

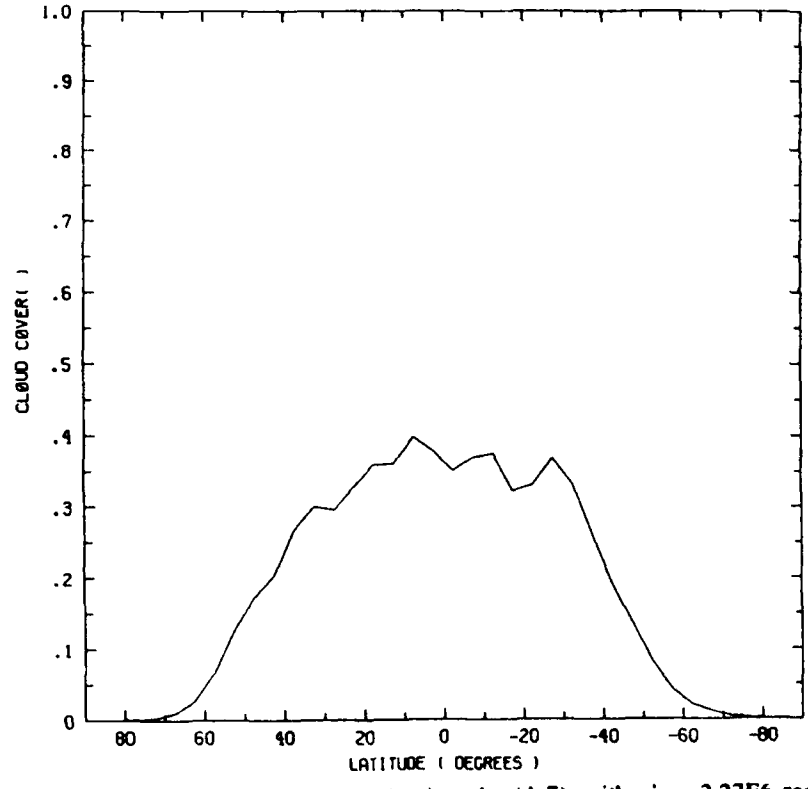

Figure A.7. Computed convective cloud cover η'_c given by (A.7), with a'_c = 2.27E6 sec and σ'_c = 28.9.

p_c. The total (convective and stratiform) cloud cover cover below p_c is then given as

$$c'_t \quad c_c + (1 \quad c_c)\, c_s \tag{A.9}$$

Finally, c_t is obtained by overlapping any stratiform clouds at levels above p_c over c'_t, using a random overlap formulation as in (A.3).

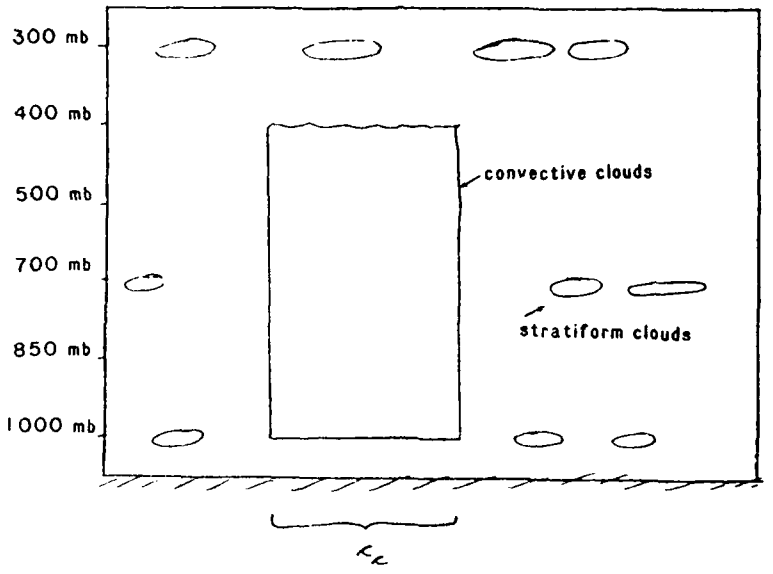

Figure A.8. Schematic depiction of combined cloud diagnostic scheme. See text for details.

This scheme has several tunable parameters: the convective scheme depends on the factor of proportionality η'_c, which is determined by the amplitude a'_c and half-width σ'_c. The stratiform scheme depends on the values of r_c, defined at the six σ levels 1.00, .85, .70, .50, .40, .30. In our tuning of these parameters, we did not attempt to simultaneously tune the convective and stratiform components, but instead relied on the previous separate optimizations of the individual components.

The convective tuning yielded values of the amplitide a'_c = 2.27E6 sec, and half-width σ'_c = 28.9. Since the resulting convective cloud cover differed somewhat from the assumed convective climatology shown in Figure A.3, we repeated the tuning of the stratiform relationship by simply subtracting the convective cloud cover from the climatological total cloud cover, to arrive at an approximate value of observed stratiform cloud cover. The optimization converged to the r_c profile shown in Figure A.9, which resulted in an rms difference from the approximate stratiform climatological values of 8.4%, compared to 9.1% for the r_c shown in Figure A.4. The values of r_c at the six σ levels shown in Figure A.9 are 95.2%, 56.9%, 99%, 99%, 64.3%, 98.5%. Application of these values for a'_c, σ'_c, and r_c to the combined cloud cover scheme resulted in the total cloud cover distribution shown in Figure A.10, which differs from the observed climatology by 10.3%. The discrepancy is thus not much larger than what was to be expected from the approximate tuning of the stratiform scheme alone. For comparison, the use of the r_c shown in Figure A.4 resulted in an rms error of total cloud cover of 11.4%.

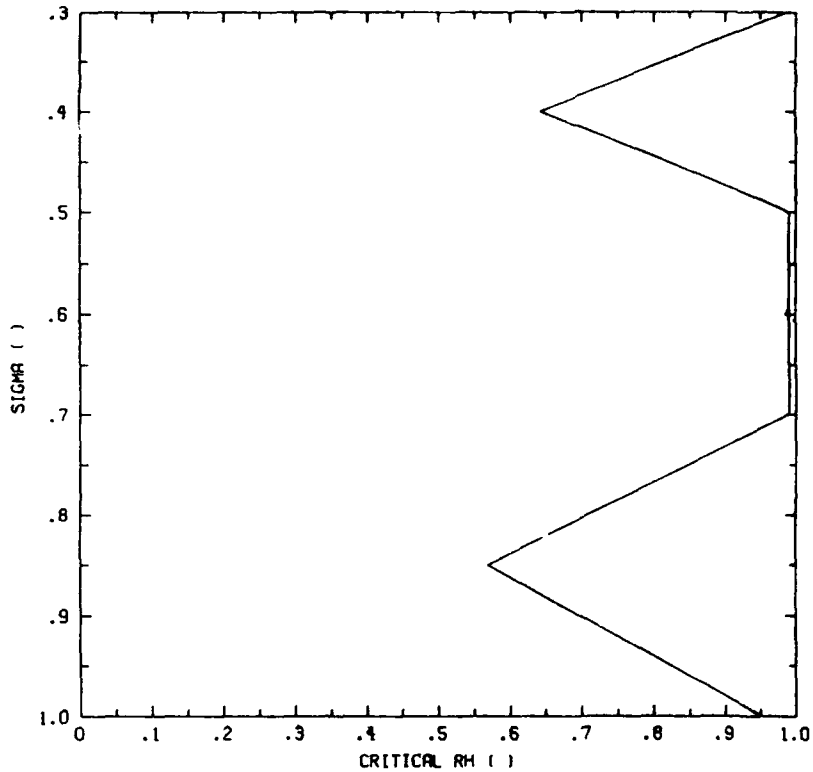

Figure A.9. Optimized profile of critical relative humidity, r_c, for the convective cloud cover shown in Figure A.7.

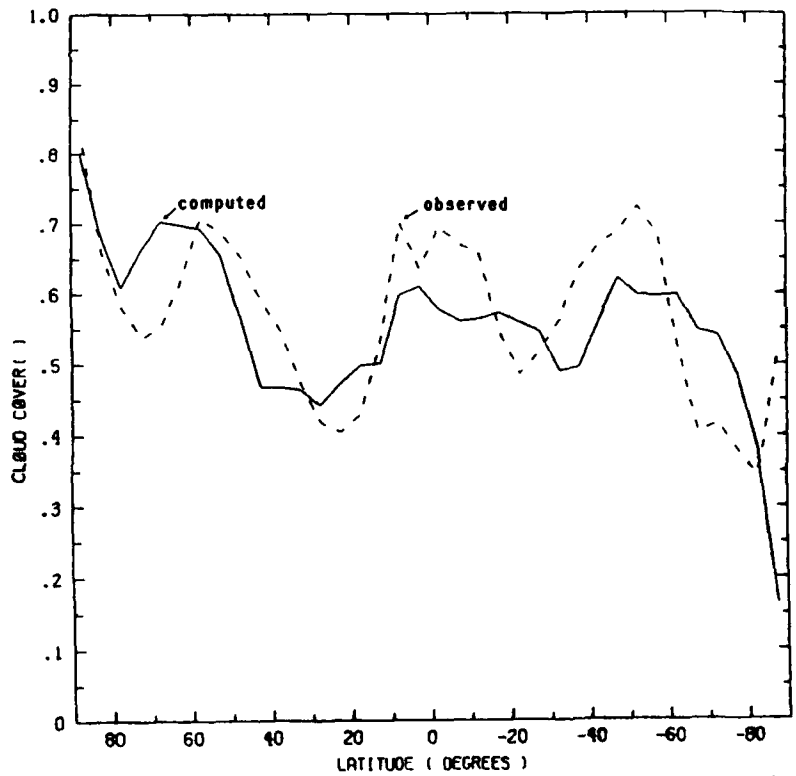

Figure A.10. Computed total cloud cover using the combined cloud scheme, with the convective parameters as in Figure A.7 and the r_c shown in Figure A.9. For comparison, the observed climatology is repeated from Figure A.3.

Bibliography

[1] C. P. Arnold, C. H. Dey, and W. J. Bostelman. Results of an observing system simulation experiment based on the proposed WINDSAT instrument. In W. E. Baker and R. J. Curran, editors, *Global Wind Measurements*. A. Deepak Publishing, Hampton, VA, 1985.

[2] R. Atlas, E. Kalnay, W. E. Baker, J. Susskind, D. Reuter, and M. Halem. Simulation studies of the impact of future observing systems on weather prediction. In *Preprint Volume, Seventh Conference on Numerical Weather Prediction*, pages 145–151, Montreal, June 17-20 1985. American Meteorological Society.

[3] B. Ballish. *Initialization, theory and application to the NMC spectral model*. PhD thesis, Dept. of Meteorology, University of Maryland, College Park, MD, 1980.

[4] W. H. Bennett. Passive microwave sounders for air temperature and water vapor profiling. In *Proceedings, NOAA Conference on Passive Microwave Observing from Environmental Satellites*, Technical Report NESDIS 35, pages 157–166. U. S. Department of Commerce, Washington, DC, 1987.

[5] K. H. Bergman. Multivariate analysis of temperature and winds using optimum interpolation. *Monthly Weather Review*, 107:1423–1444, 1979.

[6] S. Brenner, C.-H. Yang, and K. Mitchell. The AFGL global spectral model: Expanded resolution baseline version. Technical Report 84-0308, Air Force Geophysics Laboratory, Hanscom AFB, MA, 1984. [NTIS ADA160370].

[7] S. Brenner, C.-H. Yang, and S. Y. K. Yee. The AFGL spectral model of the moist global atmosphere: Documentation of the baseline version. Technical Report 82-0393, Air Force Geophysics Laboratory, Hanscom AFB, MA, 1982. [NTIS ADA129283].

[8] J. A. Coakley, Jr. and F. P. Bretherton. Cloud cover from high-resolution scanner data: Detecting and allowing for partially filled fields of view. *Journal of Geophysical Research*, 87(C7):4917–4932, 1982.

[9] R. J. Curran et al. LAWS instrument panel report. Technical report, NASA, Washington, DC, 1988.

[10] M. Danard. On the use of satellite estimates of precipitation in initial analyses for numerical weather prediction. *Atmos. Ocean*, 23:23–42, 1985.

[11] C. Dey, C. P. Arnold, and W. Bostelman. Design of a WINDSAT observing system simulation experiment. In W. E. Baker and R. J. Curran, editors, *Global Wind Measurements*, pages 73–79, Columbia, MD, 1985. A. Deepak Publishing, Hampton, VA.

[12] V. J. Falcone, L. W. Abreu, and E. P. Shettle. Atmospheric attenuation of millimeter and submillimeter waves: Models and computer code. Technical Report 79-0253, Air Force Geophysics Laboratory, 1979. [NTIS ADA084485].

[13] V. J. Falcone, L. W. Abreu, and E. P. Shettle. Atmospheric attenuation in the 30-300 GHz region using RADTRAN and MWTRAN. *Proc. Soc. Photo Opt. Instrum. Eng.*, 337:62–66, 1982.

[14] V. J. Falcone and R. G. Isaacs. The DMSP microwave suite (1987). In *Proceedings, NOAA Conference on Passive Microwave Observing from Environmental Satellites*, Technical Report NESDIS 35, pages 174–185. U. S. Department of Commerce, Washington, DC, 1987.

[15] N. E. Gaut, M. G. Fowler, R. G. Isaacs, D. T. Chang, and E. C. Reifenstein, III. Studies of microwave remote sensing of atmospheric parameters. Technical Report 75-0007, Air Force Cambridge Research Laboratory, 1975. [NTIS ADA008042].

[16] J.-F. Geleyn. Some diagnostics of the cloud-radiation interaction in ECMWF forecasting models. In *Workshop on Radiation and Cloud-Radiation Interaction in Numerical Modeling*, pages 135–161, Reading, U.K., 15-17 October 1980. ECMWF. [Publication date 1981].

[17] C. Grassotti, R. Isaacs, R. N. Hoffman, J.-F. Louis, T. Nehrkorn, and M. Mickelson. A study of the impact of simulated 183 GHz water vapor retrievals on numerical weather prediction. Technical Report 89-0093, Geophysics Laboratory, Hanscom AFB, MA, 1989. [NTIS ADA210431].

[18] R. N. Hoffman, C. Grassotti, R. G. Isaacs, J.-F. Louis, and T. Nehrkorn. Assessment of the impact of simulated satellite lidar wind and retrieved 183 GHz water vapor observations on a global data asssimilation system. *Monthly Weather Review*, 1990. Submitted.

[19] R. N. Hoffman, M. Mickelson, and T. Nehrkorn. Enhancements to the AFGL Statistical Analysis Program (ASAP) for the global multivariate analysis of heights and winds. Technical Report 87-0279, Air Force Geophysics Laboratory, Hanscom AFB, MA, 1988. [NTIS ADA202912].

[20] N. A. Hughes. Global cloud climatologies: A historical review. *Journal of Climate and Applied Meteorology*, 23:724–751, 1984.

[21] N. A. Hughes and A. Henderson-Sellers. Global 3-D nephanalysis of total cloud amount: Climatology for 1979. *Journal of Climate and Applied Meteorology*, 24:669–686, 1985.

[22] R. G. Isaacs. Retrieval techniques for atmospheric path characterization. In *Critical Review of Atmospheric Modeling Technology*, Proceedings of SPIE. SPIE, 1988.

[23] R. G. Isaacs. A unified retrieval methodology for the DMSP meteorological sensors. In A. Deepak, H. E. Fleming, and J. S. Theon, editors, *RSRM '87: Advances in Remote Sensing Retrieval Methods*, pages 203–214. A. Deepak Publishing, Hampton, VA, 1989.

[24] R. G. Isaacs and G. Deblonde. Millimeterwave moisture sounding: the effect of clouds. *Radio Science*, 22:367–377, 1987.

[25] R. G. Isaacs, R. N. Hoffman, and L. D. Kaplan. Satellite remote sensing of meteorological parameters for global numerical weather prediction. *Reviews of Geophysics*, 24:701–743, 1986.

[26] R. G. Isaacs, R. N. Hoffman, J.-F. Louis, and T. Nehrkorn. A study of the impact of 183 GHz water vapor retrievals. In *Preprints, Eighth Conference on Numerical Weather Prediction*, pages 285–289, Baltimore, Maryland, February 22-26 1988. American Meteorological Society.

[27] R. G. Isaacs, R. D. Worsham, and B. L. Lindner. Characterizing microwave propagation using the AFGL microwave attenuation/transmittance/brightness temperature code. Technical Report 89-0188, Air Force Geophysics Laboratory, Hanscom AFB, MA, 1989.

[28] Y.-Q. Jin and R. G. Isaacs. Simulation and statistical retrieval for inhomogeneous, nonisothermal atmospheric precipitation. *Journal of Quantitative Spectroscopy and Radiative Transfer*, 37:461–468, 1987.

[29] P. R. Julian. Objective analysis in the tropics: A proposed scheme. *Monthly Weather Review*, 112:1752–1767, 1984.

[30] R. B. Kiess and W. M. Cox. The AFGWC automated real-time cloud analysis model. Technical Note 88/001, AFGWC, 1988.

[31] R. C. Lo. A comprehensive description of the mission sensor microwave imager (SSM/I) environmental parameter extraction algorithm. Memorandum Report 5199, Naval Research Laboratory, 1983. [NTIS ADA134052].

[32] J.-F. Louis, R. N. Hoffman, W. J. Gutowski, L. D. Kaplan, W.-C. Wang, J. Susskind, and D. Reuter. Tuning of cloud parameterizations for radiative heating calculations in GCM using satellite IR sounding data. In *Preprint Volume, Seventh Conference on Numerical Weather Prediction*, pages 405–407, Montreal, June 17-20 1985. American Meteorological Society.

[33] J.-F. Louis, R. N. Hoffman, T. Nehrkorn, and D. Norquist. Observing systems experiments using the AFGL four-dimensional data assimilation system. *Monthly Weather Review*, 117:2186–2203, 1989.

[34] R. D. McPherson, K. H. Bergman, R. E. Kistler, G. E. Rasch, and D. S. Gordon. The NMC operational global data assimilation system. *Monthly Weather Review*, 107:1445–1461, 1979.

[35] D. C. Norquist. Alternative forms of moisture information in 4-D data assimilation. Technical Report 86-0194, Air Force Geophysics Laboratory, Hanscom AFB, MA, 1986. [NTIS ADA179792].

[36] D. C. Norquist. Alternate forms of humidity information in global data assimilation. *Monthly Weather Review*, 116:452–471, 1988.

[37] P. S. Ray. Broadband complex refractive indices of ice and water. *Applied Optics*, 11:1836–1844, 1972.

[38] F. Richards and P. Arkin. On the relationship between satellite-observed cloud cover and precipitation. *Monthly Weather Review*, 109:1081–1093, 1981.

[39] J. L. Rigone and A. P. Stogryn. Data processing for the DMSP microwave radiometer system. In *Proc. Eleventh International Symp. Remote Sensing of the Environment*, pages 1599–1608, Ann Arbor, 1977. Univ. of Michigan.

[40] G. Salvetti. Spaceborne doppler wind lidars. *ESA Journal*, 11:19, 1987.

[41] J. G. Sela. Spectral modeling at the National Meteorological Center. *Monthly Weather Review*, 108:1279–1292, 1980.

[42] W. L. Smith, H. M. Woolf, and A. J. Schreiner. Simultaneous retrieval of surface and atmospheric parameters: A physical and analytically-direct approach. In A. Deepak, H. E. Fleming, and M. T. Chahine, editors, *Advances in Remote Sensing Retrieval Methods*, pages 221–232. A. Deepak Publishing, Hampton, VA, 1985.

[43] J. Susskind, J. Rosenfield, D. Reuter, and M. T. Chahine. Remote sensing of weather and climate parameters from HIRS2/MSU on TIROS-N. *Journal of Geophysical Research*, 89(D3):4677–4697, 1984.

[44] H. C. van de Hulst. *Light Scattering by Small Particles*. Wiley, New York, 1957.